

Chapter 8

Some Special Applications

We have learned from the preceding chapters that the chemical and physical state of a Mössbauer atom in any kind of solid material can be characterized by way of the hyperfine interactions which manifest themselves in the Mössbauer spectrum by the isomer shift and, where relevant, electric quadrupole and/or magnetic dipole splitting of the resonance lines. On the basis of all the parameters obtainable from a Mössbauer spectrum, it is, in most cases, possible to identify unambiguously one or more chemical species of a given Mössbauer atom occurring in the same material. This – usually called phase analysis by Mössbauer spectroscopy – is nondestructive and widely used in various kinds of physicochemical studies, for example, the studies of

- Phase transitions
- Spin and magnetic transitions
- Dynamic solid-state phenomena
- Solid-state reactions (e.g., thermolysis, radiolysis)
- Problems of metallurgy
- Surface phenomena
- Catalysis
- Corrosion
- After effects of nuclear transformations in solids
- Biological systems
- Minerals
- Archeological artifacts
- Industrial applications

Because of the limited scope of this monograph, it is impossible to give a rigorous account of the work that has been accomplished in these fields. By the end of 2008, about 60,000 publications dealing with the use of Mössbauer spectroscopy had been documented in the literature. Excellent review articles on “Mössbauer Spectroscopy Applied to Inorganic Chemistry” (3 volumes) are given in [30, 34–35] in Chap. 1 and on “Mössbauer Spectroscopy Applied to Magnetism and Materials Science” (2 volumes) in [38, 40] in Chap. 1.

The reader is also referred to the CD-ROM enclosed at the end of this book, where we have collected a large variety of examples of applications of Mössbauer spectroscopy in many disciplines. The first part of the CD-ROM presents a lecture series on Mössbauer spectroscopy (Principles and typical applications), which has been arranged particularly for teaching purposes. The second part comprises a large number of special applications contributed by various research groups specialized on Mössbauer spectroscopy.

The authors of this book consider it appropriate to include in this section two contributions from their own laboratories, one on Mössbauer spectroscopy of spin crossover (SCO) phenomena in iron(II) compounds and the other on applications to biological systems. Both chapters will demonstrate the effectiveness of Mössbauer spectroscopy in these particular fields.

8.1 Spin Crossover Phenomena in Fe(II) Complexes

8.1.1 Introduction

The behavior of SCO compounds is among the most striking and fascinating shown by relatively simple molecular species. As a consequence of the splitting of the energy of the d -orbitals into the t_{2g} and e_g sets in a ligand field, octahedral complexes of certain transition metal ions, nearly exclusively those of the first transition series with configurations d^4 – d^7 may exist in either the high-spin (HS) or low-spin (LS) state, depending on the nature of the ligand field about the metal ion. In weak fields, the ground state is HS where the spin multiplicity is a maximum, the d -electrons being distributed over the t_{2g} and e_g sets, whereas strong fields stabilize the LS state with minimum multiplicity, the t_{2g} set being completely occupied before electrons are added to the e_g set. For the d^6 configuration of iron(II), for example, the two states are illustrated by $[\text{Fe}(\text{H}_2\text{O})_6]^{2+}$, which, with the configuration $t_{2g}^4 e_g^2$, has four unpaired electrons and is thus strongly paramagnetic (${}^5T_{2g}$ state in octahedral symmetry), and by $[\text{Fe}(\text{CN})_6]^{4-}$ ($t_{2g}^6 e_g^0$), which has no unpaired electrons (${}^1A_{1g}$ state) (Fig. 8.1). For intermediate fields, the energy difference (ΔE_{HL}^0) between the

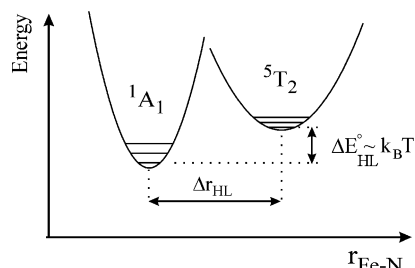


Fig. 8.1 Representation of the potential wells for the 1A_1 and 5T_2 states of an iron(II) SCO system, the nuclear coordinate being the metal–donor atom distance

lowest vibronic levels of the potential wells of the two states may be sufficiently small such that relatively minor external perturbation causes a change in the spin state. This phenomenon is known as spin transition (ST) or SCO and its origin is illustrated in Fig. 8.1. ST will be induced thermally when $\Delta E_{\text{HL}}^0 \sim k_{\text{B}}T$, and when this criterion is met, pressure- and light-induced STs may also be observed (*vide infra*).

Although STs have been observed for the first ($3d$) transition series and also partially for the second transition series, by far the greatest number has been reported for iron(II). The earlier developments in iron(II) ST systems were reviewed by König [1], Goodwin [2] and Gütlich [3]. Since then, numerous reviews have appeared on specific aspects of the phenomenon [4, 5 and references therein].

From the measurement of the temperature-dependent properties of a ST system, it is possible to evaluate the relative concentrations of HS and LS states as a function of temperature and, thus, to plot the HS molar fraction versus T . Such curves are diagnostic of the nature of the ST. The steepness of the change, for example, is indicative of the extent of cooperativity involved in the propagation of the spin change throughout the solid lattice, that is, how electronic and structural changes in a molecule proceed to neighboring molecules. When this cooperativity is low, the transition will be a gradual process, but as cooperativity increases, the transition becomes more abrupt and may occur within a very narrow range of temperature. In this case, the transition can be associated with a phase change and/or a thermal hysteresis. The transition temperature $T_{1/2}$ is defined as that temperature at which the fractions of HS and LS isomers, which take part in the transition, are equal. For transitions displaying hysteresis, two transition temperatures $T_{1/2,\downarrow}$ and $T_{1/2,\uparrow}$ define the width of the hysteresis loop. The appearance of a thermally induced ST is manifested in strong temperature-dependence of properties, which are related to the electronic structure of the system, that is, color, magnetism, and molecular structure. Since the antibonding e_g orbitals of iron(II) are unoccupied in the LS state, while they are partially occupied in the HS state, the metal–donor atom distance is remarkably sensitive to changes of the spin-state. The structural change amounts to an increase of the Fe–N bond distances by about 0.2 Å as a consequence of the singlet (1A_1) \leftrightarrow quintet (5T_2) transition. For systems in the solid state, this change in the molecular dimension may bring about fundamental changes in the crystal lattice.

It is possible to monitor an ST by a variety of techniques. The measurement of magnetic susceptibility is frequently used to characterize ST since there is a marked difference in the magnetic moments of HS (ca. 5 B.M.) and LS (ca. 0 B.M.) iron(II) and, thus, a strong temperature-dependence of the magnetic moment is expected. Magnetism alone may not be sufficient to establish the existence of ST, since magnetic properties refer to the bulk material rather than to a local atomic site. Techniques such as optical spectroscopy in the visible region, vibrational spectroscopy, and magnetic resonance methods, are frequently applied to identify and characterize ST. A survey of physical techniques and methods suitable for the investigation of SCO systems have been discussed in [6].

^{57}Fe Mössbauer spectroscopy is particularly suitable to study ST since (1) the spectral parameters associated with the HS and LS states of iron(II) clearly differ and (2) the time-scale of the technique ($\sim 10^{-7}$ s) allows the detection of the separate spin states in the course of the transition. Typically, Mössbauer spectra of HS iron(II) show relatively high quadrupole splitting ($\Delta E_Q \approx 2 - 3 \text{ mm s}^{-1}$) and isomer shift ($\delta \approx 1 \text{ mm s}^{-1}$), while for LS iron(II), these parameters are generally smaller ($\Delta E_Q \leq 1 \text{ mm s}^{-1}$, $\delta \leq 0.5 \text{ mm s}^{-1}$). Among the early applications of Mössbauer spectroscopy to study ST phenomena in iron(II) complexes is the work of Dézsi et al. [7] on $[\text{Fe}^{\text{II}}(\text{phen})_2(\text{NCS})_2]$ (phen = 1,10-phenanthroline) as a function of temperature (Fig. 8.2). The transition from the HS (5T_2) state (quadrupole doublet of outer two lines with $\Delta E_Q \approx 3 \text{ mm s}^{-1}$) to the LS (1A_1) state (quadrupole

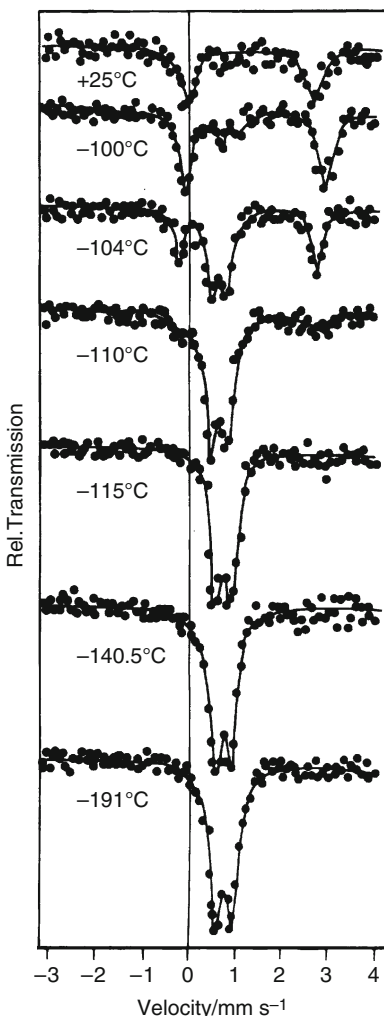


Fig. 8.2 ^{57}Fe Mössbauer spectra of $[\text{Fe}^{\text{II}}(\text{phen})_2(\text{NCS})_2]$ as a function of temperature.
At room temperature, the spectrum shows only a HS quadrupole doublet characteristic of the HS (5T_2) state. On lowering the temperature, a new quadrupole doublet (inner two lines with $\Delta E_Q \sim 0.5 \text{ mm s}^{-1}$) develops. The thermally induced ST occurs abruptly near 178 K (from [7])

doublet of inner two lines with $\Delta E_Q \approx 0.5 \text{ mm s}^{-1}$) with decreasing temperature occurs at $T_{1/2} \sim 172 \text{ K}$. Jesson et al. [8, 9] studied the $^5T_2 - ^1A_1$ transition in an iron (II) complex with hydrotris(1-pyrazolyl)borate as ligands, and Long et al. [10] remeasured the temperature-dependent Mössbauer spectra of this SCO complex several decades later (Fig. 8.3).

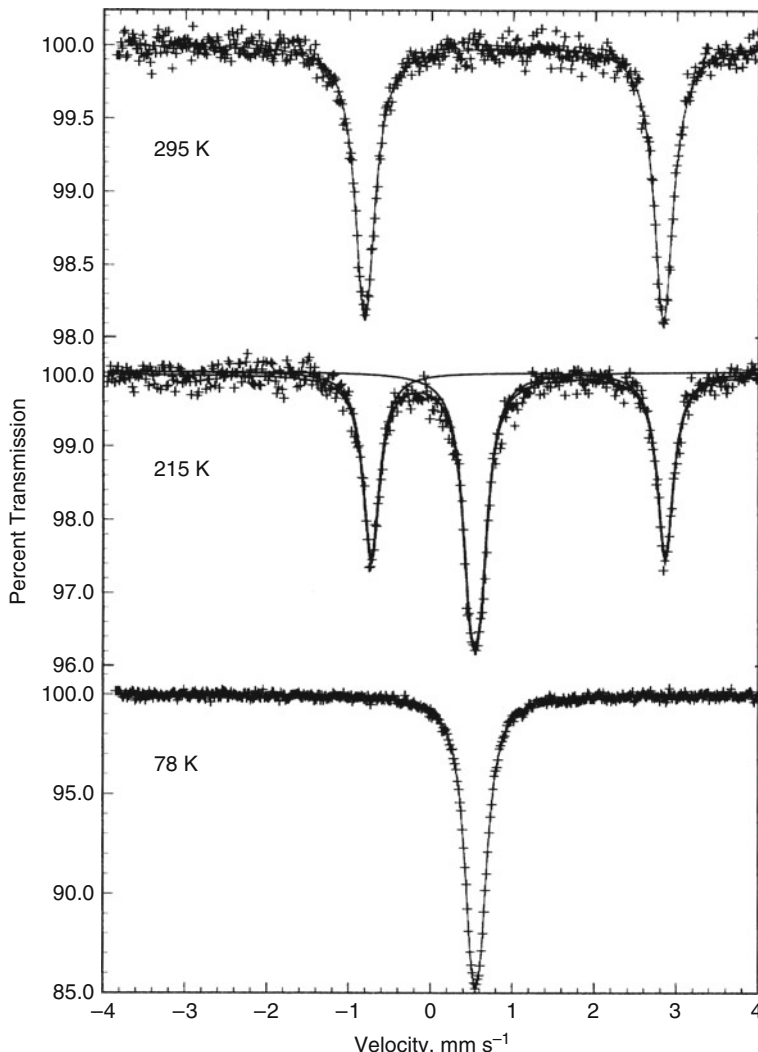


Fig. 8.3 ^{57}Fe Mössbauer spectra of $[\text{Fe}(\text{HB}(3,5-(\text{CH}_3)_2\text{pz})_3)_2]$ (pz = pyrazolyl) obtained at the indicated temperatures. The spectra were fitted with two symmetric quadrupole doublets; the outer two lines refer to the HS state and the inner (unresolved quadrupole doublet) to the LS state (from [10])

8.1.2 Spin Crossover in $[\text{Fe}(\text{2-pic})_3]\text{Cl}_2\cdot\text{Sol}$

Gütlich et al. [4, 6] have studied SCO in solid $[\text{Fe}(\text{2-pic})_3]\text{Cl}_2\cdot\text{EtOH}$ (2-pic = 2-picolyamine), particularly the influence of dilution with Zn and Co, the nature of noncoordinated anions and crystal solvent, the H/D and $^{14}\text{N}/^{15}\text{N}$ isotope effect, and the influence of pressure on ST properties. This SCO system has proven particularly suitable for mechanistic studies because of the excellent resolution of the resonance signals of the HS and LS states. As an example, Fig. 8.4 shows a series of temperature-dependent ^{57}Fe Mössbauer spectra of $[\text{Fe}(\text{2-pic})_3]\text{Cl}_2\cdot\text{EtOH}$, and the spectra in Fig. 8.5 demonstrate the effect of metal dilution in the isomorphous mixed crystal series $[\text{Fe}_x\text{Zn}_{1-x}(\text{2-pic})_3]\text{Cl}_2\cdot\text{EtOH}$ [11, 12]. On decreasing the iron concentration, the intensity of the HS quadrupole doublet increases at a given temperature and the ST curves become less steep and, additionally, they are shifted toward lower temperatures, as seen in Fig. 8.6. The inset in Fig. 8.6 shows the strong concentration dependence of the ST temperature. Clearly, this effect originates from cooperative interactions, that is, the distances between the iron(II) sites become larger and the cooperative interactions weaker with decreasing iron concentration. These cooperative interactions have been interpreted in a thermodynamic approach in the context of elasticity theory [4, 13].

The SCO properties of the system $[\text{Fe}(\text{2-pic})_3]\text{Cl}_2\cdot\text{Sol}$ ($\text{Sol} = \text{EtOH}, \text{MeOH}, \text{H}_2\text{O}$, and $2\text{H}_2\text{O}$) have been found to be strongly dependent on the nature of the solvent [14]. Temperature-dependent ^{57}Fe Mössbauer spectra of deuterated systems have proven that hydrogen bonding plays a significant role in communicating the ST from one iron site to neighboring sites via cooperative interaction [15]. ST curves for $[\text{Fe}(\text{2-pic})_3]\text{Cl}_2\cdot\text{EtOH}$, deuterated in different positions of the hydrogen bonding network, are shown in Fig. 8.7; the changes are particularly dramatic when the deuteration positions are direct constituents of the communication chain as in the case of $\text{C}_2\text{H}_5\text{OH}/\text{ND}_2$, but they are less dramatic when deuteration occurs only as an attachment to the chain, as in the case of $\text{C}_2\text{D}_5\text{OH}$ as crystal solvent. The high-resolution Mössbauer data obtained for $[\text{Fe}(\text{2-pic})_3]\text{Cl}_2\cdot\text{C}_2\text{H}_5\text{OH}$ unraveled for the first time that ST in this system actually takes place in two steps, as is clearly seen in Fig. 8.7 [16].

The ST curve is sensitive to the external pressure because of the difference in volume of the HS and LS isomers involved in the transition. The primary effect of an increase in pressure is favoring the LS state in which the metal–donor atom distances are shorter (by ca. 10%) than those of the HS state. This generally results in a displacement of the transition temperature to higher values, and this also implies an increase in the zero-point energy separation ΔE_{HL}^0 in Fig. 8.1. The study of the effect of pressure on ST systems has been pursued for many years, primarily to elucidate the subtle effects associated with the transitions and to gain insight into their mechanistic aspects. The pioneering work of Drickamer [17] on the effect of pressure on the spin state of $[\text{Fe}(\text{phen})_2(\text{NCS})_2]$ and related iron(II) ST systems provided unequivocal evidence for the $\text{HS} \rightarrow \text{LS}$ conversion with increasing pressure. The effect of pressure on the ST behavior of $[\text{Fe}(\text{2-pic})_3]\text{Cl}_2\cdot\text{C}_2\text{H}_5\text{OH}$

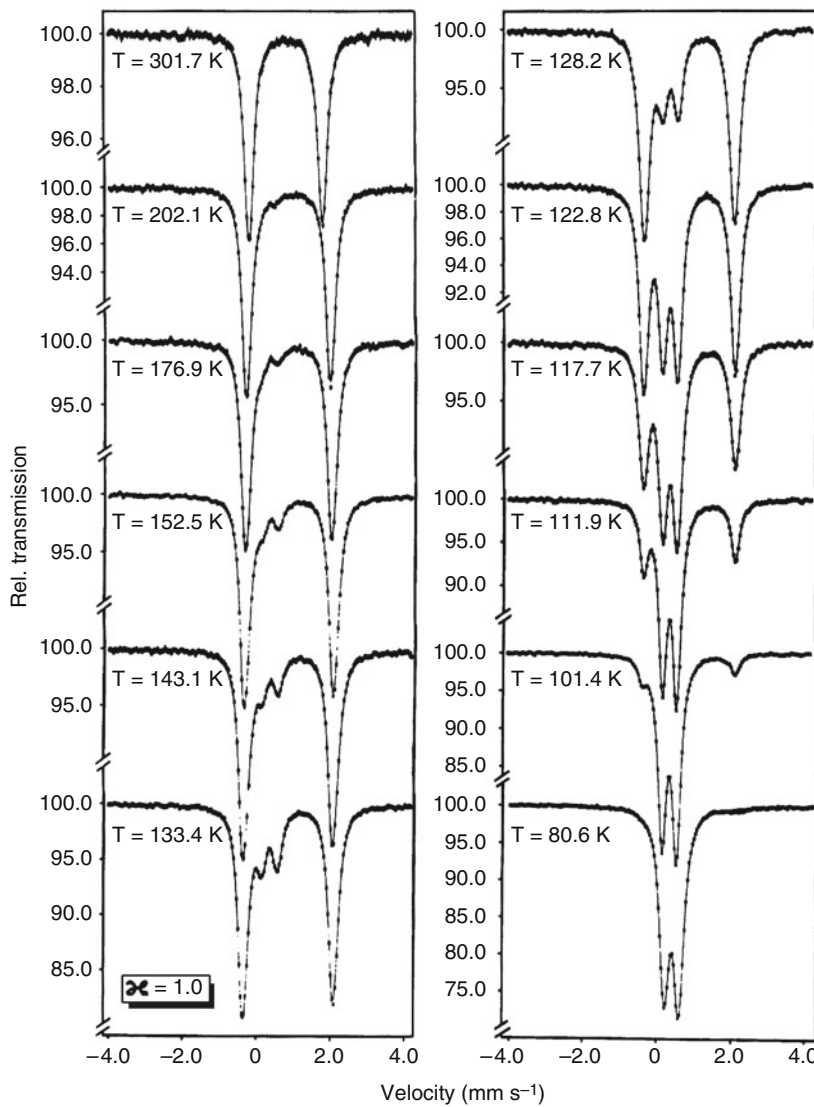


Fig. 8.4 ^{57}Fe Mössbauer spectra of $[\text{Fe}(2\text{-pic})_3]\text{Cl}_2 \cdot \text{C}_2\text{H}_5\text{OH}$ as a function of temperature (source: $^{57}\text{Co}/\text{Cu}$ at room temperature). The outer two lines represent the quadrupole doublet of the $^5\text{T}_2$ (HS) state, the inner two lines that of the $^1\text{A}_1$ (LS) state. The solid lines are obtained by a least-squares computer fit of Lorentzian lines to the experimental spectra (from [11])

was also investigated by placing the sample in a custom-made hydrostatic gas cell for pressures up to ca. 12 kbar [18] (Fig. 8.8). As expected, the intensity of the LS quadrupole doublet increased and the ST curve was shifted to higher temperatures with increase of applied pressure and, interestingly, the step in the ST curve disappeared, as is seen in Fig. 8.9 [19].

Fig. 8.5 Concentration dependence of ^{57}Fe Mössbauer spectra of $[\text{Fe}_x\text{Zn}_{1-x}(2\text{-pic})_3]\text{Cl}_2\cdot\text{C}_2\text{H}_5\text{OH}$ at 101 K. The spectra clearly reveal that the 5T_2 state is favored upon substitution of iron for zinc (from [11])

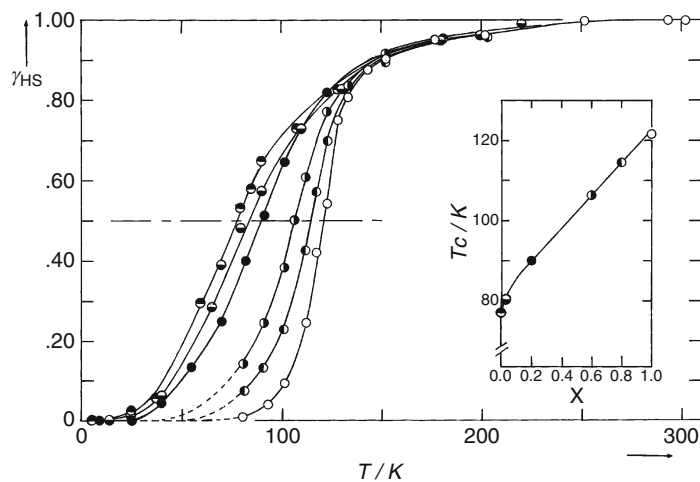
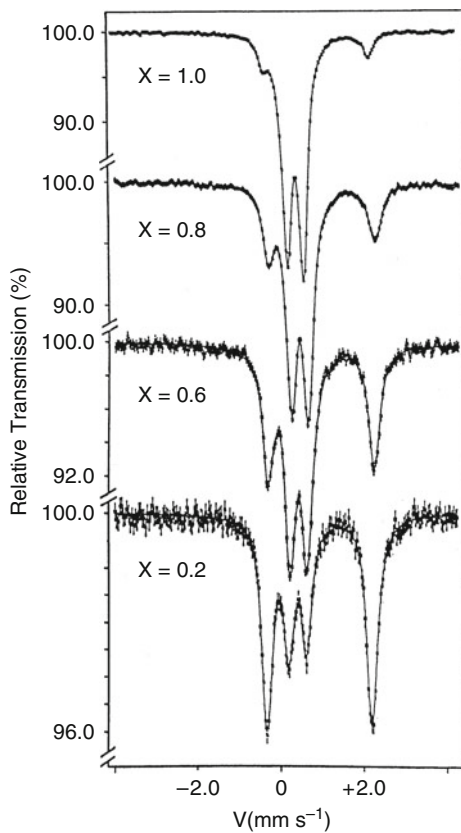
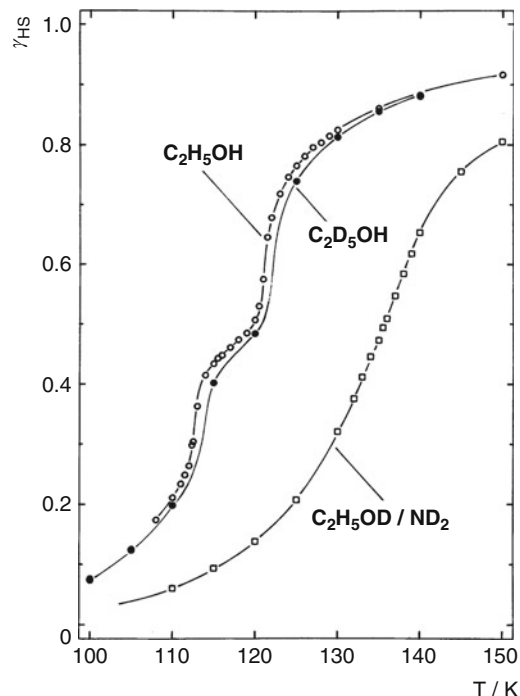


Fig. 8.6 Concentration dependence of the ST temperature for $[\text{Fe}_x\text{Zn}_{1-x}(2\text{-pic})_3]\text{Cl}_2\cdot\text{C}_2\text{H}_5\text{OH}$ at 101 K (from [11, 12])

Fig. 8.7 ST curves (molar fraction γ_{HS} as a function of temperature) for $[\text{Fe}(\text{2-pic})_3]\text{Cl}_2\text{-C}_2\text{H}_5\text{OH}$ deuterated in different positions of the solvent (from [15])



8.1.3 Effect of Light Irradiation (LIESST Effect)

In the mid-1980s, it was accidentally observed that the LS state of the iron(II) SCO compound $[\text{Fe}(\text{ptz})_6](\text{BF}_4)_2$ (ptz = 1-H-propyltetrazole) was converted by green light into the metastable HS state which had a virtually infinite lifetime at sufficiently low temperatures [20, 21]. This phenomenon became known as the LIESST effect (Light-Induced-Excited-Spin-State-Trapping). Later, it was found that the reverse process is also possible using red light [22]. The mechanism for these photoswitching processes, which turned out to be a common feature of most Fe (II) SCO systems, is sketched in Fig. 8.10 [21, 22]. Green light (514 nm from an Ar laser) is used for the spin-allowed excitation $^1\text{A}_1 \rightarrow ^1\text{T}_1$ with $^1\text{T}_1$ lifetimes typically of nanoseconds. A fast relaxation cascade over two successive intersystem crossing steps, $^1\text{T}_1 \rightarrow ^3\text{T}_1 \rightarrow ^5\text{T}_2$, populates the metastable $^5\text{T}_2$ state. Radiative relaxation $^5\text{T}_2 \rightarrow ^1\text{A}_1$ is forbidden, and decay by thermal tunneling to the ground state $^1\text{A}_1$ is slow at low temperatures. Reverse LIESST is achieved by the application of red light (ca. 820 nm), whereby the transition from the $^5\text{T}_2$ state to the ^5E state is induced with two subsequent intersystem crossing processes, $^5\text{E} \rightarrow ^3\text{T}_1 \rightarrow ^1\text{A}_1$, leading back to the LS ground state. As demonstrated later by Hauser [22], photo-switching from LS to HS is also possible via $^1\text{A}_1 \rightarrow ^3\text{T}_1 \rightarrow ^5\text{T}_2$ transitions using red light of 980 nm. LIESST has also been observed for the conversion of a HS ground state to the metastable LS state by red light [23].

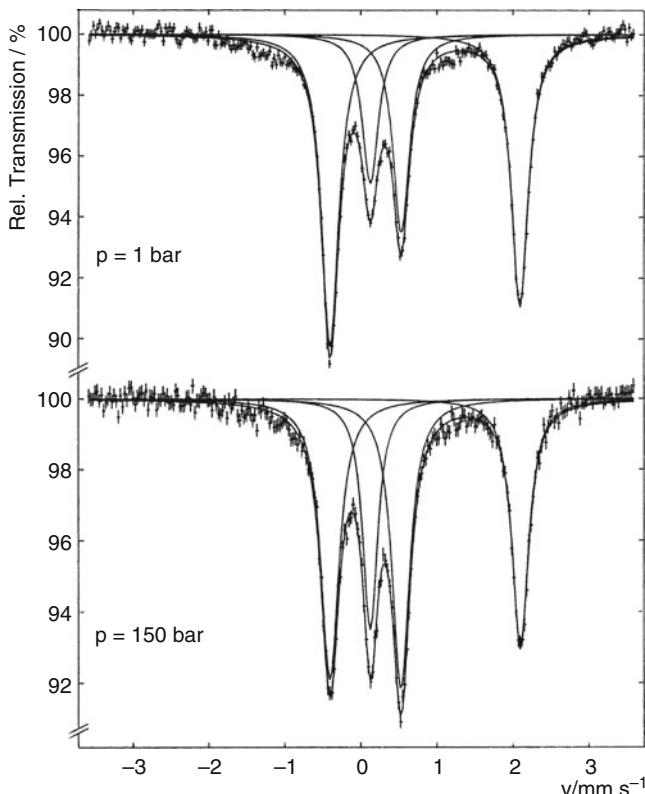


Fig. 8.8 Pressure dependence of the ^{57}Fe Mössbauer spectra of $[\text{Fe}(2\text{-pic})_3]\text{Cl}_2 \cdot \text{C}_2\text{H}_5\text{OH}$ at 121 K. The area fraction of the LS doublet (inner two lines) increases by application of pressure (from [18])

As the lifetimes of the light-induced excited spin states are relatively long in the low temperature region, Mössbauer spectroscopy can easily be employed to identify the spin states. As an example, Mössbauer spectra measured on $[\text{Fe}(\text{mtz})_6](\text{BF}_4)_2$ (mtz = 1-H-methyltetrazole) under various experimental conditions are shown in Fig. 8.11 [23]. $[\text{Fe}(\text{mtz})_6](\text{BF}_4)_2$ is an interesting SCO complex, which, according to single-crystal structure analysis, possesses two slightly inequivalent lattice sites for the iron(II) ions, that is, sites A and B. Both are in the HS state at room temperature. On lowering the temperature, only A sites undergo thermally induced ST, whereas B sites remain in the HS state at all temperatures. This is obvious from the spectrum (recorded at 50 K) in the center of Fig. 8.11. The outer lines refer to the quadrupole doublet of HS isomers at B sites; the intensity asymmetry is due to texture, a well-known effect for plate-like crystals. The poorly resolved quadrupole doublet in the middle refers to LS isomers at A sites which have undergone thermal ST from HS(A) to LS(A). Irradiating the sample with green light (514 nm) from an Ar laser at 20 K induces LS to HS conversion at A

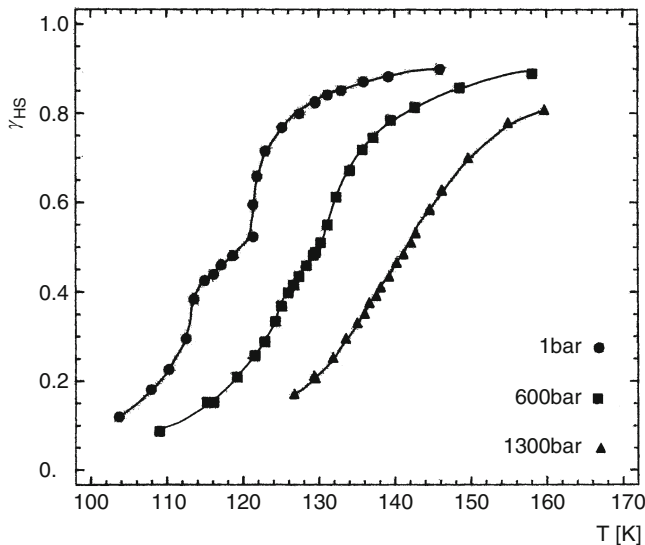


Fig. 8.9 ST curves $\gamma_{HS}(T)$ as obtained from Mössbauer measurements on $[\text{Fe}(2\text{-pic})_3]\text{Cl}_2 \cdot \text{C}_2\text{H}_5\text{OH}$ at ambient and applied hydrostatic pressures of 600 and 1,300 bar (from [19])

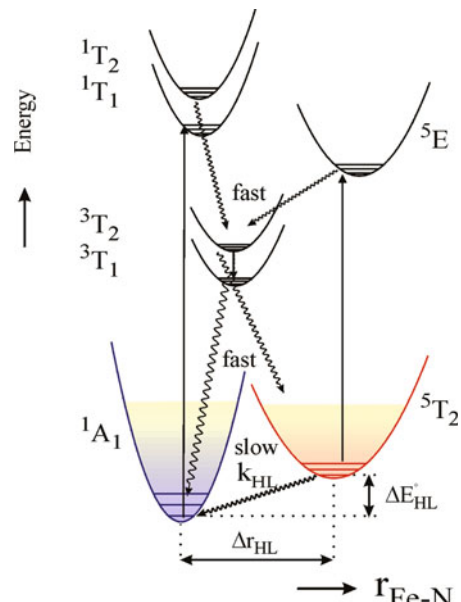


Fig. 8.10 Schematic illustration of LIESST and reverse LIESST of a d^6 complex. Spin allowed $d-d$ transitions are denoted by arrows and the radiationless relaxation processes by wavy lines (from [21])

sites (see the Mössbauer spectrum at the top of Fig. 8.11); the LS(A) quadrupole doublet has disappeared in favor of a new HS(A) doublet, also showing line intensity asymmetry due to texture. The metastable HS(A) site relaxes on heating

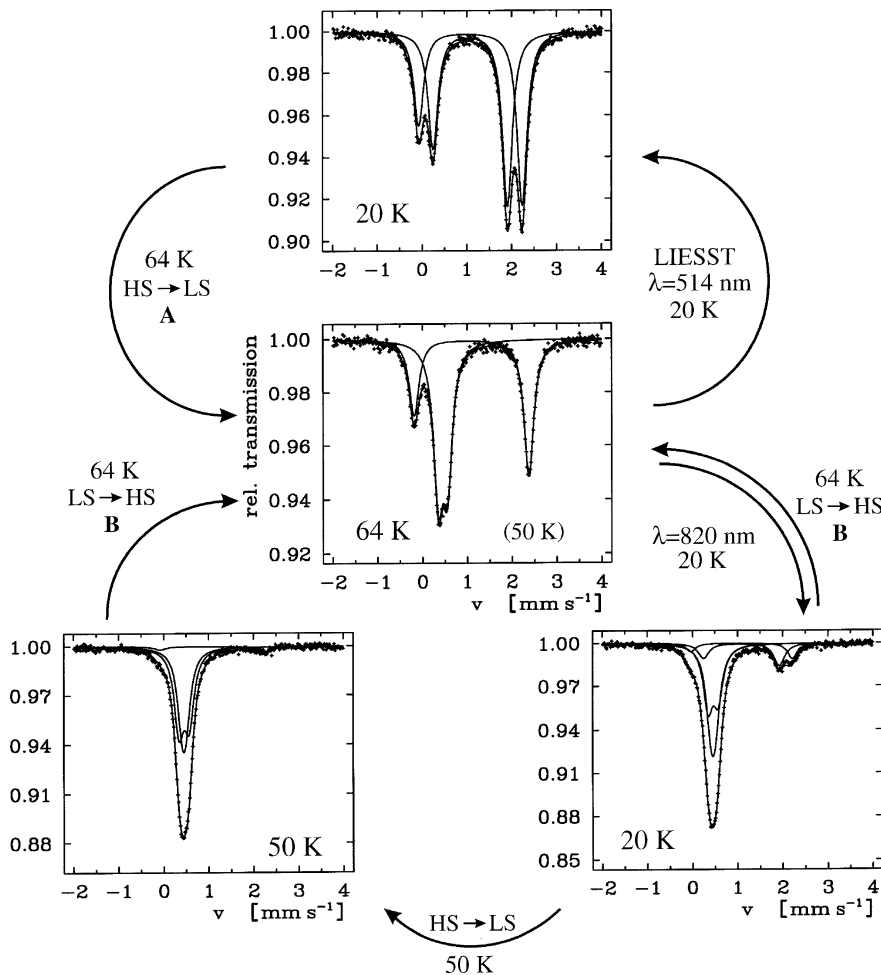


Fig. 8.11 ^{57}Fe Mössbauer spectra of $[\text{Fe}(\text{mtz})_6](\text{BF}_4)_2$ recorded under various experimental conditions as described in the text. This Mössbauer study demonstrates the LIESST (LS \leftrightarrow HS) phenomenon at A sites, where thermal ST occurs, and LIESST (HS \leftrightarrow LS) at B sites, where no thermal ST takes place (from [23])

the sample; the spectrum measured at 64 K corresponds to the original spectrum displayed in the center of Fig. 8.11 with the resonance signals for HS(B) and LS(A). If the sample is irradiated with red light (820 nm) at 20 K, the spectrum on the lower right is obtained, where essentially, the HS(B) doublet disappeared in favor of a LS signal which overlaps with the LS(A) signal. There is also a small fraction of HS (A) doublet overlapping with the HS(B) doublet; this is formed via the above-mentioned $^1\text{A}_1 \rightarrow ^3\text{T}_1 \rightarrow ^5\text{T}_2$ LIESST pathway that is possible with red light, though with lower efficiency than with green light. The light-induced conversion of stable HS(B) to metastable LS(B) was the first LIESST (HS \leftrightarrow LS) effect

reported for an iron(II) SCO complex. After thermal relaxation at 64 K, the metastable LS(B) relaxes back to the stable HS(B) state yielding the original spectrum (center of Fig. 8.11). If, however, thermal relaxation is conducted at only 50 K, the Mössbauer spectrum shown at the lower left is obtained, where essentially, the small fraction of metastable HS(A) has relaxed. At this point, the sample contained ca. 50% each of metastable LS(B) and stable LS(A) ions. Further heating to 64 K caused thermal relaxation of the metastable LS(B) isomers and yielded again the Mössbauer spectrum displayed in the center of Fig. 8.11. These experiments have demonstrated the possible existence of both HS and LS states in both A and B lattice sites at one and the same temperature, a case of bistability [23].

8.1.4 Spin Crossover in Dinuclear Iron(II) Complexes

The interplay between magnetic coupling and ST in 2,2'-bipyrimidine (bpym)-bridged iron(II) dinuclear compounds has been studied by magnetic susceptibility and ^{57}Fe Mössbauer spectroscopy [24]. The molecular structures of $\{[\text{Fe}(\text{bpym})(\text{NCS})_2]_2(\text{bpym})\}$ and $\{[\text{Fe}(\text{bt})(\text{NCS})_2]_2(\text{bpym})\}$ ($\text{bt} = 2,2'\text{-bithiazoline}$) are shown in Fig. 8.12. The magnetic behavior in the form of $\chi_M T$ versus T plots, χ_M being the magnetic susceptibility, of four members of this series is drawn in Fig. 8.13. The complex (bpym, S) does not undergo thermal ST; instead, it exhibits intramolecular antiferromagnetic coupling between the two iron(II) ions through the bpym bridge ($J = -4.1 \text{ cm}^{-1}$, $g = 2.18$) [25]. When thiocyanate is replaced by selenocyanate, the resulting (bpym, Se) derivative shows an abrupt ST in the 125–115 K temperature region with a small hysteresis loop of 2.5 K width. Only 50% of the iron atoms undergo ST. The decrease of the $\chi_M T$ values at lower temperatures is due to the zero-field splitting (ZFS) of the $S = 2$ state and does not result from a further ST (Fig. 8.14e). The magnetic properties of the compounds abbreviated as (bt, S) and (bt, Se) are similar and show a complete ST with the remarkable feature that it takes

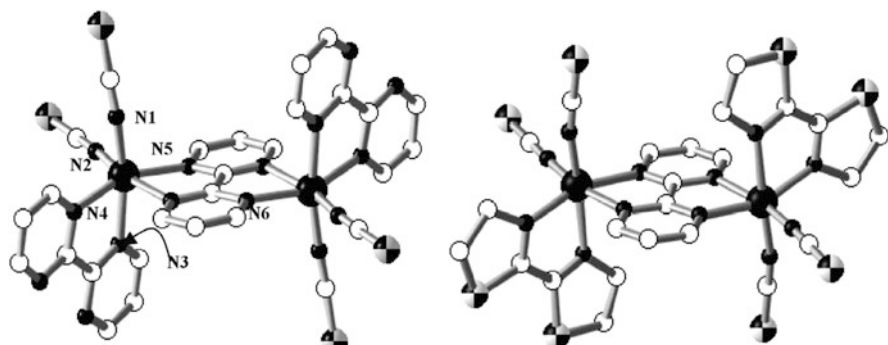


Fig. 8.12 Molecular structures of $\{[\text{Fe}(\text{bpym})(\text{NCS})_2]_2(\text{bpym})\}$ (left) and of $\{[\text{Fe}(\text{bt})(\text{NCS})_2]_2(\text{bpym})\}$ (right) (from [24, 25])

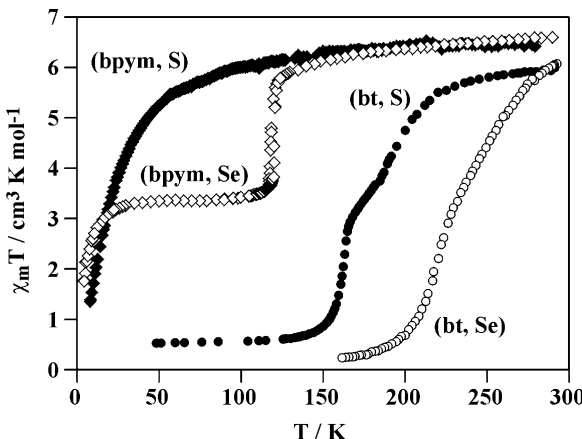


Fig. 8.13 Temperature dependence of $\chi_M T$ for $\{[\text{Fe}(\text{bpym})(\text{NCS})_2]_2(\text{bpym})\}$ ($L = \text{bpym}$ and $X = \text{S}$ (bpym, S) or Se (bpym, Se)) and $L = \text{bt}$ and $X = \text{S}$ (bt, S) or Se (bt, Se)) (from [25])

place in two steps, though somewhat less pronounced than in the (bpym, Se) derivative. ST is centered at 197 and 163 K for (bt, S) and at 265 and 223 K for (bt, Se). In both cases, the region between the two steps corresponds approximately to 50% spin conversion. These steps, also detected by Mössbauer and calorimetric measurements, were interpreted in terms of a microscopic two-step transition between the three possible spin pairs of each individual dinuclear molecule [26]: $[\text{HS}-\text{HS}] \leftrightarrow [\text{HS}-\text{LS}] \leftrightarrow [\text{LS}-\text{LS}]$. Of particular interest has been the nature of the plateau (region between the two steps) in the ST curve of dinuclear iron(II) complexes. In the case of the (bpym, Se) derivative, for instance, it may either be a 1:1 mixture of [HS–HS] and [LS–LS] pairs, or it may consist only of the mixed spin-state pairs [HS–LS]. Both situations are not distinguishable in the $\chi_M T$ versus T plot. In this situation, conventional Mössbauer spectroscopy is not sensitive, since the spectra corresponding to the HS state of iron(II) in the [HS–LS] and [HS–HS] spin pairs are indistinguishable. Differentiation of three spin pairs [HS–HS], [HS–LS], [LS–LS], however, is possible by Mössbauer measurements in applied field [27]. This is demonstrated for the (bpym, S), (bpym, Se) and (bt, S) derivatives by the spectra shown in Fig. 8.14.

The effective hyperfine field H_{eff} at the iron nuclei of a paramagnetic nonconducting sample in an external field H_{ext} may be estimated as $H_{\text{eff}} \approx H_{\text{ext}} - (220 - 600(g - 2))\langle S \rangle$ where $\langle S \rangle$ is the expectation value of the iron spin and g is the Landé splitting factor [28, 29]. The difference between the expectation values of S for the LS and the HS states in [HS–LS] and [HS–HS] pairs permits unambiguous distinction between these dinuclear units. To do so, the strength of the external field should be sufficiently high and the temperature sufficiently low in order to avoid magnetic relaxation taking place within the characteristic time window of the Mössbauer experiment. Figure 8.14 displays the Mössbauer spectra of (bpym, S), (bpym, Se), and (bt, S) recorded at 4.2 K in zero-field and at 50 kOe,

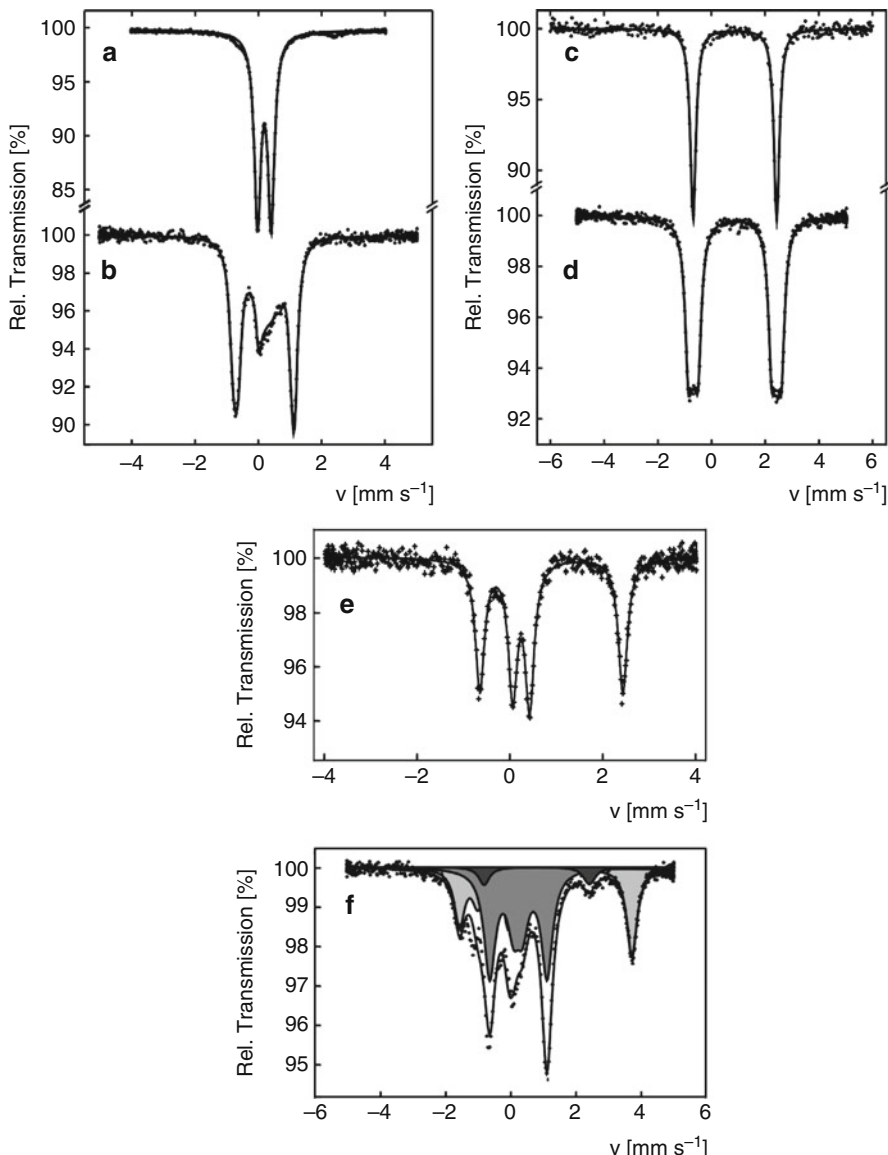


Fig. 8.14 Mössbauer spectra of (bt, S) recorded at 4.2 K in zero-field (**a**) and in a field of 50 kOe (**b**), of (bpym, S) recorded at 4.2 K in zero-field (**c**) and in a magnetic field of 50 kOe (**d**), of (bpym, Se) recorded at 4.2 K in zero-field (**e**) and in a magnetic field of 50 kOe (**f**). LS in [HS–LS] and [LS–LS] pairs (gray), HS in [HS–LS] pairs (light gray), HS in [HS–HS] pairs (dark gray) (from [27])

respectively. The zero-field spectrum of the (bt, S) complex with only [LS–LS] pairs present at low temperatures shows the expected typical iron(II)-LS quadrupole doublet with isomer shift $\delta_{\text{LS}}(\text{bt}, \text{S}) = 0.19(1) \text{ mm s}^{-1}$ and quadrupole splitting

$\Delta E_{Q(LS)}$ (bt, S) = 0.43(2) mm s⁻¹ at 4.2 K (Fig. 8.14a). In an applied field of $H_{\text{eff}} = 50$ kOe, magnetic splitting is observed with a local effective field of $H_{\text{eff}} \approx 50$ kOe as is expected for $\langle S \rangle = 0$ of the [LS–LS] pair (Fig. 8.14b). The zero-field spectrum of (bpym, S), consisting of only [HS–HS] pairs, is characterized by a typical HS doublet (Fig. 8.14c). The presence of an external magnetic field causes a slight broadening of the doublet lines (Fig. 8.14d). The value of the effective field, H_{eff} , calculated from this spectrum is 15 kOe. The difference between $H_{\text{ext}} = 50$ kOe and the observed field at the iron nucleus, H_{eff} , arises from the antiferromagnetic nature of the [HS–HS] pairs. In fact, the $\langle S \rangle$ value deduced from the corresponding partition function is around 0.5, which is consistent with the parameters $J = -4.1$ cm⁻¹ and $g = 2.2$ for (bpym, S) at 4.2 K. The zero-field spectrum of the (bpym, Se) complex recorded at 4.2 K reflects the nearly 50% ST by virtue of the nearly 1:1 intensity ratio of the HS:LS resonance signals with parameters $\delta_{\text{HS}} = 0.86(1)$ mm s⁻¹, $\Delta E_Q(\text{HS}) = 3.11(2)$ mm s⁻¹, and $\delta_{\text{LS}} = 0.22(1)$ mm s⁻¹, $\Delta E_Q(\text{LS}) = 0.36(1)$ mm s⁻¹, respectively (Fig. 8.14e). Measurements in a magnetic field of 50 kOe at 4.2 K yield a spectrum with three components (Fig. 8.14f). One of them, with a relative intensity of ca. 52.0% and with isomer shift and quadrupole splitting being equal to δ_{LS} (bt, S) and $\Delta E_{Q(\text{LS})}$ (bt, S), can be identified as the LS state ($H_{\text{eff}} \approx H_{\text{ext}}$). The second low-intensity contribution (ca. 4.0%) is a broadened doublet with parameters δ_{HS} (bpym, S) and $\Delta E_{Q(\text{HS})}$ (bpym, S) and $H_{\text{eff}} = 14$ kOe corresponding to iron(II) sites in antiferromagnetically coupled [HS–HS] pairs. The third component (relative intensity ca. 44.0%) with parameters δ_{HS} (bpym, S) and $\Delta E_{Q(\text{HS})}$ (bpym, S) can be unambiguously assigned to the HS state in [HS–LS] pairs because the measured effective field at the iron nuclei of 81 kOe originates from an $S = 2$ spin state. As a result, the complete distinction of dinuclear units becomes possible. It follows from the area fractions of the subspectra intensities that, at 4.2 K, the sample (bpym, Se) contains 88.0% [HS–LS], 4.0% [HS–HS] and 8.0% [LS–LS] pairs.

These results obtained in applied field clearly prove that the ST in the dinuclear compounds under study proceeds via [HS–HS] \leftrightarrow [HS–LS] \leftrightarrow [LS–LS]. Simultaneous ST in both iron centers of the [HS–HS] pairs, leading directly to [LS–LS] pairs, apparently can be excluded, at least in the systems discussed above. This is surprising in view of the fact that these dinuclear complexes are centrosymmetric, that is, the two metal centers have identical surroundings and therefore, experience the same ligand field strength and consequently, thermal ST is expected to set in simultaneously in both centers. In other dinuclear iron(II) complexes, however, thermally induced direct ST from [HS–HS] to [LS–LS] pairs does occur and, indeed, has been observed by Mössbauer measurements [30, 31].

An interesting Mössbauer study has been reported on the dinuclear SCO complex $[\text{Fe}_2^{\text{II}}(\text{PMAT})_2](\text{BF}_4)_4 \cdot \text{DMF}$ (PMAT: 4-amino-3,5-bis{[(2-pyridylmethyl)amino]methyl}-4H-1,2,4-triazole), where thermal ST occurs from [HS–HS] to the stable endproduct [HS–LS] [32]. The molecular structure and magnetic behavior of this complex was reported earlier by Brooker et al. [33, 34] (Fig. 8.15). At ca. 225 K, the complex undergoes a sharp half ST from the HS state, 5T_2 , to a state containing 50% HS and 50% LS, 1A_1 , isomers. The single-crystal structural analysis

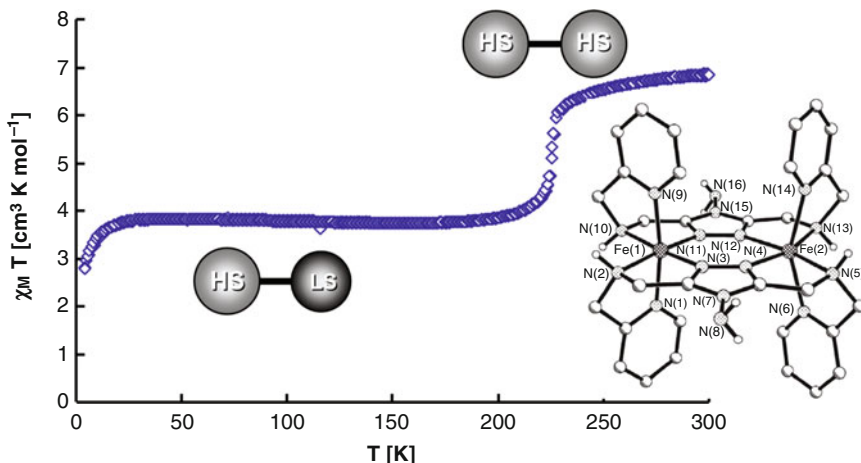


Fig. 8.15 Molecular structure and magnetic properties, $\chi_M T$ versus T , of $[\text{Fe}_2^{\text{II}}(\text{PMAT})_2](\text{BF}_4)_4 \cdot \text{DMF}$. Only half of the Fe(II) sites undergo thermal SCO from HS to LS (from [33, 34])

at 123 K has identified that the dinuclear complex contains one Fe(II) in the LS state and one in the HS state, the latter with Fe–N bond distances about 10% longer than those in the LS state. The sharp decrease of the magnetic susceptibility below 30 K is due to the ZFS effect at the 50% HS isomers. The inset of Fig. 8.15 illustrates (1) that the LS site has decreased in volume (by up to 5%) as compared to the HS site and (2) that the HS site (dark gray) in the LS–HS pair has suffered a slight structural distortion during ST from HS–HS to LS–HS. This situation is in full accord with the Mössbauer data obtained from $[\text{Fe}_2^{\text{II}}(\text{PMAT})_2](\text{BF}_4)_4 \cdot \text{DMF}$ [32]. Mössbauer spectra were recorded as a function of temperature between 298 and 4.2 K (Fig. 8.16). At 298 K, the only quadrupole doublet, $\delta = 0.96 \text{ mm s}^{-1}$ and $\Delta E_Q = 2.34 \text{ mm s}^{-1}$ is characteristic of Fe(II) in the HS state and is consistent with the presence of only [HS–HS] pairs. The slight intensity asymmetry is due to texture; therefore, all further measurements were carried out with the sample mounted at the magic angle of 54° with respect to the γ -radiation, which results in symmetric intensities of the quadrupole doublet. As the temperature is decreased to 240 K, two new doublets (black and dark gray) appear at the expense of the original HS doublet (light gray). The doublet (black) with $\delta = 0.36 \text{ mm s}^{-1}$, $\Delta E_Q = 0.26 \text{ mm s}^{-1}$ and area fraction $A = 10.3\%$, arises from the LS site in [HS–LS] pairs, which are formed as a result of thermal HS to LS transition. The doublet (dark gray) with $\delta = 0.96 \text{ mm s}^{-1}$, $\Delta E_Q = 1.66 \text{ mm s}^{-1}$ and area fraction $A = 10.3\%$, is unambiguously due to the HS site in these HS–LS pairs. The doublet arising from the original [HS–HS] pairs (light gray) now yields $\delta = 0.92 \text{ mm s}^{-1}$ and a slightly larger $\Delta E_Q = 2.65 \text{ mm s}^{-1}$ (compared to the value obtained at higher temperature) and area fraction $A \sim 80\%$. By further lowering the temperature, the doublet (light gray) arising from original [HS–HS] pairs continues to lose intensity in favor of the new doublets (dark gray and black) with equal area fractions. In the plateau region,

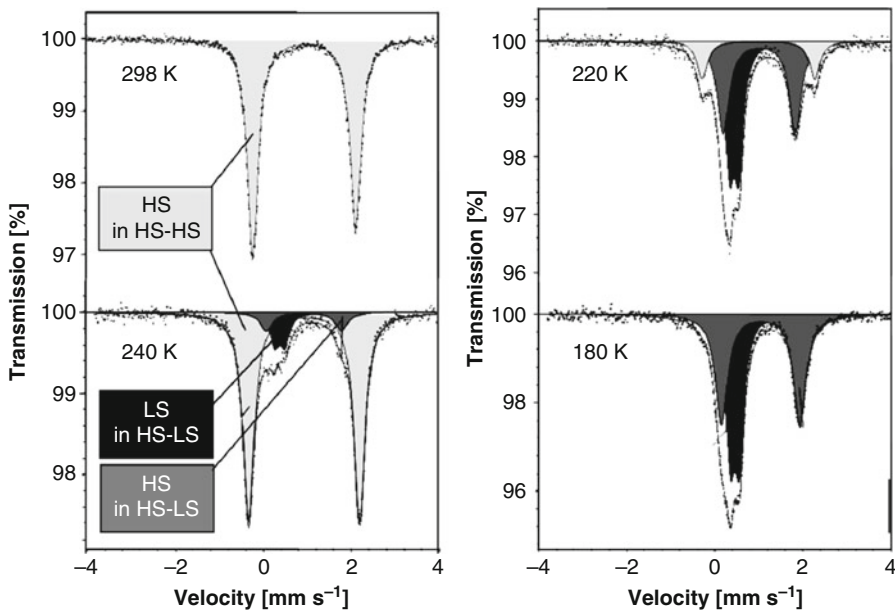


Fig. 8.16 ^{57}Fe Mössbauer spectra of $[\text{Fe}_2\text{II}(\text{PMAT})_2](\text{BF}_4)_4\text{-DMF}$ at selected temperatures. At 298 K, the only quadrupole doublet is characteristic of iron(II) in the HS state. SCO from HS to LS occurs at one Fe(II) site of the dinuclear complex at ca. 225 K. The second Fe(II) site remains in the HS state, but “feels” the spin state conversion of the neighboring atom by local distortions communicated through the rigid bridging ligand, giving rise to a new quadrupole doublet (*dark gray*), i.e., HS in [HS–LS], in the Mössbauer spectrum. The intensity ratio of the resonance signals of HS in [HS–LS] to that of LS (black) in [HS–LS] is close to 1:1 at all temperatures (from [32])

at 180 K and below, the half ST is complete and the doublet (*light gray*) from original [HS–HS] pairs has vanished.

Clearly, one of the two HS sites in the [HS–HS] pair undergoes thermal SCO generating a [HS–LS] pair. The unique feature is the concomitant appearance of the new HS quadrupole doublet, with a smaller ΔE_Q than the original HS doublet. This is clearly due to local structural distortion at the HS site induced by the newly formed LS state and communicated via the bridging ligand. This distortion at the iron center affects the electric field gradient (EFG) at the ^{57}Fe nucleus and causes a reduction of the ΔE_Q value of the new HS quadrupole doublet. The formation of [HS–LS] intermediates is favored by rigid bridging ligands in these dinuclear systems.

8.1.5 Spin Crossover in a Trinuclear Iron(II) Complex

Thermal ST occurs in the trinuclear iron(II) complex $[\text{Fe}_3(\text{iptrz})_6(\text{H}_2\text{O})_6](\text{Trifl})_6$ (with iptrz = 4-isopropyl-1,2,4-triazole and Trifl = trifluoromethanesulfonate) only at the

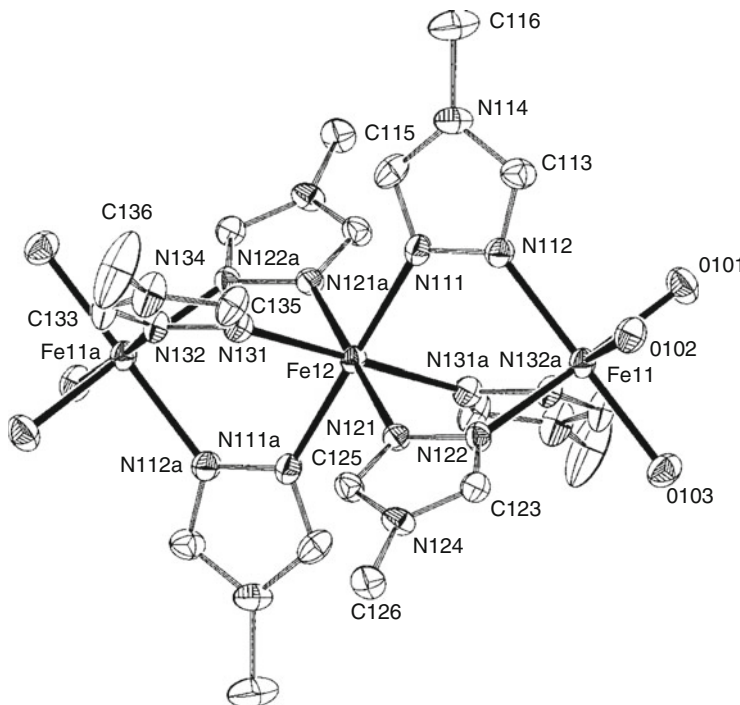


Fig. 8.17 Projection showing the molecular structure of $[\text{Fe}_3(\text{iptrz})_6(\text{H}_2\text{O})_6](\text{Trifl})_6$ (from [35])

central iron(II) site, whereas the outer two iron(II) sites remain in the HS state at all temperatures under study [35]. A simplified version of the molecular structure is shown in Fig. 8.17. The central iron(II) site is coordinated to six nitrogen atoms belonging to three 1,2,4-triazole units on either side forming the bridges to the outer two iron(II) sites, which are capped by three water molecules on either site. The central site has a FeN_6 core and the appropriate ligand field strength to meet the thermal SCO conditions. The outer two sites have FeN_3O_3 cores and thus possess a weaker ligand field strength, obviously too weak for thermal SCO to occur. Figure 8.18 shows the Mössbauer spectra of this complex recorded at the indicated temperatures. At 300 K, the two quadrupole doublets, that is, HS_{c} (red) and HS_{o} (yellow), are characteristic for ferrous iron in the HS state and represent the central site and the two outer sites, respectively. The area fractions of the two doublets deviate from the ratio 1:2. The reason is that the outer Fe(II) sites with their FeN_3O_3 cores experience a relatively weak ligand field strength and are, therefore, more weakly bonded to their donor atoms than the central Fe(II) site with its FeN_6 core and stronger ligand field strength. Consequently, the Lamb–Mössbauer factor of the outer Fe(II) sites is lower than that of the central Fe(II) site and, thus, the corresponding intensities of the Mössbauer resonance lines do not reflect the

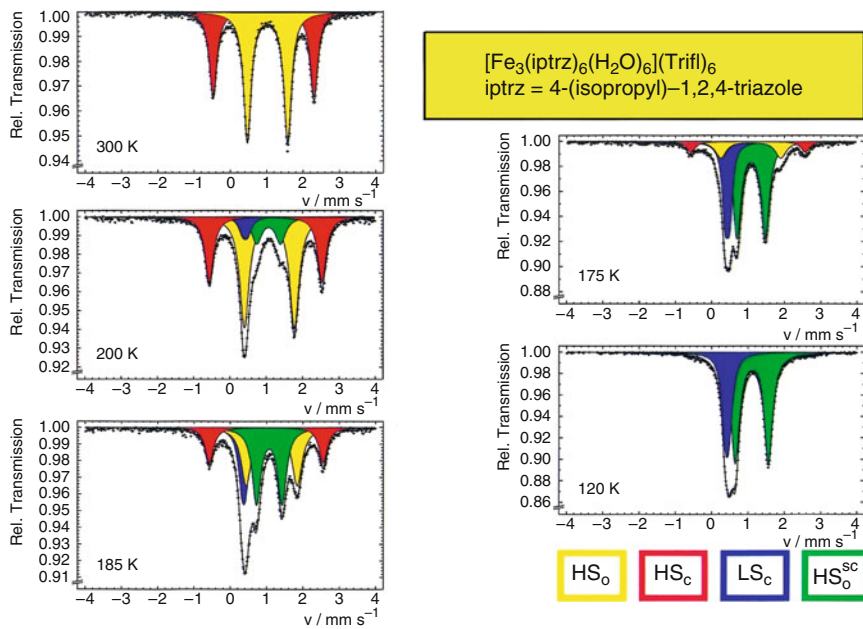


Fig. 8.18 ^{57}Fe Mössbauer spectra of the trinuclear complex $[\text{Fe}_3(\text{iptrz})_6(\text{H}_2\text{O})_6](\text{Trifl})_6$ recorded at the indicated temperatures. Only the central Fe(II) site undergoes thermally induced ST, HS_c (red) \rightarrow LS_c (blue). The outer two Fe(II) sites, which remain in HS state at all temperatures, “feel” the ST occurring at the central iron site through a molecular distortion, the latter giving rise to a new quadrupole doublet, $\text{HS}_o \rightarrow \text{HS}_o^{\text{SCO}}$ (from [35])

actual concentrations; those of the HS_c doublet are overweighted in comparison with the HS_o doublet.

Lowering temperature to 200 K, the thermally induced ST at the central Fe(II) site sets in with the appearance of two new doublets in the Mössbauer spectrum: (1) the poorly resolved doublet termed LS_c refers to central Fe(II) sites now being in the LS state, and (2) the doublet termed HS_o^{SCO} arises from the outer Fe(II) sites of those trinuclear molecules, the central Fe(II) site of which has undergone $\text{HS} \rightarrow \text{LS}$ conversion (a similar situation was discussed above for the dinuclear complex $[\text{Fe}_2^{\text{II}}(\text{PMAT})_2](\text{BF}_4)_4 \cdot \text{DMF}$ also giving rise to a new HS doublet). The area fraction ratio of $\text{LS}_c:\text{HS}_o^{\text{SCO}}$ derived from the Mössbauer spectra is nearly 1:2 at all temperatures under study; deviations are again due to different Lamb-Mössbauer factors as discussed earlier. The spectrum measured at 120 K can be decomposed into two doublets arising from LS_c and HS_o^{SCO} , respectively. Thus, thermal ST at the central Fe(II) site is complete at this temperature. The signals referring to HS_c and HS_o vanish in favor of LS_c and HS_o^{SCO} . In conclusion, the presented example demonstrates that the Mössbauer technique is an excellent tool to follow the selective spin switching in polynuclear systems.

8.1.6 Spin Crossover in Metallomesogens

Metallomesogens belong to a class of metal-containing compounds which exhibit liquid–crystal properties. The possibility of combining the properties of fluidity, ease of processability, one- or two-dimensional order, etc., with the properties associated with metal atoms, for example, color, paramagnetism, electron-rich environment, is the main objective of progress in this field. In addition, the possibility of tuning the physical (mesomorphic, optical, and magnetic) properties of metallomesogens is significantly extended, since the organic ligand of these systems can be varied. Liquid crystalline materials in which a spin crossover center is incorporated into the mesogenic organic skeleton constitute a separate class of compounds for which an interplay of structural transition and liquid crystallinity is expected. This may lead to advantages in practical applications, for example, processing SCO materials in the form of thin films, enhancement of ST signals, switching and sensing in different temperature regimes, and the achievement of photo and thermochromism in metal-containing liquid crystals. The change of color in coexistence with liquid crystallinity is certainly a phenomenon which is of interest in the field of material sciences.

Galyametdinov et al. [36] reported on temperature-dependent Mössbauer and magnetic susceptibility measurements of an iron(III) compound which exhibits liquid crystalline properties above – and thermal ST below – room temperature. This was the first example of SCO in metallomesogens. Later, different families of iron(II) and cobalt(II) systems were also investigated [37–43]. The question whether the solid–liquid crystal phase transition provokes the spin-state change in spin crossover metallomesogens has been addressed in several series of iron(II) systems employing a variety of physical measurements [43]. In all these studies, ^{57}Fe Mössbauer spectroscopy has been extremely helpful, for example, in controlling the completeness of ST in both the high and low temperature regions where $\chi_M T$ data are often not reliable due to calibration difficulties. Also, one can unambiguously decide whether a significant decrease of the $\chi_M T$ versus T plot toward lower temperatures is due to SCO or ZFS. An example is the study of the one-dimensional triazole-based compound $[\text{Fe}(\text{C}_{10}\text{-tba})_3](4\text{-MeC}_6\text{H}_4\text{SO}_3)_2 \cdot s\text{H}_2\text{O}$, with $\text{C}_{10}\text{-tba} = 3,5\text{-bis(decyloxy)-}N\text{-(4H-1,2,4-triazol-4-yl)benzamide}$, $s = 1$ or 0 [44, 45]. This system exhibits thermal SCO with a concomitant change of color between white (HS state) and purple (LS state). The magnetic properties of the pristine compound ($s = 1$) in the form of a $\chi_M T$ versus T plot are depicted in Fig. 8.19. At 300 K, the value of $\chi_M T = 0.20 \text{ cm}^3 \text{ K mol}^{-1}$ indicates that this complex is apparently in the LS state. The Mössbauer spectrum recorded at 4.2 K is in agreement with the magnetic data, that is, the HS population is 4.8% and the LS population 95.2% (Fig. 8.20a). Upon heating, $\chi_M T$ increases abruptly within a few degrees, reaching the value of $3.74 \text{ cm}^3 \text{ K mol}^{-1}$ at 342 K. This clearly shows that ST from $S = 0$ to $S = 2$ has occurred. The thermogravimetric analysis (TGA) of this system has shown that dehydration takes place in the same temperature region where SCO occurs. The magnetic susceptibility of the dehydrated compound ($s = 0$)

Fig. 8.19 Magnetic properties in the form of $\chi_M T$ versus T of the complexes $[\text{Fe}(\text{C}_{10}-\text{tba})_3] \cdot (4\text{-MeC}_6\text{H}_4\text{SO}_3)_2 \cdot s\text{H}_2\text{O}$, $s = 1$ (filled circle) and $s = 0$ (open circle). Both complexes exhibit thermal SCO (from [44, 45])

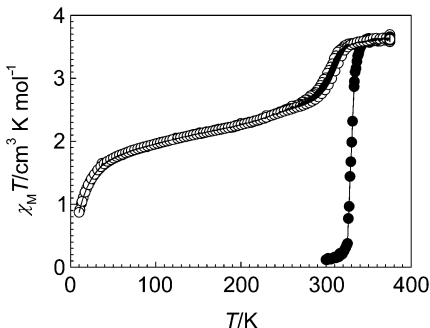
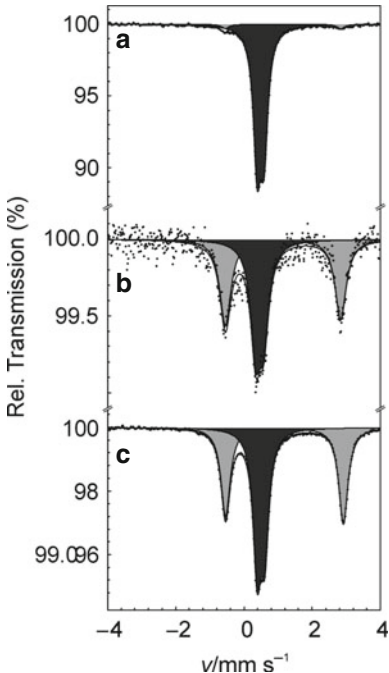


Fig. 8.20 Mössbauer spectra of $[\text{Fe}(\text{C}_{10}-\text{tba})_3] \cdot (4\text{-MeC}_6\text{H}_4\text{SO}_3)_2 \cdot s\text{H}_2\text{O}$, $s = 1$ at 4.2 K (a) and of $s = 0$ at 200 K (b) and at 4.2 K (c) (from [44, 45])



was recorded in a temperature loop, that is, from 375 K down to 10 K and then up again to 375 K. The dehydrated complex reveals incomplete and abrupt SCO, accompanied by hysteresis and color change (from purple in the LS state to white in the HS state) in the temperature region of 250–300 K. Around 50% of Fe(II) sites change spin state, as can be inferred from the value of $\chi_M T$ at 200 K. The Mössbauer spectrum recorded at 200 K show that 49.3% of the iron is in the LS state and 50.7% in the HS state. The further decrease of the $\chi_M T$ value below 100 K, particularly below 50 K, is due to the ZFS of those iron ions which remain in the HS state even at very low temperature, as derived from the Mössbauer spectrum at 4.2 K (HS population is 48.1%, LS population is 51.9%) (Fig. 8.20c).

8.1.7 Effect of Nuclear Decay: Mössbauer Emission Spectroscopy

The nuclear decay of radioactive atoms embedded in a host is known to lead to various chemical and physical “after effects” such as redox processes, bond rupture, and the formation of metastable states [46]. A very successful way of investigating such after effects in solid material exploits the Mössbauer effect and has been termed “Mössbauer Emission Spectroscopy” (MES) or “Mössbauer source experiments” [47, 48]. For instance, the electron capture (EC) decay of ^{57}Co to ^{57}Fe , denoted $^{57}\text{Co}(\text{EC})^{57}\text{Fe}$, in cobalt- or iron-containing compounds has been widely explored. In such MES experiments, the compound under study is usually labeled with ^{57}Co and then used as the Mössbauer source versus a single-line absorber material such as $\text{K}_4[\text{Fe}(\text{CN})_6]$. The recorded spectrum yields information on the chemical state of the nucleogenic ^{57}Fe at ca. 10^{-7} s, which is approximately the lifetime of the 14.4 keV metastable nuclear state of ^{57}Fe after nuclear decay.

The MES technique has been applied to ^{57}Co -labeled cobalt(II) and iron(II) coordination compounds with strong, intermediate, and weak ligand fields. Among the most interesting results are the formation of metastable HS states of $^{57}\text{Fe}(\text{II})$ in strong and intermediate ligand fields as exemplified by the following two cases: (1) $[\text{Fe}(\text{phen})_3](\text{ClO}_4)_2$ (phen = 1,10-phenanthroline), a typical LS compound at room temperature and below, and (2) $[\text{Fe}(\text{phen})_2(\text{NCS})_2]$, a typical SCO system. Mössbauer emission spectra of $[^{57}\text{Co}/\text{Co}(\text{phen})_3](\text{ClO}_4)_2$ as a function of temperature versus $\text{K}_4[\text{Fe}(\text{CN})_6]$ as absorber (which was kept at 295 K) are depicted in Fig. 8.21 and are compared with ^{57}Fe absorption spectra of $[^{57}\text{Fe}/\text{Co}(\text{phen})_3](\text{ClO}_4)_2$ as a function of temperature versus $^{57}\text{Co}/\text{Rh}$ as source (which was kept at 295 K). The main component in the emission spectra of $[^{57}\text{Co}/\text{Co}(\text{phen})_3](\text{ClO}_4)_2$ refers to $^{57}\text{Fe}(\text{phen})_3](\text{ClO}_4)_2$. At temperatures down to ca. 200 K, the spin state is LS, but below ca. 200 K, new signals, clearly indicative of $^{57}\text{Fe}(\text{II})$ in the HS state, appear with increasing intensity at the expense of the $^{57}\text{Fe}(\text{II})$ -LS signals. Thus, even in the case of a strong ligand field environment of the iron, such as $(\text{phen})_3$, where $\text{Fe}(\text{II})$ -LS is the thermodynamically stable state, the metastable state $^{57}\text{Fe}(\text{II})$ -HS can be detected in the low-temperature regime with lifetimes of the order of 10^{-7} s [48]. Interestingly, there is no significant difference if one uses the paramagnetic $[\text{Co}(\text{phen})_3]^{2+}$ or the diamagnetic $[\text{Fe}(\text{phen})_3]^{2+}$ compound as the Mössbauer source; the only important consideration is the immediate ligand cage of ^{57}Co or ^{57}Fe , respectively, after decay. If the ^{57}Co ion decays in a somewhat weaker ligand field such as $(\text{phen})_2(\text{NCS})_2$, which is known to induce thermal SCO, $\text{LS} \leftrightarrow \text{HS}$, at the iron(II) center, the nucleogenic $^{57}\text{Fe}(\text{II})$ manifests itself in the HS state at all temperatures down to 4.2 K [49]. This is shown in Fig. 8.22. Similar results have also been observed with other ^{57}Co -labeled iron(II) SCO systems [50].

The essential information from these Mössbauer source experiments is that, at a given temperature, the probability of “trapping” the HS state of the nucleogenic $^{57}\text{Fe}(\text{II})$ within the Mössbauer time window is significantly greater in SCO compounds with intermediate ligand field strength than in those with strong ligand field. The discovery of the LIESST phenomenon (generating and trapping of metastable

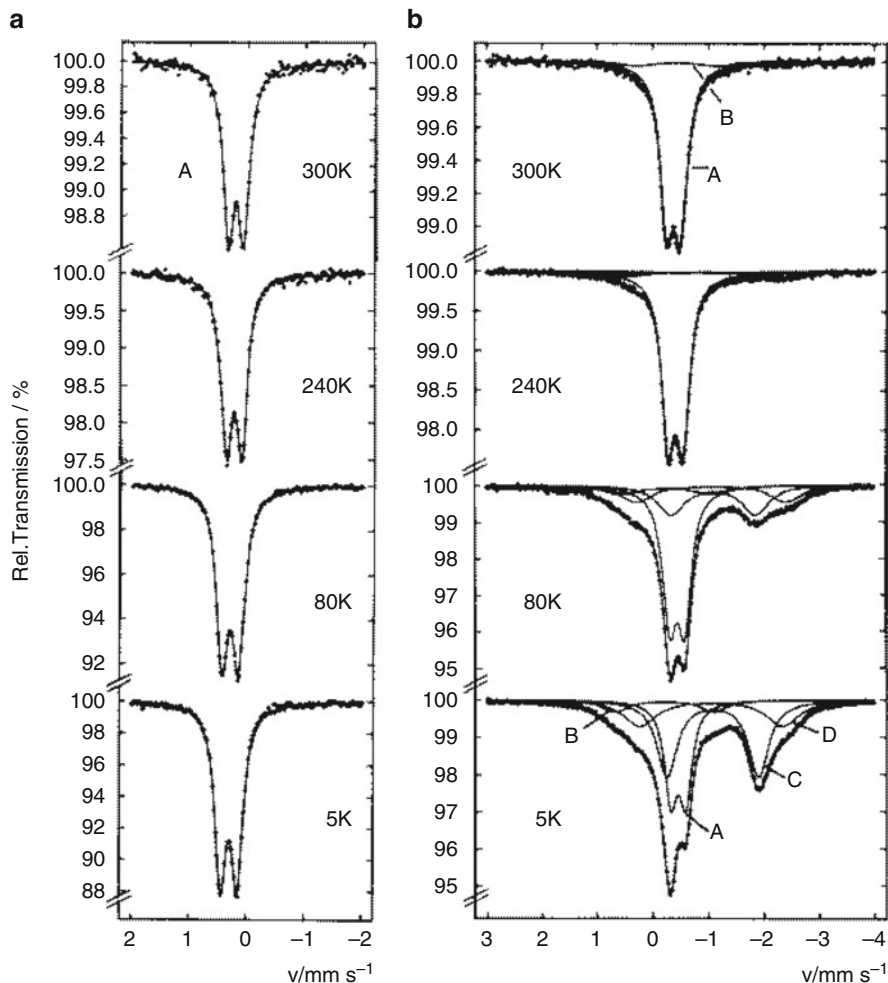


Fig. 8.21 (a, left) ^{57}Fe Mössbauer absorption spectra of $[^{57}\text{Fe}/\text{Co}(\text{phen})_3](\text{ClO}_4)_2$ as a function of temperature versus $^{57}\text{Co/Rh}$ as source (which was kept at 295 K). (b, right) Time-integral ^{57}Fe Mössbauer emission spectra of $[^{57}\text{Co}/\text{Co}(\text{phen})_3](\text{ClO}_4)_2$ as source as a function of temperature versus $\text{K}_4[\text{Fe}(\text{CN})_6]$ as absorber (which was kept at 295 K). Assignment: A, Fe(II)-LS; B, Fe(III)-LS; C, Fe(II)-HS1; D, Fe(II)-HS2. In (a) the source was moved relative to the absorber; in (b) the absorber was moved relative to the fixed source which was mounted in the cryostat. For direct comparison, the sign of the velocities (x-axis) must be changed either in (a) or in (b) (from [48, 50])

HS states by irradiation with light) has contributed to our understanding of the mechanism of the “Nuclear Decay Induced Excited Spin State Trapping (NIESST),” where the nuclear decay process $^{57}\text{Co}(\text{EC})^{57}\text{Fe}$ may be regarded as an “internal” source for molecular excitation.

The mechanism of NIESST is essentially the same as for LIESST (see Fig. 8.10), except for the initial excitation step. The electronic structure of the nucleogenic

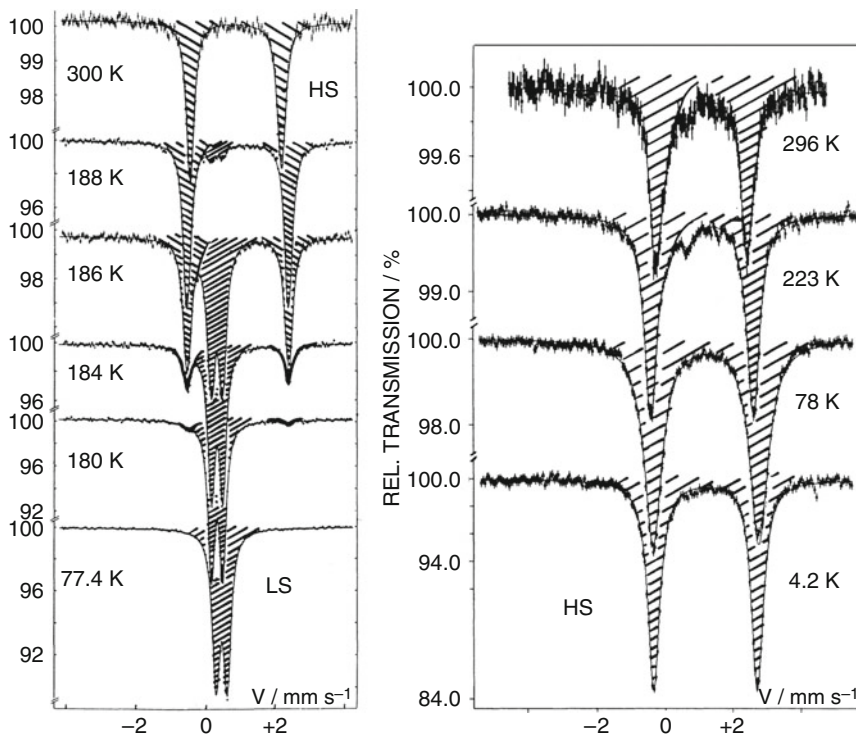


Fig. 8.22 *Left:* ^{57}Fe Mössbauer absorption spectra of $[\text{Fe}(\text{phen})_2(\text{NCS})_2]$ as a function of temperature versus $^{57}\text{Co}/\text{Rh}$ source (which was kept at 295 K). *Right:* Time-integral ^{57}Fe Mössbauer emission spectra of $[^{57}\text{Co}/\text{Co}(\text{phen})_2(\text{NCS})_2]$ as source as a function of temperature versus $\text{K}_4[\text{Fe}(\text{CN})_6]$ as absorber (which was kept at 295 K). Assignment: The quadrupole doublet with the larger quadrupole splitting (ca. 3 mm s^{-1}) refers to the Fe(II)-HS state, and that with the smaller quadrupole splitting (ca. 0.5 mm s^{-1}) to the Fe(II)-LS state (from [43])

^{57}Fe (II) is still highly excited within the Mössbauer time window ($\sim 10^{-7} \text{ s}$ after nuclear decay). The fast ($\ll 10^{-7} \text{ s}$) spin-allowed transitions to the $^1\text{A}_{1g}$ ground state as well as fast intersystem crossing processes ($\ll 10^{-7} \text{ s}$) are favored by spin-orbit coupling (SOC) as in the LIESST mechanism, feeding the metastable $^5\text{T}_{2g}$ state. The branching ratio for the two relaxation pathways (to either $^1\text{A}_{1g}$ or $^5\text{T}_{2g}$) depends on the ligand field strength of the system, in analogy to the observed correlation of the lifetime of the metastable LIESST state and the energy difference ΔE_{HL}^0 , which also depends on the ligand field strength (“reduced energy-gap law”).

Measurements of the lifetimes of NIESST states by time-resolved MES [51] and of LIESST states by time-resolved optical spectroscopy [52] on the very same system (a single crystal of $[\text{Fe}_x\text{Mn}_{1-x}(\text{bpy})_3]^{2+}$ (bpy = bipyridine)) gave similar results. This supports the suggestion that the mechanisms for LIESST and NIESST relaxation are very similar, at least for the low-energy regime. The NIESST effect was also studied in Co(II) SCO compounds, viz. $[^{57}\text{Co}/\text{Co}(\text{terpy})_2]\text{X}_2 \cdot n\text{H}_2\text{O}$ ($X = [\text{ClO}_4]^-$, $n = 1/2$, $X = \text{Cl}^-$, $n = 5$), where terpy is the tridentate ligand terpyridine

[53]. The perchlorate salt shows thermal SCO with $T_{1/2}$ around 200 K and a high-spin fraction of nearly 100% at room temperature, whereas the chloride salt possesses a somewhat stronger ligand field giving rise to thermal ST at much higher temperatures (the HS fraction starts to develop around 200 K, reaches ca. 20% at 320 K and would be expected to increase further) [53]. Conventional Mössbauer absorption measurements were performed on the corresponding systems doped with 5% Fe(II) which was found to be in the LS ($S = 0$) state at all temperatures under study [53]. The emission spectra of the ^{57}Co -labeled cobalt complexes were measured using a home-made resonance detector which operates as conversion-electron detector with count rates 10–20 times higher than those of a conventional detector. At room temperature, the nucleogenic ^{57}Fe ions were found to have relaxed to the stable $^1\text{A}_1$ LS ground state. On lowering the temperature, a doublet from a metastable Fe(II)-HS state appears in the spectra with increasing intensities. The perchlorate derivative with the weaker ligand field strength shows, at comparable temperatures, a considerably higher amount of the Fe(II)-HS fraction than the chloride derivative with the stronger ligand field. The emission spectra recorded at 100 K displayed in Fig. 8.23 demonstrate this effect very clearly. For a comparative study on a related system with even weaker ligand-field strength at the central metal site, temperature-dependent NIESST experiments were carried out with the ^{57}Co -doped high-spin compound $[\text{Mn}(\text{terpy})_2](\text{ClO}_4)_2 \cdot 1/2\text{H}_2\text{O}$. As expected, the ^{57}Fe (II)-HS fraction derived from the emission spectra of the manganese host with the weakest ligand field is the highest one among the three systems Mn/ClO_4 , Co/ClO_4 and Co/Cl at comparable temperatures [53]. It can be seen that ΔE_{HL}^0 , as defined in the relaxation scheme in Fig. 8.10, takes on increasing values in the order

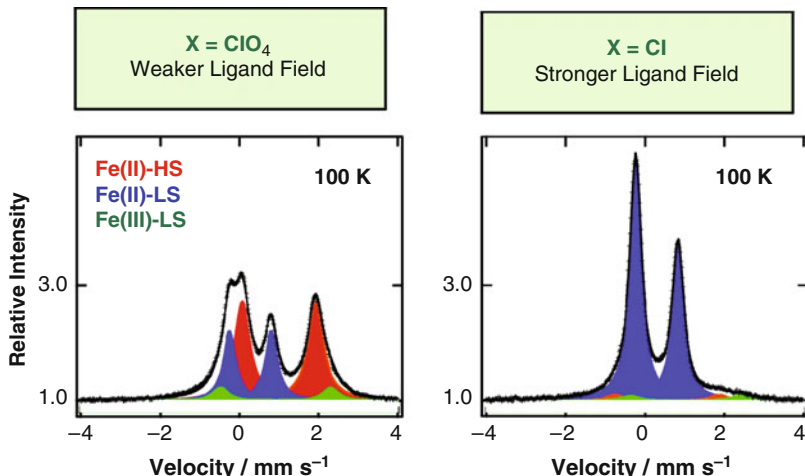


Fig. 8.23 Mössbauer emission spectra of $^{57}\text{Co}/\text{Co}(\text{terpy})_2\text{X}_2 \cdot n\text{H}_2\text{O}$ ($X = \text{ClO}_4^-$, $n = 1/2$; $X = \text{Cl}^-$, $n = 5$) as source material versus $\text{K}_4[\text{Fe}(\text{CN})_6]$ as absorber (which was kept at 298 K) recorded at 100 K with a conversion-electron detector. *Left:* $X = \text{ClO}_4^-$, $n = 1/2$. *Right:* $X = \text{Cl}^-$, $n = 5$ (from [53])

$\text{Mn}/\text{ClO}_4 < \text{Co}/\text{ClO}_4 < \text{Co}/\text{Cl}$ corresponding to the increasing ligand field strength in the same order. The $^{57}\text{Fe}(\text{II})\text{-HS}$ fraction, at a given temperature, decreases in the reverse order, in full agreement with the “reduced energy gap law”.

8.2 ^{57}Fe Mössbauer Spectroscopy: Unusual Spin and Valence States

By far the most utilized Mössbauer isotope is ^{57}Fe , particularly in (bio)inorganic chemistry. Most iron compounds are found in the oxidation states iron(II) and iron(III), either with low-spin or high-spin electron configuration. The literature on the application of ^{57}Fe Mössbauer spectroscopy in this field of research has been reviewed in several textbooks, which are referenced in Chap. 1. The present chapter is intended as a survey of the Mössbauer studies on iron compounds with less common, nevertheless increasingly interesting, valence and spin states.

8.2.1 Iron(III) with Intermediate Spin, $S = 3/2$

The spin-quartet ground state ($S = 3/2$) of trivalent iron (configuration $3d^5$) is often regarded as exotic and marginal, probably because in crystal field theory (CFT), it is explicitly excluded as the ground state for octahedral complexes [54]. However, Gibson et al. reported in 1959 on a square-pyramidal ferric porphyrin chloride complex with EPR signals at $g_{\parallel} = 2$, $g_{\perp} = 3.8$, which Griffith, shortly after, explained by the presence of a ground state with $S = 3/2$ [55]. Some years later, it became obvious from the syntheses and magnetic studies of a series of iron(III) dithiocarbamato-halide complexes that the spin-quartet ground state prevails for several classes of ferric compounds because of their quasi-square-pyramidal geometry [56]. This subject has become a focus of interest during the recent decades partly because biological compounds such as ferricytochrome c' from photosynthetic and denitrifying bacteria [57–62], horseradish peroxidase [60, 63] and the fully oxidized form of cytochrome c oxidase [64] exhibit ground-state properties with spin-admixture, $S = (3/2, 5/2)$. New interest in intermediate-spin complexes arose because several types of the ligands that afford $S = 3/2$ for ferric iron are redox-active and hold promise for versatile new chemistry. Among these dithioleienes are presently experiencing a revival in interest in basic inorganic chemistry and material sciences [65].

8.2.1.1 Ligand Field Considerations

In a simple crystal-field description, a spin-quartet ground state ($S = 3/2$) of iron(III) is energetically stabilized over the spin-sextet ($S = 5/2$) when the energy separation

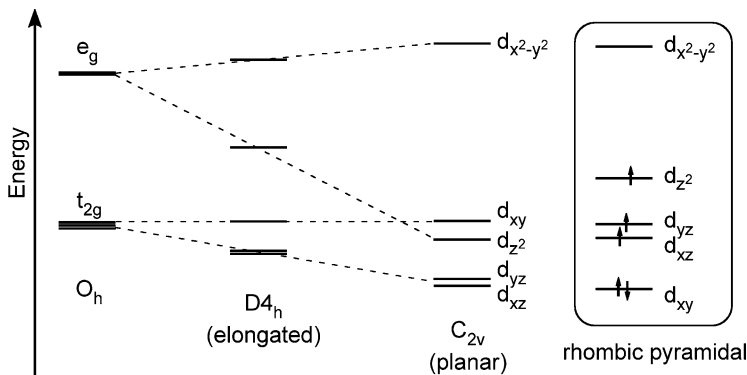


Fig. 8.24 Energy splitting of d -orbitals in an octahedral crystal field and the effect of increasing elongation of the coordination polyhedron along z . The box on the right presents the situation encountered with rhombic monopyramidal iron(III) complexes with $S = 3/2$ [66–68]

of the d -orbitals is such that one orbital lies at higher energy than the other four by a larger amount as compared to Coulomb repulsion and SOC. The five valence d -electrons then occupy only four orbitals (Fig. 8.24). Such an arrangement is afforded in C_{2v} symmetry, when the $d_{x^2-y^2}$ orbital is greatly destabilized by strong-field equatorial ligands and the d_{z^2} orbital remains low in energy because of a weak axial ligand [69]. Electrostatic arguments suggest that the ground-state configuration is $(d_{xy})^2 (d_{yz}, d_{xz})^2 (d_{z^2})^1$ with spin $S = 3/2$ according to Hund's rule [70]. Correspondingly, most ferric intermediate-spin complexes have quasi square-pyramidal symmetry with four strong ligands in the basal plane and a weak fifth one in the apical position; a similar orbital pattern arises for four-coordinate planar complexes.¹

The single-electron crystal-field picture may be a crude over-simplification because Coulomb repulsion and SOC can lead to a situation where the ground term is a composite mixture of $S = 1/2, 3/2$, and $5/2$ states that does not derive from a single configuration [71, 72]; the corresponding physical description is obtained from proper quantum chemical calculations [73–75].

8.2.1.2 Mössbauer Parameters

Intermediate spin occurs mainly for square- and rhombic-pyramidal five-coordinate iron complexes and also for planar four-coordinate and for asymmetric six-coordinate

¹A priori also a linear iron(III) molecule would show a “one-over-four” orbital pattern. Alternatively, a “four-over-one” arrangement could also afford $S = 3/2$ for the d^5 configuration, but this cannot arise from only strong σ -interaction and would need competing strong π -interaction. Neither option has been observed so far.

complexes. The examples with pyramidal symmetry may be further divided into (1) complexes containing 4-sulfur- or 2-sulfur/2-nitrogen donor sets in equatorial positions and (2) complexes with macrocyclic ligands with four nitrogen atoms occupying the equatorial positions. Porphyrinates which also have a N₄-donor set will be described separately because they show a broad variety of phenomena arising from $S = (3/2, 5/2)$ spin admixture.

Square- and Rhombic-Pyramidal Complexes

S_4X Ligand Sphere

Ferric dithiocarbamato complexes have been intensely studied by Mössbauer spectroscopy since the first report on the synthesis and the unusual magnetic properties of iron(III) halide complexes of the type $[\text{Fe}^{\text{III}}(\text{dtc}-\text{R}_2)_2 \text{X}]$, where dtc-R₂ = S₂CNR₂ which is a bis(*N,N'*-dialkyl-dithiocarbamato) ligand with methyl- or ethyl-groups etc. substituting for R, and X = Cl⁻, Br⁻, I⁻ [56]. Throughout this series, iron(III) has four equatorial sulfur-ligands and the halide is in the apical position. The room temperature effective magnetic moments range from 3.98 to $4.01\mu_{\text{B}}$, consistent with three unpaired electrons [56, 76]. The first Mössbauer data, including magnetic spectra recorded at 1.2 K, were reported in 1967 by Wickman for the diethyl chloride derivative, $[\text{Fe}^{\text{III}}(\text{dtc}-\text{Et}_2)_2\text{Cl}]$ (**1**) [70, 77, 78], and later for the isopropyl and other analogs [79–81]. The magnetic properties of the diethyl-chloride derivatives and the 4-morphyl iodide and bromide derivatives, $[\text{Fe}(\text{dtc}-\text{C}_4\text{H}_8\text{O})_2\text{I}]$ (**2**) and $[\text{Fe}(\text{dtc}-\text{C}_4\text{H}_8\text{O})_2\text{Br}]$ (**3**), respectively, have been intensely investigated by ^{57}Fe - and ^{129}I -Mössbauer spectroscopy [82] because the solids exhibit ferromagnetic ordering at liquid helium temperatures [78, 83, 84] and paramagnetic relaxation in the vicinity of the magnetic transition [77, 85]. The Mössbauer spectra of ferric dithiocarbamate complexes, in general, are characterized by relatively large isomer shifts ($\delta \approx 0.50 \text{ mm s}^{-1}$) and large quadrupole splittings, ΔE_Q , close to +3 mm s⁻¹ (Table 8.1). Exchange of the apical halide by thiocyanate, SCN⁻, like in $[\text{Fe}^{\text{III}}(\text{dtc}-\text{Et}_2)_2\text{SCN}]$ (**4**), has only a minor effect on the Mössbauer parameters [86].

Bis(dithiooxalato)ferric complexes, $[\text{Fe}^{\text{III}}(\text{dto})_2\text{X}]^{2-}$ with dto = S₂C₂O₂ and X = I⁻, Br⁻, Cl⁻, respectively (compounds **5–7**), have been studied by magnetic susceptibility, EPR and applied-field Mössbauer spectroscopy, [67]. The isomer shifts at 4.2 K are in the range $\delta \approx 0.25\text{--}0.30 \text{ mm s}^{-1}$ and the quadrupole splittings are larger than +3.25 mm s⁻¹ (Table 8.1).

Coordination compounds of dianionic dithiolene (S₂C₂R₂) and benzene-1,2-dithiolene (bdt = (S₂C₆H₄) and their derivatives have been studied since the 1960s by Mössbauer spectroscopy [87] and other techniques. Nevertheless, many aspects of their electronic structure remained uncertain for a long time. The five-coordinate ferric complexes with two equatorial dithiolene ligands exhibit intermediate spin and show the Mössbauer parameters $\delta = 0.25\text{--}0.38 \text{ mm s}^{-1}$ and $\Delta E_Q = 1.6\text{--}3.2 \text{ mm s}^{-1}$. For example, $[\text{Fe}^{\text{III}}(\text{mnt})_2\text{py}]^{2-}$ with two mnt ligands (=S₂C₂(CN)₂) and an

Table 8.1 Mössbauer parameters of five- and six-coordinate ferric compounds with $S_{\text{Fe}} = 3/2$

Complex	δ^{a} (mm s ⁻¹)	ΔE_Q^{b} (mm s ⁻¹)	η^{c}	$A/g_N\mu_N^{\text{d}}$ (T)	T (K)	Ref.
1 [Fe ^{III} (dtc-Et ₂) ₂ Cl] ⁺	0.50	+2.70	0.2	22.0 ^{e,f}	4.2	[77, 78]
2 [Fe ^{III} (dtc-C ₄ H ₈ O) ₂ I] ⁺	0.48	+2.80	0.1	22.4 ^{e,f}	4.2	[84, 85]
3 [Fe ^{III} (dtc-C ₄ H ₈ O) ₂ Br] ⁺	0.47	+2.72	0.2	26.8 ^{e,f}	4.2	[84, 85]
4 [Fe ^{III} (dtc-Et ₂) ₂ SCN] ⁺	0.42	2.65	—	—	77	[86]
5 [Fe ^{III} (dto) ₂ FeI] ²⁻	0.30	+3.33	0.1	18.2 ^f	4.2	[67]
6 [Fe ^{III} (dto) ₂ Br] ²⁻	0.29	+3.25	0.1	21.0 ^f	4.2	[67]
7 [Fe ^{III} (dto) ₂ Cl] ²⁻	0.25	+3.60	0.2	22.5 ^f	4.2	[67]
8 [Fe ^{III} (mnt) ₂ (idzm)] ⁺	0.36	2.64	—	—	77	[88]
9 [Fe ^{III} (^{Bu} bdt [•])(^{Bu} bdt)(PMe ₃) ₂] ⁺	0.12 ^g	+3.05	0.7	-25.9, -17.7, +0.3	4.2	[92]
10 [Fe(^{Bu} bdt [•]) ₂ (PMe ₃) ₂] ⁺	0.29 ^h	+2.57	0.5	-18.7, -19.6, +1.0	4.2	[92]
11 [Fe ^{III} (^{Bu} bdt) ₂ (^t Bu-py)] ⁺	0.34	+2.94	0	-19.1, -32.2, +1.5	4.2	[92]
12 [^{SS} salen]Fe ^{III} Cl] ⁺	0.38	3.13	—	—	4.2	[93]
13 [Fe(^{Me} iTSC [•]) ₂ (SCH ₃) ₂] ⁺	0.06	2.32	—	—	80	[97]
14 [Fe(^{Me} iTSC [•]) ₂ Cl] ⁺	0.20	2.21	—	—	80	[97]
15 [Fe(^{N,S} IBSQ [•]) ₂]I ⁺	0.12	+3.18	0.5	-7.4, -16.1, +0.6	4.2	[94]
16 [Fe(^{N,O} IBSQ [•]) ₂]I ⁺	0.24	+2.80	0.3	-12.4, -20.3, +1.3	4.2	[94]
17 [Fe ^{III} (^{N,N} IBSQ [•]) ₂]I ⁺	0.15	+3.03	0.2	-9.5, -28.3, +1.8	4.2	[98]
18 [Fe ^{III} (^{N,N} IBSQ [•]) ₂ Ph ₂ Im] ⁺	0.11	+2.26			77	[98]
19 [Et ₄ N] ₂ [FeCl(η^4 -MAC*)] ⁺	0.25	+3.60	0.2	-16.6, -22.0, +5.0	4.2	[100]
20 [(L-N ₄)FeI] ⁺	0.19	+3.56	0	-12.7, -12.7, +0.5	4.2	[68]
21 [Fe(TMCP)(EtOH) ₂]ClO ₄	0.35	3.79	—	—	77	[101]
22 [Fe(OETPP)(THF) ₂]ClO ₄	0.50	3.50	—	—	80	[102]
23 [Fe(L-N ₄ Me ₂)(bdt)]ClO ₄	0.32	2.22	—		200	[103]
24 [Fe ^{III} (^{Bu} bdt [•]) ^{(Bu} bdt)(PMe ₃) ₂] ⁺	0.17	+1.46	0.1	+1.3, -9.9, -30.6	4.2	[92]

^aIsomer shift versus α -iron at RT^bQuadrupole splitting^cAsymmetry parameter^dHyperfine-coupling tensor components in Tesla for the intrinsic spin of iron, $S_{\text{Fe}} = 3/2$ ^eEstimated at 1.2 K due to magnetic self-ordering^fIsotropic part^g0.11 mm s⁻¹ at 80 K^h0.25 mm s⁻¹ at 80 K

apical (N -coordinating) pyridine yields $\delta = 0.33$ mm s⁻¹ at 77 K and $|\Delta E_Q| = 2.41$ mm s⁻¹ [87], and the [Fe^{III}(mnt)₂(idzm)]·2dmf derivative (**8**), where idzm represents the bulky N -coordinating pyridyl ligand, exhibits $\delta = 0.36$ mm s⁻¹, $|\Delta E_Q| = 2.64$ mm s⁻¹ at 77 K [88]. A usually steep drop in μ_{eff} was observed for (**8**) below 10 K, in conjunction with the formation of a new Mössbauer subspectrum, which was interpreted as a $S = 1/2 \leftrightarrow S = 3/2$ ST occurring at $T_{1/2} \sim 3$ K.

Many of the problems and misconceptions occurring for dithiolene compounds are related to the fact that the ligands are redox-active and can be oxidized to monoanionic radicals. Typical examples for this phenomenon are the mono and diradical complexes [Fe^{III}(^{Bu}bdt[•])^{(Bu}bdt)(PMe₃)₂]⁺ (**9**) and [Fe^{III}(^{Bu}bdt[•])₂(PMe₃)⁺ (**10**) for which ^{Bu}bdt and ^{Bu}bdt[•] are *tert*-butyl-dithiolene and its one-electron oxidized form. Originally, these and other bdt derivatives had been described as

iron(IV) and iron(V) compounds [89–91]. Using EPR, Mössbauer and susceptibility measurements, it was however, shown, that iron stays in the ferric intermediate-spin state in all cases, whereas the ligand is oxidized to $\text{bdt}^{\bullet-}$ [92]. The ligand radicals ($S' = 1/2$) interact antiferromagnetically with the spin of the central ferric ion ($S_{\text{Fe}} = 3/2$, $J \gg kT$) and thus, affords a well-isolated ground state with total spin $S_t = 1$ for **9** and $S_t = 1/2$ for **10**. The quartet ground state of iron has been directly observed for $[\text{Fe}^{\text{III}}(\text{^{Bu}bdt})_2(\text{'Bu-py})]^-$ (**11**), which contains the dithiole ligands in their closed-shell form without an interacting radical spin [92]. All of the complexes **9–11** exhibit a single doublet in their zero-field Mössbauer spectra, with isomer shifts ranging from 0.12 to 0.34 mm s^{-1} (Table 8.1). Interestingly, the isomer shift increases slightly upon oxidation **9** → **10**, in contrast to the situation normally expected for a metal-centered oxidation.

S₂N₂X Ligand Sphere

Mixed sulfur and nitrogen donors as encountered with iminothiophenolate ligands also yield intermediate spin ferric complexes. A detailed spectroscopic analysis was necessary to unravel the electronic structure of the bis(*o*-iminothiobenzosemiquinonate) iron(III) complex $[\text{Fe}^{(\text{N,S})\text{IBSQ}^{\bullet}}_2]\text{I}$ (**15**), because this is again a diradical complex with spin $S_t = 1/2$, like in **10**. The ground state here also results from strong antiferromagnetic coupling of the two ligand radicals ($S_{\text{rad}} = 1/2$) to $S_{\text{Fe}} = 3/2$ of the ferric ion [94]. Magnetically split Mössbauer spectra revealed two negative and one positive components of the intrinsic hyperfine tensor of iron ($A/g_N\mu_{\text{N}}(S_{\text{Fe}} = 3/2) = (-7.38, -16.05, +0.60)$ T), similar to the situation found for the complexes **9–11**. The isomer shift of $\delta = 0.12$ mm s^{-1} , and the large positive quadrupole splitting ($\Delta E_Q = +3.18$ mm s^{-1}) corroborate the presence of an intermediate-spin ferric species in **15**.

O₂N₂X Ligand Sphere

Closely related to the above example is the *o*-iminobenzosemiquinonate compound ($[\text{Fe}^{\text{III}}(\text{N,O})\text{IBSQ}^{\bullet}]\text{I}$, **16**), which to the best of our knowledge is the only example of a five-coordinate ferric intermediate-spin complex with oxygen donors in the equatorial plane. Like for its (S_2N_2) analog **15**, both ligands are oxidized π -radicals (monoanions) and the ground state of the molecule corresponds to $S_t = 1/2$. Magnetically split Mössbauer spectra revealed a larger intrinsic field at the iron nucleus ($A/g_N\mu_{\text{N}}(S_{\text{Fe}} = 3/2) = (-12.40, -20.32, +1.30)$ T) and a larger isomer shift value ($\delta = 0.24$ mm s^{-1}) for **16** than for **15**. This reflects the reduced covalency of the $\text{N}_2\text{O}_2\text{I}$ donor set as compared to $\text{N}_2\text{S}_2\text{I}$. Interestingly, the spin state of Fe^{III} in the *chloride* analog of **16** is *high-spin*, whereas for the *bromide* analog, both spin isomers, $S_{\text{Fe}} = 3/2$ and $S_{\text{Fe}} = 5/2$, are present in the crystalline state in a 1:1 ratio [95]. Depending on the type of crystalline state, the bromide complex can also show a $S_{\text{Fe}} = 1/2 \leftrightarrow S_{\text{Fe}} = 3/2$ ST [96].

N₄X Ligand Sphere

The bis(thiosemicarbazide) compounds $[\text{Fe}^{\text{III}}(\text{MeiTSC})_2(\text{SCH}_3)]$ (**13**) and $[\text{Fe}^{\text{III}}(\text{MeiTSC}^\bullet)_2\text{Cl}]$ (**14**) were recently shown to be ferric intermediate-spin complexes with two ligand radicals (${}^{\text{Me}}\text{iTSC}^\bullet$) [97]. The total spin is again $S_t = 1/2$ due to strong antiferromagnetic coupling. The equatorial ligand atoms coordinating to iron are nitrogen, whereas methylthiolate or chloride, respectively, occupy the apical positions. The low isomer shift of $\delta = 0.06 \text{ mm s}^{-1}$ of **13**, in contrast to $\delta = 0.20 \text{ mm s}^{-1}$ for **14**, is explained by an exceptionally strong covalent Fe–SCH₃ bond compared to the lower covalency of the Fe–Cl bond.

The neutral complexes ($[\text{Fe}^{\text{III}}(N,N'\text{IBSQ}^\bullet)_2\text{I}]$, **17**) and ($[\text{Fe}^{\text{III}}(N,N'\text{IBSQ}^\bullet)_2\text{Ph}_2\text{Im}]$, **18**) also possess iron in its ferric intermediate-spin state with the *N,N'*-coordinating equatorial ligands in their monoanionic π -radical form, *o*-diiminobenzosemiquinonate(1–) [98]. The ground state is $S_t = 1/2$ and the Mössbauer parameters are $\delta = 0.16$ and 0.11 mm s^{-1} , and $|\Delta E_Q| = 2.90$ and 2.26 mm s^{-1} , respectively, at 77 K. More examples of such complexes are found in [98].

The classical compound [⁵⁵Fe] $(\text{salen})\text{Fe}^{\text{III}}\text{Cl}$] (**12**) exhibits an effective magnetic moment of $3.90 \mu_B$ and the Mössbauer isomer shift and quadrupole splitting recorded at 4.2 K are $\delta = 0.38 \text{ mm s}^{-1}$ and $|\Delta E_Q| = 3.13 \text{ mm s}^{-1}$ [93]. Other five-coordinate intermediate-spin ferric complexes with four equatorial N donor atoms have macrocyclic ligands, such as $[\text{Fe}^{\text{III}}(\text{Ph}_2[16]\text{N}_4)(\text{SPh})]$, where [16]N₄ is a 16-member tetraaza macrocycle ligand ($\delta = 0.26 \text{ mm s}^{-1}$, $|\Delta E_Q| = 1.93 \text{ mm s}^{-1}$ at 300 K, [99]). More recently, the electronic structure of $[\text{Et}_4\text{N}]_2[\text{Fe}^{\text{III}}\text{Cl}(\eta^4\text{-MAC}^*)\text{-CH}_2\text{Cl}_2]$ (**19**) was investigated by comprehensive EPR- and applied-field Mössbauer spectroscopy [100] revealing the typical feature of two large negative magnetic hyperfine coupling components and one small positive component: $A/g_N\mu_N = (-16.6, -22.0, +5.0) \text{ T}$.

The intermediate-spin ground state of the ferric compounds published by Jäger and coworkers is also stabilized by a N₄-macrocyclic ligand, [N₄]^{2–} which exist in different varieties of substitutions. The apical ligands are weakly coordinating halides or pseudohalides, such as iodide in the case of $[\text{Fe}^{\text{III}}(\text{N}_4)\text{I}]$ (**20**) [68]. The electronic structure was elucidated by EPR, Mössbauer and DFT studies.

Six-Coordinate Complexes

Most six-coordinate iron(III) compounds with a spin-quartet ground state are highly nonplanar porphyrinates like the strongly ruffled chiroporphyrin $[\text{Fe}(\text{TMCP})(\text{EtOH})_2\text{ClO}_4]$ (**21**) [101] or the saddle-shaped compound $[\text{Fe}(\text{OETPP})(\text{THF})_2\text{ClO}_4]$ (**22**) [102]. The Mössbauer parameters for these two examples are $\delta = 0.35 \text{ mm s}^{-1}$, $|\Delta E_Q| = 3.79 \text{ mm s}^{-1}$ at 77 K, and $\delta = 0.50 \text{ mm s}^{-1}$, $|\Delta E_Q| = 3.50 \text{ mm s}^{-1}$ at 80 K, respectively. More information on porphyrinates is presented in the paragraph below dealing with spin admixture.

A remarkable nonporphyrin complex is the highly distorted compound $[\text{Fe}(\text{L-N}_4\text{Me}_2)(\text{bdt})]\text{ClO}_4 \cdot \text{H}_2\text{O}$ (**23**) [103] which undergoes a very gradual ST from

a spin-doublet state persisting below 50 K to a spin-quartet state at ambient temperature. The X-band EPR recorded in MeCN/toluene displays a rhombic signal with $g^{\text{eff}} = 5.50, 1.86, 1.40$ consistent with a large rhombicity parameter E/D for the quartet state. The intermediate-spin ferric species shows $\delta = 0.32 \text{ mm s}^{-1}$, $|\Delta E_Q| = 2.22 \text{ mm s}^{-1}$ at 200 K.

The octahedral iron complex $[\text{Fe}^{\text{III}}(^{\text{Bu}}\text{bdt}^{\bullet})(^{\text{Bu}}\text{bdt})(\text{PMMe}_3)_2]$ (**24**) plays a particular role among the quasi octahedral complexes because it has two strong trimethyl phosphine ligands and shows virtually D_2 symmetry without much tetragonal distortion of the iron coordination. The ground-state spin is $S_t = 1$. An array of complementary spectroscopic data had been invoked to show that **24** contains an intermediate-spin ferric iron and one $\text{bdt}^{\bullet-}$ radical and one dianion bdt^{2-} ligand (PMMe_3 is neutral) [92]. The spin-triplet ground state arises from antiparallel coupling of the iron spin $S_{\text{Fe}} = 3/2$ and the ligand-radical spin $S_{\text{rad}} = 1/2$. The ground state exhibits large ZFS ($D_t = +14.35 \text{ cm}^{-1}$, $E/D = 0.02$) which, converted to local values of iron, yields $D_{\text{Fe}} = +9.57 \text{ cm}^{-1}$. Applied-field Mössbauer spectra reveal an anisotropic A tensor with a very large negative A_{zz} component and rather small A_{xx} and A_{yy} components: $A/g_N\mu_{\text{N}}(S_{\text{Fe}} = 3/2) = (+1.25, -9.88, -30.58) \text{ T}$. The Mössbauer parameters $\delta = 0.17 \text{ mm s}^{-1}$, $\Delta E_Q = +1.46 \text{ mm s}^{-1}$ and $\eta = 0.1$ resemble those of the rhombic planar compounds, though ΔE_Q is rather small.

Common Features and Electronic Structures

Intermediate-spin ferric complexes have been found for rhombic pyramidal and distorted octahedral complexes containing strong equatorial and weak axial ligands. The equatorial ligands comprise: thiocarbamates, thiooxolates, thiosalen, thiosemicarbazides, benzenedithiolates, iminothiobenzosemiquinonates, and $[\text{N}_4]\text{-}$ macrocycles, porphyrines and tetraazaporphyrines, which mostly have sulfur and nitrogen as coordinating atoms. Among the axial ligands are halides, $(\text{SbF}_6)^-$, $(\text{ClO}_4)^-$, H_2O , THF, Et_2O , halogenocarbonane $(\text{CB}_{11}\text{H}_6X_6)^-$ and carbonane $(\text{CB}_{11}\text{H}_{12})^-$ monoanions or, in a few cases, pyridines and thiolates.

Mössbauer isomer shifts are found between 0.06 and 0.50 mm s^{-1} at 80 K, with a clear statistical prevalence for $\delta \approx 0.3 \text{ mm s}^{-1}$. A typical feature of $S_{\text{Fe}} = 3/2$ compounds is a large quadrupole splitting up to 4.38 mm s^{-1} with positive V_{zz} (main component of the EFG). Moreover, the rhombic-pyramidal compounds are characterized by anisotropic magnetic hyperfine tensors with relatively large A_{xx} and A_{yy} components of about -18 to -26 T , and a small or even slightly positive A_{zz} component. ZFS of the spin quartet is usually large, on the order $2\text{--}20 \text{ cm}^{-1}$, with either a positive or a negative sign of D .

In a crystal-field picture, the electronic structure of iron in the five-coordinate compounds is usually best represented by a $(d_{xy})^2(d_{yz}, d_{xz})^2(d_{z^2})^1$ configuration [66, 70], as convincingly borne out by spin-unrestricted DFT calculations on the “Jäger compound” **20** [68]. The intermediate spin configuration with an empty $d_{x^2-y^2}$ orbital in the CF model, however, has a vanishing valence contribution to the

EFG. Early extended Hückel calculations suggested that the large quadrupole splitting of the spin-quartet ground state is entirely caused by covalency effects. The recent DFT molecular-orbital calculations by Grodzicki et al. [68] corroborate this conclusion and specify particularly the covalent contribution of the otherwise, in the crystal-field picture, completely empty $d_{x^2-y^2}$ orbital as the origin of a large quadrupole splitting of **20**. The shape of the magnetic orbitals, $(d_{yz}, d_{xz})^2 (d_{z^2})^1$, renders a large spin-dipole contribution caused by the corresponding elongated spin-density distribution as the origin of the *A*-anisotropy of the five-coordinate ferric spin-quartet compounds.

8.2.1.3 Spin Admixture $S = (5/2, 3/2)$ in Porphyrinates: A Special Case?

The ground state of five-coordinate *high-spin* iron(III)-porphyrinates sometimes cannot be properly described by a pure $S = 5/2$ state. The classical examples are, as mentioned above, ferricytochrome c' and horseradish-peroxidase [60, 63]; a recent review on corresponding synthetic porphyrinates is found in [104]. These ferric compounds display magnetic moments between 5.8 and $4\mu_B$ at room temperature [64, 69, 105–111], curved Curie–Weiss plots [107, 112], very low EPR effective g_\perp values of 4.2–5.8 and large ZFS of more than 10 cm^{-1} [107, 109, 110, 113, 114], large temperature changes of the NMR chemical shift of the pyrrole protons [109, 112, 115, 116], and large Mössbauer quadrupole splittings $\Delta E_Q = 2.2\text{--}4.1\text{ mm s}^{-1}$ with isomer shifts $\delta = 0.38\text{--}0.43\text{ mm s}^{-1}$ at 4.2 K [69, 104, 107, 109, 110, 113, 114, 117, 118]. All these properties are distinct from those of $S = 1/2$ and $S = 5/2$ iron(III) porphyrinates and indicate that the spin state of the iron(III) is a coherent superposition (not a thermal mixture) of the $S = 3/2$ and $S = 5/2$ states.

Maltempo adapted the theoretical approach worked out by Harris [71] to explain the unusual spectroscopic data by a simplified model using quantum-mechanical mixing of the excited spin-quartet state (4A_2) into the sextet ground state (6A_1), caused by SOC [57, 59]. The energy gap between these states necessary to explain this observation is of the order of the SOC constant ($200\text{--}400\text{ cm}^{-1}$). The situation, in general, results from the coordination of weak-field axial ligand(s) that cause the porphyrinate core to contract, thereby destabilizing the $d_{x^2-y^2}$ orbital to the point where the $S = 3/2$ spin state becomes lowest in energy. *The actual ground state of iron(III) porphyrinates can be on either side of this crossover, that is, either largely $S = 3/2$ or $S = 5/2$* [114].

Spin-admixed ($S = 3/2, 5/2$) iron(III) porphyrinates are mostly observed when weak-field counter-anions are coordinated as axial ligands, such as ClO_4^- , $\text{B}_{11}\text{CH}_{12}^-$, SbF_6^- , BF_4^- , PF_6^- , $\text{C}(\text{CN})_3^-$, or SO_3CF_3^- [104, 116] (Table 8.2). The degree of spin admixture, however, also depends on the 2,6-substituents of the phenyl rings of tetraphenyl porphyrins [116]. Spin admixture has also been observed in six-coordinate complexes such as iron(III)octaethylporphyrinate *bis*-ligated by 3,5-dichloropyridine [113, 118] or 3-chloropyridine [119] and in iron(III) tetraazaporphyrins. Additionally, the spin-admixed state exists in some five-coordinate iron(III) phthalocyanines [120]. The first truly four-coordinate ferric heme

Table 8.2 Mössbauer parameters of some five- and the first truly four-coordinate ferric porphyrinates with admixed spin $S = (3/2, 5/2)$

Compound ^a	δ ^b (mm s ⁻¹)	ΔE_Q ^c (mm s ⁻¹)	Temp. (K)	% ($S = 3/2$) ^d	Ref.
Fe(TPP)(B ₁₁ CH ₁₂)(C ₇ H ₈)	0.33	4.12	4.2	92	[111]
Fe(TPP)(ClO ₄) (0.5 <i>m</i> -xylene)	0.38	3.50	4.2	65	[107]
Fe(TPP)(FSbF ₅)·C ₆ H ₅ F	0.39	4.29	4.2–77	98	[123]
Fe(OETPP)Cl	0.35	0.92	280	4–10	[124]
Fe(OEP)ClO ₄	0.40	3.54	4.2	100	[125]
Fe(TPP)(CF ₃ SO ₃)	—	2.39	200	30	[126]
[Fe(TipsiPP)] ⁺ [CB ₁₁ H ₆ Br ₆] ^{−e}	0.33	5.16	6	100	[121]

^aTPP tetraphenyl porphyrin, OETPP 2,3,7,8,12,13,17,18-octaethyl-5,10,15,20-tetraphenylporphyrin, OEP octaethylporphyrin, TipsiPP 5,10,15,20-tetrakis(2',6'-bis(triisopropylsiloxy)phenyl)-porphyrin (in short: bis-pocket siloxyl porphyrin)

^bIsomer shift versus α -iron at RT

^cQuadrupole splitting

^dDerived from EPR g-values

^eIron in [Fe(TipsiPP)]⁺ is four-coordinated

with the extremely hindered *bis*-pocket siloxyl porphyrin (HTipsiPP) shows, as expected, *pure intermediate spin* $S = 3/2$ [121].

An interesting example of a spin-admixed nonheme iron(III) complex with $S = (3/2, 5/2)$ ground state is the organometallic anion $[\text{Fe}^{\text{III}}(\text{C}_6\text{Cl}_5)_4]^-$ which has four pentachloro phenyl ligands in tetrahedrally distorted planar symmetry [122].

8.2.2 Iron(II) with Intermediate Spin, $S = 1$

8.2.2.1 Square-Planar Iron(II) Compounds

The planar complex of iron(II)-phthalocyanine, FePc, was the first example of an iron(II) compound ($3d^6$ configuration) for which a $S = 1$ ground state has been established. Phthalocyanine is a macrocyclic ligand with a planar N₄ set of donor atoms resembling the core of a porphyrin. The magnetic susceptibility of FePc has been measured by Klemm [127] who reported a value of $3.96\mu_{\text{B}}$ (Bohr magnetons) at room temperature, and later by Lever who found $3.85\mu_{\text{B}}$ for a highly purified powder of FePc [128]. Both values are considerably larger than the spin-only value of $2.83\mu_{\text{B}}$ for $S = 1$ ($\mu_{\text{eff}} = g \cdot [S(S + 1)]^{1/2}$) but, nevertheless, the temperature-dependence of the magnetic data could be readily explained by the presence of a spin-triplet ground state, $S = 1$. Strong SOC partly restores the orbital momentum and yields large ZFS (see Chap. 4.7) as well as a large (average) g-factor for the Zeeman interaction; the corresponding spin Hamiltonian parameters are found in the range of $D = 64\text{--}70\text{ cm}^{-1}$ and $g_{\text{av}} = 2.61\text{--}2.74$ [129, 130]. Essentially, the magnetic properties of FePc can be reasonably well explained in a crystal field (CF) model by mixing of the spin-triplet ground state with excited spin-triplet and

spin-quintet states under the influence of SOC. Probably the best CF description invokes an energetically split 3E ground state, according essentially to a $(d_{xy})^2, (d_{xz}, d_{yz})^3, (d_{z^2})^1, (d_{x^2-y^2})^0$ ground-state configuration [129–131]. Apparently, the $d_{x^2-y^2}$ orbital is destabilized by strong in-plane σ -interaction affording a one-over-four arrangement of valence d -orbitals as expected for a planar compound.

Metal complexes of phthalocyanine still attract much attention, mostly because of a wide range of applications, such as catalysts, dyes, optical switches, but more recently also because of their magnetic properties, particularly the iron complex FePc [132]. The “flat” molecules can aggregate in the solid and form chains of the so-called herringbone type with various properties. FePc crystallizes in an α - [133] and a β -form [134], which may explain many of the magnetic properties reported for FePc. The α -form which is most interesting for applications shows spontaneous magnetic ordering at low temperatures with a remarkably strong internal field of 66.2 T at the Mössbauer nucleus at 1.3 K due to sizable intermolecular spin coupling (a record value for an $S = 1$ system) [132]. In contrast, the β -form is paramagnetic and shows vanishing magnetization below 10 K because of the large (positive) ZFS of the triplet, providing a $M_s = 0$ ground state [129, 130].

A remarkable number of Mössbauer studies have been published since the first spectra reported in 1966 [135], most of them performed on the β -form when not specified differently [131, 132, 136–139]. Also, high pressure has been applied [140] and thin films were prepared [141]. Because of the ambiguity concerning the crystalline phase, the values of the hyperfine parameters show some dispersion. The isomer shift, $\delta = 0.4\text{--}0.6 \text{ mm s}^{-1}$, is found in between the typical values known for high-spin iron(II) and low-spin iron(II). The quadrupole splitting is large, $\Delta E_Q = 2.4\text{--}3.0 \text{ mm s}^{-1}$ (Table 8.3), as one might expect because of the unusual non-cubic symmetry. Applied-field measurements revealed positive V_{zz} .

Interestingly, a CF model invoked for the basic interpretation of the magnetic properties can explain reasonably well the quadrupole splitting, including the weak temperature dependence. (Note, the valence contribution to the EFG as it can be inferred for the basic $(d_{xy})^2, (d_{xz}, d_{yz})^3, (d_{z^2})^1, (d_{x^2-y^2})^0$ configuration of the 3E ground state has its main component along the x -axis of the crystal field: $V_{xx,\text{val}} = +4/7e\langle r^{-3} \rangle$, $V_{yy,\text{val}} = V_{zz,\text{val}} = -2/7e\langle r^{-3} \rangle$, as can be inferred from Table 4.3). However, a major contribution from covalent bonding has been noted. Recent quantum chemical calculations on intermediate-spin phthalocyanines are found in [142].

Four-coordinate iron(II)-porphyrins also show an intermediate-spin ($S = 1$) ground state. The classical examples are the tetraphenyl, TPP, and octaethyl, OEP, derivatives, whose effective magnetic moments are about $4.2\mu_B$ at room temperature [143]. The magnetic properties of these planar complexes (with S_4 symmetry due to ruffling of the N₄-ligand plane for Fe(TPP)), studied by magnetic susceptibility, paramagnetic NMR [144, 145], and applied-field Mössbauer measurements [146–149], are compatible with a $^3A_{2g}$ ground state in a crystal field model arising from a $(d_{xy})^2, (d_{z^2})^2, (d_{xz}, d_{yz})^2$ configuration, mixed by SOC with an excited 3E_g state, $(d_{xy})^2, (d_{z^2})^1, (d_{xz}, d_{yz})^3$. Other suggestions for the ground state are 3E_g and $^3B_{2g}$ [150]. More recent Mössbauer studies were performed with iron(II) octaethyltetrazaporphyrin, Fe(OETAP), which shows magnetic ordering in the

Table 8.3 Mössbauer parameters of iron(II) complexes with intermediate spin ($S = 1$)

Compounds	Temp. (K)	δ (mm s $^{-1}$)	ΔE_Q (mm s $^{-1}$)	Ref.
Fe(Pc)	4	0.49	+2.70	[136]
Fe(Pc)	77	0.51	+2.69	[136]
Fe(Pc)	293	0.40	+2.62	[136]
Fe(Pc), α -phase	4.2	0.46	+2.52	[132]
Fe(TPP)	4.2	0.52	+1.51	[148]
α -Fe(OEP)	4.2	0.59	+1.60	[147]
Fe(OETAP)	4.2	0.3	+3.09	[151]
porphyrinogen ^a	4.2	0.35	2.34	[152]
Fe(octaaza[14]annulene) ^b	78	0.19	+4.13	[156]
(AsPh ₄) ₂ [Fe(II)bdt ₂]	4.2	0.44	+1.16	[157]
(N(C ₂ H ₅)) ₂ [Fe(II)bdt ₂]	4.2	0.45	+1.21	[158]

^aA porphyrinogen is a reduced tetrapyrrole parent compound of a porphyrin

^bThe true electronic structure might be Fe(III) with intermediate spin ($S_{\text{Fe}} = 3/2$), antiferromagnetically coupled to a ligand radical ($S' = 1/2$)

solid with a large internal field of 62.4 T at the Mössbauer nucleus [151]. Iron(II)-porphyrinogens represent another group of quasi square-planar iron(II) complexes with $S = 1$ ground state [152].

Both Fe(II)(TPP) and Fe(II)(OEP) have positive electric quadrupole splitting without significant temperature dependence which, however, cannot be satisfactorily explained within the crystal field model [117]. Spin-restricted and spin-unrestricted X_α multiple scattering calculations revealed large asymmetry in the population of the valence orbitals and appreciable $4p$ contributions to the EFG [153] which then was further specified by ab initio and DFT calculations [154, 155].

Four-coordinate iron(II) complexes of porphyrin-derivatives, so-called porphyrinogens, show similar properties as the square planar porphyrins [152], whereas the macrocyclic N₄-donor ligand octaaza[14]annulene affords a planar iron(II) complex with a particularly low isomer shift, $\delta = 0.19$ mm s $^{-1}$. Since this value is significantly lower than the typical values for planar iron(II) complexes given in Table 8.3, one may presume that the ligand is not innocent and has oxidized the metal center so that the true electronic structure is better described by iron(III) intermediate-spin ($S = 3/2$) antiferromagnetically coupled to a ligand radical located on the one-electron reduced ligand in its trianion form.

Four-coordinate, planar iron(II)-dithiolate complexes also exhibit intermediate spin. The first example described was the tetraphenylarsonium salt of the square-planar bis(benzene-1,2-dithiolate)iron(II) dianion, (AsPh₄)₂[Fe(II)bdt₂], which showed $\delta = 0.44$ mm s $^{-1}$ and $\Delta E_Q = 1.16$ mm s $^{-1}$ at 4.2 K [157]. The electronic structure of a different salt was explored in depth by DFT calculations, magnetic susceptibility, MCD measurements, far-infra red spectroscopy and applied-field Mössbauer spectroscopy [158].

The four-coordinate iron(II) complex of cycloheptatrienyldiene is a rare example of a fully reversible singlet ($S = 0$ at 6 K) to triplet ($S = 1$ at 293 K) transition in the slow relaxation regime [159].

Six-Coordinate Iron(II) Complexes

König and others published in the 1970s an impressive series of studies on six-coordinate iron(II)-bis-phenanthroline complexes [160–164] for which they inferred $S = 1$ from thorough magnetic susceptibility and applied-field Mössbauer measurements. Criteria for the stabilization of the triplet ground state for six-coordinate compounds with tetragonal (D_{4h}) and trigonal (D_{3d}) symmetry were obtained from LFT analyses [163]. The molecular structures, however, were not known because the materials could not be crystallized.

Elaborate studies finally revealed that the composition of the solid material in reality was not $\text{Fe}(\text{II})\text{-}(\text{phenanthroline})_2\text{-}X$, as presumed previously, where X is a dianionic ligand like oxalate or malonate, but a so-called mixed-valence “double-salt” of $[\text{Fe}(\text{II})(\text{phen})_3]_2$ and $[\text{Fe}(\text{III})(\text{dianion})_3]$ with $(1/2\text{-dianion})^*\text{xH}_2\text{O}$ [164, 165]. The iron(II) compounds are low-spin ($S = 0$) and the iron(III) species are high-spin ($S = 5/2$), and the superposition of the magnetic moments of both centers accounts for the “effective” triplet signal. Most annoying, the Mössbauer spectra of the paramagnetic iron(III) species turned out to be broadened beyond recognition because of intermediate-spin relaxation. Their contribution was completely missed and the Mössbauer spectra, reported as those of iron(II) with $S = 1$, are, in reality, the spectra of the low-spin iron(II) species only ($\delta \sim 0.3 \text{ mm s}^{-1}$, $\Delta E_Q \sim 0.25 \text{ mm s}^{-1}$ [162]). It took the authors almost a decade to uncover the true nature of these systems (which might be a lesson for every spectroscopist). In conclusion, we can state that, partly in contrast with textbook knowledge (e.g., [16] in Chap. 1), iron(II) with intermediate spin $S = 1$ has been unambiguously identified only for four-coordinate (mainly planar) compounds.

8.2.3 Iron in the High Oxidation States IV–VI

Iron centers that are more electron-deficient than iron(III) compounds are used for efficient and highly specific oxidation reactions in, for example, heme and nonheme enzymes [166–172]. Most iron(IV)-complexes found in biological reaction cycles possess terminal or bridging oxo groups as is known from a large number of structural and spectroscopic investigations. With the exception of iron(IV)-nitrido groups, nonoxo iron(IV) centers very rarely take part in such reactions.

The enzymatic reactions of peroxidases and oxygenases involve a two-electron oxidation of iron(III) and the formation of highly reactive $[\text{Fe}=\text{O}]^{3+}$ species with a formal oxidation state of +V. Direct (spectroscopic) evidence of the formation of a genuine iron(V) compound is elusive because of the short life times of the reactive intermediates [173, 174]. These species have been safely inferred from enzymatic considerations as the active oxidants for several oxidation reactions catalyzed by nonheme iron centers with “innocent,” that is, redox-inactive, ligands [175]. This conclusion is different from those known for heme peroxidases and oxygenases

which show a separation and delocalization of the two oxidation equivalents formally stored on one $[\text{Fe}=\text{O}]^{3+}$ unit. Upon oxidation, one of the two electrons is removed from iron(III) and one from the porphyrin ligand forming an iron(IV)-oxo species and a porphyrin (ligand) radical [176–178]. The reaction intermediate, called compound-I, was initially discovered because of its unusual and intense green color [179] appearing after a two-electron oxidation [180, 181]. In the next step of the reaction cycle of peroxidases, the red so-called compound-II is formed by a one-electron back-reduction of the radical, leaving the iron(IV)-oxo group in the ferryl state [182]. In some cases of modified heme proteins, when a redox-active amino acid like tyrosine is close to the iron, another organic radical (instead of the porphyrin radical) can be formed in conjunction with the iron(IV)-oxo group [183]. Although examples of oxidation states higher than iron(V) are elusive in biological systems, the whole range of high-valent iron sites have been intensely studied with synthetic compounds, as will be shown below.

Iron(IV), (V), and (VI) centers are also found in solid-state materials, the coordination chemistry of which is of considerable interest because unusual structures and remarkable electronic and catalytic properties are encountered [184]. Reviews of the corresponding Mössbauer properties are found in [185–187].

8.2.3.1 Crystal-Field Ground States

High-valent iron can occur in a wide variety of electronic configurations. Figure 8.25 (a-c, e-i) presents a summary of the corresponding one-electron crystal-field states for the $3d^4$, $3d^3$, and $3d^2$ electron configurations, allocated to HS and LS states in distorted octahedral and tetrahedral symmetry. Part d, in addition, depicts the case of “low-low-spin” iron(IV) found in some trigonal

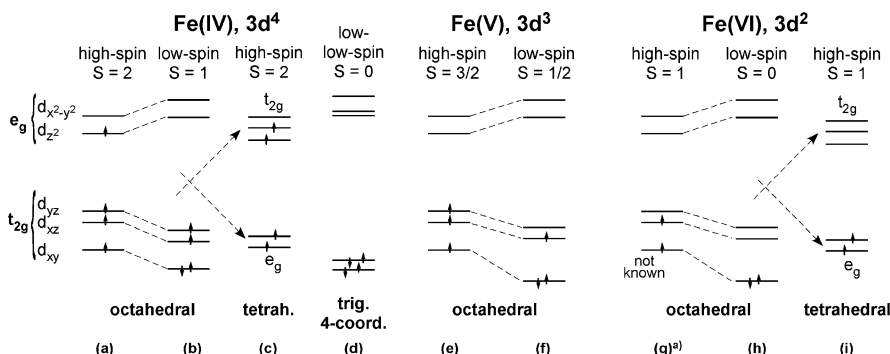


Fig. 8.25 Schematic presentation of the one-electron crystal-field states for the $3d^4$, $3d^3$, and $3d^2$ electron configurations of iron(IV), (V), and (VI). ^aCase (g) has not been observed yet

compounds. We note that in solid-state materials, only HS states are observed (parts a, c, e, and i).

8.2.3.2 Iron(IV) Oxides

The chemistry of iron(IV) in solid-state materials and minerals is restricted to that of oxides, since other systems such as iron(IV)-halides are not stable [186]. Iron(IV) oxides are easy to handle because they are usually stable in air, but they often have a substoichiometric composition, with oxygen vacancies contributing to varying degrees. Moreover, the samples may contain different amounts of iron(III) in addition to the intended iron(IV) oxide, a complication which may obscure the Mössbauer data [185]. Even iron(V) was found in iron(IV) oxides due to temperature-dependent charge disproportionation [188, 189].

The Mössbauer parameters of several iron(IV) compounds are summarized in Table 8.4. The calcium, barium, and strontium perovskites CaFeO_3 [188], BaFeO_3 [190] and SrFeO_3 [189, 191], together with their various modifications containing mixed metal ions and different oxygen content, are probably the best investigated systems among the iron(IV) oxides [185]. In perovskites, iron(IV) is coordinated by six oxygen atoms yielding spin $S = 2$, arising from the $t_{2g}^3 e_g^1$ configuration (Fig. 8.25, case a). The isomer shift (relative to α -iron) is about $+0.1 \text{ mm s}^{-1}$ at 4.2 K and the quadrupole splitting is practically zero, as expected for iron in a cubic lattice site [185]. Octahedral oxoferrates, such as $\text{Sr}_{0.5}\text{La}_{1.5}\text{Li}_{0.5}\text{Fe}_{0.5}\text{O}_4$, have isomer shifts at 4.2 K in the range of -0.12 to -0.08 mm s^{-1} [185].

More recently, tetrahedral $\text{Fe(IV)}\text{O}_4^{4-}$ anions have been found in the barium-rich iron oxides Ba_2FeO_4 and Ba_3FeO_5 . The fragment is high spin, $S = 2$, according to the tetrahedral coordination (Fig. 8.25, case c) and yields an isomer shift of about -0.15 mm s^{-1} at 80 K and -0.24 mm s^{-1} at room temperature and a quadrupole splitting of 0.3 – 0.4 mm s^{-1} [187].

8.2.3.3 Iron(IV) in Metalloproteins and Coordination Compounds

The archetypical and spectroscopically best investigated example of a heme peroxidase is horseradish peroxidase (HRP). Moss et al. have shown by Mössbauer spectroscopy that compound-I and compound-II of HRP both possess the same oxidation state of iron [182]. Later, the corresponding iron(IV) and particularly the iron(IV)-radical states have been studied in great detail, revealing much insight into the electronic interaction of both paramagnetic sites, the iron and the porphyrin radical [63]. The iron(IV)-oxo group is in the LS state, $S = 1$, throughout in all heme systems. The isomer shifts and quadrupole splittings for HRP and chloroperoxidase (CPO), are summarized in Table 8.4.

Table 8.4 Mössbauer parameters of iron(IV) compounds^a

Compound	CN ^b	Spin ^c	Temp. (K)	δ (mm s ⁻¹)	ΔE_Q (mm s ⁻¹)	Ref.
(1) Solid-state oxides						
SrFeO_3	6	2	4.2/300	0.11/0.07	<1.w. ^d	[191]
$\text{Sr}_{0.5}\text{La}_{1.5}\text{Li}_{0.5}\text{Fe}_{0.5}\text{O}_4$	6	2	4.2	-0.08	<1.w. ^d	[192]
$\text{Ba}_2\text{FeO}_4 / \text{Ba}_3\text{FeO}_5$	4	2	85/78	-0.15/-0.14	0.36/0.39	[187]
(2) Fe(IV) hemes						
HRP-II	6	1	4.2	0.03	+1.61	[63]
HRP-I	6	1	4.2	0.08	+1.25	[193]
CPO-I	6	1	4.2	0.14	+1.02	[194]
$[(\text{TMP})\text{Fe}=\text{O}]^+$	6	1	4.2	0.08	+1.62	[195, 196]
$[\text{TPP}(2,6-\text{Cl})\text{Fe}=\text{O}]^+$	5?	1	4.2	0.08	+1.8	[196]
$[(\text{TMP})\text{Fe}^{\text{IV}}(\text{OCH}_3)_2]$	6	1	4.2	-0.025	2.10	[197]
Catalase (high pH, $\text{Fe}^{\text{IV}}=\text{O}$)	6	1	4.2	0.03	2.29	[198]
Catalase (low pH, $\text{Fe}^{\text{IV}}=\text{OH}$)	6	1	4.2	0.07	1.47	[198]
$(\text{FeTPP})_2\text{N}$	5?	1?	131	0.18	1.08	[199]
$(\text{FeTPP})_2\text{C}$	5?	1?	131	0.10	1.88	[199]
$(\text{FeTPP})_2\text{CCl}_2$	5?	1?	131	0.10	2.28	[199]
(3) Nonheme compounds						
$[(\text{cyc-ac})(\text{ACN})\text{Fe}=\text{O}]^+$	5?	1	4.2	0.01	+1.37	[200]
$[\text{Fe}=\text{O}(\text{TMC})(\text{NCCH}_3)](\text{OTf})_2$	6	1	4.2	0.17	+1.24	[201]
$[\text{Fe}^{\text{IV}}(\text{O})(\text{TPA})]^{2+}$	5/6?	1	4.2	0.01	+0.92	[202]
TauD, intermediate J	6	2	4.2	0.30	-0.88	[203]
$[(\text{H}_2\text{O})_5\text{Fe}^{\text{IV}}=\text{O}]^{2+}$	6	2	4.2	0.38	-0.33	[204]
$[\text{Fe}^{\text{IV}}(\text{O})(\text{TMG}_3\text{tren})]^{2+}$	5	2	4.2	0.09	-0.29	[205]
RNR, R2 intermediate X	6	2	4.2	0.26	-0.6	[206]
MMO, intermediate Q	6	2	4.2	0.17	0.53	[207]
$[(9\text{-janeN}_3)\text{Fe}^{\text{III}}(\text{O})$ $(\text{CH}_3\text{CO}_2)_2\text{Fe}^{\text{IV}}(9\text{-janeN}_3)]^{3+}$	6	2 35%, 1 65%	4.2	-0.10	+0.86, +1.14	[208]
L(cat) $[\text{Fe}^{\text{III}}-\text{N}\equiv\text{Fe}^{\text{IV}}](\text{cat})\text{L}$	6	1	77	0.09	+0.81	[209, 210]
L(cat) $[\text{Fe}^{\text{IV}}=\text{N}=\text{Fe}^{\text{IV}}](\text{cat})\text{L}]^+$	6	1	77	0.04	+1.55	[209, 210]
$[\text{PhBP}^R_3]\text{Fe}\equiv\text{N}$, $R = i\text{Pr}$, CH_2Cy	4	0	140	-0.34	6.01	[211]
$[(\text{TIMEN}^{\text{mes}})\text{Fe}\equiv\text{N}]^+$	4	0	77	-0.27	6.04	[212]
$[\text{Fe}(\text{NTs})(\text{N}_4\text{Py})]^{2+}$	6	1	4.2	0.02	+0.98	[213]
$[\text{Fe}(\text{O})(\text{N}_4\text{Py})]^{2+}$	6	1	4.2	-0.04	+0.93	[213]
(4) Nonoxo, nonnitrido compounds						
$[\text{Fe}(\text{oetpp})(\text{C}_6\text{H}_5)]^+$	5	1	4.2	0.13	+3.23	[214]
$[\text{Fe}^{\text{IV}}\text{Cl}(\eta^4\text{-MAC}^*)]^-$	5	2	4.2	-0.02	+0.89	[100]
$[(\text{Me}_3\text{cyclam}-\text{acetate})\text{Fe}^{\text{IV}}\text{Cl}]^{2+}$	6	1	80	0.08	+2.40	[215]
$[(\text{Me}_3\text{cyclam}-\text{acetate})\text{Fe}^{\text{IV}}\text{F}]^{2+}$	6	1	80	0.02	+2.43	[215]
$[(\text{Me}_3\text{cyclam}-\text{acetate})\text{Fe}^{\text{IV}}\text{N}_3]^{2+}$	6	1	80	0.11	+1.92	[216]
$[\text{N}_3\text{N}']\text{FeCN}$	5	0	180	-0.22	3.28	[217]

^aHRP horseradish peroxidase, CPO chloroperoxidase, TMP chloro-5,10,15,20-tetra(mesityl)porphyrin, TPP(2,6-Cl) tetra(2,6-dichlorophenyl)porphyrin, cyc-ac cyclam-acetate = 1,4,8,11-tetramethyl-1,4,8,11-tetraaza-cyclotetradecane-1-acetate, ACN = (NCCH₃), TMG₃tren = N(CH₂CH₂N=C(NMe₂)₂)₃, which is based on the (tren)-backbone (=tris(2-ethylamino)amine) and has a set of three superbasic tetramethylguanidine (=TMG) N-donor atoms, RNR ribonucleotide reductase, MMO methane monooxygenase, L = 1,4,7-trimethyl-1,4,7-triazacyclononane, cat = (tetrachlorocatechol)⁴⁻, PhBP^R = tris(phosphino)borate, R = isopropyl, TIMEN^R = tris[2-(3-aryl-imidazol-2-ylidene)ethyl]amine, R = mesityl (mes), $\eta^4\text{-MAC}^* = 1,4,8,11\text{-tetraaza-13,13diethyl-2,2,5,5,7,7,10,10-octamethyl-3,6,9,12,14 pentaoxocyclotetradecane}$, $[\text{N}_3\text{N}']^{3-} = [(t\text{-BuMe}_2\text{ SiNCH}_2\text{CH}_2\text{N})]^3$

^bCoordination number

^cSpin of the iron(IV) site

^dLess than the natural line width; materials are magnetic and exhibit a six-line spectrum at low temperatures without appreciable quadrupole interaction

A typical feature of the Mössbauer spectra of five- or six-coordinate iron(IV) with an axial oxo group (or a OCH_3 , a nitrido or a imido group) is a low isomer shift ($+0.1 \pm 0.15 \text{ mm s}^{-1}$), a large and positive quadrupole splitting ($1\text{--}2 \text{ mm s}^{-1}$), an anisotropic hyperfine coupling tensor with moderately large values for $A_{xx}/g_{\text{N}}\mu_{\text{N}}$ and $A_{yy}/g_{\text{N}}\mu_{\text{N}}$ (-16 to -23 T) and a rather small value for $A_{zz}/g_{\text{N}}\mu_{\text{N}}$ (0 to -10 T) and also a large positive ZFS ($D = 5\text{--}35 \text{ cm}^{-1}$). In many cases, the applied-field Mössbauer spectra of iron(IV) hemes and model compounds could be simulated by using a correlation of the electronic g - and D -values which is obtained from a perturbation treatment of ligand field theory [194, 218]. This is, however, not generally justified because the perturbation model neglects the so-called spin-flip contributions to the ZFS [219] (see Chap. 5).

Heme Iron(IV) Oxo Centers

The interesting electronic and catalytic properties of the heme enzymes have stimulated intense studies on synthetic porphyrin compounds with a large variety of possible modifications aiming for the preparation of systematic spectroscopic or functional probes. Some typical examples of synthetic iron(IV)-porphyrin models are summarized in Table 8.4. Interestingly, the one-electron oxidation of an iron (III) porphyrin can also be ligand-based, forming an porphyrin-cation radical that is exchange-coupled to iron(III). At least three types of iron(III)-porphyrin-radical complexes have been observed; high-spin iron(III) antiferromagnetically or ferromagnetically coupled to the radical affording total spin $S_t = 2$ and $S_t = 3$ ground states, respectively [220–222], and low-spin iron(III) antiferromagnetically coupled to the radical [223]. Experiments with different metal ions and porphyrin-ligand systems indicate that the energy of the metal d - and porphyrin π -orbitals controls the type of oxidation which is either metal- or ligand-based. It appeared that alkoxides, but not methanol, perchlorate or imidazole, are sufficiently strong π -donating ligands to stabilize iron(IV) in porphyrins with respect to iron(III)-porphyrin-cation radicals [197]. The iron(IV) complex $[(\text{TMP})\text{Fe}^{\text{IV}}(\text{OCH}_3)_2]$ is included in Table 8.4 as an example.

Moreover, it has been recognized that protonation of the $\text{Fe}^{\text{IV}}=\text{O}$ group induces an increase of the quadrupole splitting with respect to the nonprotonated form. As a typical example, we mention the low-pH and high-pH forms of catalase from *Proteus mirabilis* [198] in Table 8.4.

One of the amazing and still not perfectly understood differences in the electronic structures of the biomimetic models on one side and the biological systems on the other side is the strength and the sign of the exchange coupling between the ferryl iron ($S_{\text{Fe}} = 1$) and the porphyrin radical ($S_{\text{rad}} = 1/2$) in the respective compound-I states. The interaction always appears to be ferromagnetic for the model compounds ($S = 3/2$ ground state) irrespective of how distorted the respective porphyrins are, whereas the enzymes show very weak and anisotropic magnetic coupling (HRP-I) or appreciable antiferromagnetic coupling with $S = 1/2$ ground

state (CPO). Reviews of applied-field Mössbauer investigations on the heme enzymes are found in [117, 224].

Nonheme Iron(IV) Oxo Centers

Iron(IV) also occurs as an intermediate in the reaction cycle of a large family of *nonheme* enzymes that have in their resting state a catalytic mononuclear iron(II) center for the activation of oxygen and the oxidation of their substrates [169, 175, 225, 226]. The iron is coordinated by three protein ligands, two histidine, and one aspartic or glutamic acid, with three further sites for additional coordination. This (His)₂–(Asp/Glu) motif is known as “facial triad” [227]. The first iron(IV)–oxo intermediate of this type was characterized by Mössbauer spectroscopy in a transient state of taurine: α KG dioxygenase (called TauD). The species was trapped by *rapid-freeze quench* technique. This intermediate, named **J**, has a ground state with spin $S = 2$ with large, almost axial ZFS ($D = 10.5 \text{ cm}^{-1}$) and an isomer shift of $\delta = 0.30 \text{ mm s}^{-1}$ and a quadrupole splitting of $\Delta E_Q = -0.88 \text{ mm s}^{-1}$ [203, 228]. Spectroscopy-biased DFT studies on a number of possible model structures suggested for intermediate **J** either trigonal-bipyramidal or octahedral iron coordination [229]. In the meantime, the high-valent species has been thoroughly characterized for four enzymes, and in all instances, the iron(IV) center was found to be high-spin, $S = 2$ [203, 230–232].

The first nonheme iron(IV)–oxo complex, $[(\text{cyclam-acetato})\text{Fe}^{\text{IV}}=\text{O}]^+$, was generated by the ozonolysis of a $[(\text{cyclam-acetato})\text{Fe}(\text{III})(\text{O}_3\text{SCF})]^+$ precursor. Its Mössbauer study yielded $\delta = 0.01 \text{ mm s}^{-1}$ and $\Delta E_Q = 1.37 \text{ mm s}^{-1}$ [200], but the exact molecular structure could not be determined. Subsequently, it was found that the corresponding Fe(IV)–oxo complex with the ligand TMC = Me₄cyclam ($[\text{Fe}=\text{O}(\text{TMC})(\text{NCCH}_3)](\text{OTf})_2$) was sufficiently stable that it could be crystallized to obtain its molecular structure by X-ray diffraction [201]. Since then, the number of known iron(IV)–oxo compounds has increased [233–235], and some have also been investigated by Mössbauer spectroscopy [236–238]. In one case, where the high-valent state has been generated by the reaction of Fe(II) with hypochloride in CH₃CN, the terminal ligand of Fe(IV) is presumably a methoxy group ($\delta = 0.03 \text{ mm s}^{-1}$ and $\Delta E_Q = 1.21 \text{ mm s}^{-1}$ at 4.2 K) [239].

All but two of the known synthetic iron(IV)–oxo compounds are low-spin, $S = 1$ [202, 240]. The first example of an iron(IV)–oxo model compound with spin $S = 2$ was the quasioctahedral complex $[(\text{H}_2\text{O})_5\text{Fe}^{\text{IV}}=\text{O}]^{2+}$ ($\delta = 0.38 \text{ mm s}^{-1}$, $\Delta E_Q = 0.33 \text{ mm s}^{-1}$) which was obtained by treating $[\text{Fe}^{\text{II}}(\text{H}_2\text{O})_6]^{2+}$ with ozone in acidic aqueous solution [204]. The spin state of iron in this type of structure is determined by the energy gap between the $d_{x^2-y^2}$ and the d_{xy} orbitals [241]. The weak water ligands induce a sufficiently small gap being less than the spin paring energy and stabilizing the HS state (Fig. 8.25, case a).

The second example of a high-spin iron–oxo complex, $[\text{Fe}^{\text{IV}}(\text{O})(\text{TMG}_3\text{tren})]^{2+}$ (see Table 8.4) has been published only recently. In this compound, the HS state is afforded by the trigonal bipyramidal symmetry of the TMG₃tren ligand, causing

degeneracy of the d_{xy} and $d_{x^2-y^2}$ orbitals [205]. The differences in the electronic structures of high-spin and low-spin compounds matter because of the consequences for the reactivity of the complex [229].

The R2 protein of class I ribonucleotide reductase (RNR R2) and methane monooxygenase (MMO) are typical examples of enzymes with a diiron center in the active site. Their catalytic functions rely on the formation of two key intermediates, **X** and **Q**, respectively, with highly oxidized iron. Intermediate **X** of RNR contains a mixed-valent $\text{Fe}^{\text{III}}\text{--O--Fe}^{\text{IV}}$ unit [206, 242], whereas **Q** has a so-called $\text{Fe}^{\text{IV}}\text{--}(\mu\text{-O}_2)\text{--Fe}^{\text{IV}}$ diamond core [243]. Intermediate **X** is oxidized by one equivalent above the diferric resting R2 state, involving high-spin Fe(III) (d^5 , $S = 5/2$) and high-spin Fe(IV) (d^4 , $S = 2$). The Mössbauer parameters are $\delta = 0.56 \text{ mm s}^{-1}$ and $\Delta E_Q = -0.9 \text{ mm s}^{-1}$ for the ferric and $\delta = 0.26 \text{ mm s}^{-1}$ and $\Delta E_Q = -0.6 \text{ mm s}^{-1}$ for the ferryl site. Antiferromagnetic exchange produces the observed $S = 1/2$ ground state with distinct EPR and Mössbauer properties [206]. The homovalent cluster of the MMO intermediate **Q** contains two identical ferryl sites; their local spin is $S = 2$ and the Mössbauer parameters are $\delta = 0.17 \text{ mm s}^{-1}$ and $\Delta E_Q = 0.53 \text{ mm s}^{-1}$ [172, 207, 244].

High-Valent Iron Dimers

The two iron(III) sites in MMO and RNR-R2, are bridged by a (μ -oxo) group and two (μ -carboxylato) groups [245, 246]. Upon oxidation, the diiron core is converted into a localized mixed-valent iron(III)-iron(IV) dimer as characterized by high-resolution molecular-structure studies of biomimetic model compounds [208] (and references therein). Of particular interest were site-selective Mössbauer measurements on structurally related compounds which contain mixed-metal clusters of the type $(\text{Fe}^{\text{III}}\text{--Cr}^{\text{III}})$ and $(\text{Cr}^{\text{III}}\text{--Fe}^{\text{IV}})$. The g -values, ZFS, and exchange interaction parameters could be determined in detail and were related to structural features via DFT calculations [208]. Interestingly, the iron(IV) site coordinated by the neutral synthetic N_3 -donating ligand ($[9]\text{aneN}_3$) and the (μ -oxo)(μ -carboxylato)₂ bridges exhibits thermal spin-equilibrium. Corresponding to this observation, the trication $[(9)\text{aneN}_3] \text{ Fe}^{\text{III}}(\text{O})(\text{CH}_3\text{CO}_2)_2 \text{ Fe}^{\text{IV}}([9]\text{aneN}_3)]^{3+}$ measured in frozen CH_3CN solution exhibits the superpositions of two EPR spectra and of two types of magnetic Mössbauer spectra, respectively. The superpositions are related with the two different spin states of iron(IV). In one case (ca. 35%), the iron(IV) site is in the HS state, $S = 2$, and in the other (ca. 65%), it is in the LS state, $S = 1$. The corresponding Mössbauer parameters are summarized in Table 8.4. Since the iron (III) site is in the HS state, $S = 5/2$, the total spin of the two antiferromagnetically coupled spin-isomers is $S_t = 1/2$ and $S_t = 3/2$, respectively.

High-valent iron also occurs in μ -nitrido bridged dimers with linear $[\text{Fe}^{\text{III}}\text{--N}\equiv\text{Fe}^{\text{IV}}]^{4+}$ and $[\text{Fe}^{\text{IV}}=\text{N}=\text{Fe}^{\text{IV}}]^{5+}$ cores [209, 210] (and references therein). Such compounds have been prepared first by thermolysis [247] or photolysis [248] of iron(III)-porphyrin complexes with an azide ligand, $(\text{N}_3)^-$. Mixed-valent iron-nitrido porphyrin dimers exhibit valence delocalization as can be inferred from the

unique Mössbauer spectra showing isomer shifts in the range $\delta = 0.08\text{--}0.18 \text{ mm s}^{-1}$ [249, 250]). At the same time, the dimers show $S = 1/2$ ground state due to very strong antiferromagnetic spin coupling. This is somewhat mysterious because valence delocalization as the result of double-exchange interaction should stabilize HS states [251–253].

On the contrary, ligands such as 1,4,7-trimethyl-1,4,7-triazacyclononane ($=\text{Me}_3[9]\text{ane}$) yield localized valences for the $[\text{Fe}^{\text{III}}-\text{N}\equiv\text{Fe}^{\text{IV}}]^{4+}$ core with a total spin of $S_t = 3/2$, arising from strong antiferromagnetic coupling ($-J > 150 \text{ cm}^{-1}$) of high-spin ($S = 5/2$) iron(III) and low-spin ($S = 1$) iron(IV); the Mössbauer parameters of the latter are $\delta = 0.09 \text{ mm s}^{-1}$ and $\Delta E_Q = 0.81 \text{ mm s}^{-1}$. The homovalent oxidation product with a $[\text{Fe}^{\text{IV}}=\text{N}=\text{Fe}^{\text{IV}}]^{5+}$ core is diamagnetic up to room temperature ($-J > 200 \text{ cm}^{-1}$), showing Mössbauer parameters $\delta = 0.04 \text{ mm s}^{-1}$ and $\Delta E_Q = 1.55 \text{ mm s}^{-1}$ [209]. DFT calculations have provided insight into the electronic structure and exchange pathways within the diiron core of these compounds [210].

Mononuclear Iron(IV)-Nitrido and -Imido Compounds

A mononuclear iron-nitride group has recently been suggested a constituent of the cofactor catalyzing biological nitrogen reduction by nitrogenase [254]. In order to gain further insight into the structure of iron-nitride complexes and their reactivity, a number of model compounds with terminal $\text{Fe}=\text{NR}$ and $\text{Fe}\equiv\text{N}$ groups have been synthesized and spectroscopically characterized [211, 255–257]. An exciting achievement has been the preparation and characterization of distorted tetrahedral iron(IV)-nitrido complexes [257], in which the $\text{Fe}=\text{N}$ unit is coordinated by a polydentate ligand with three soft donor groups, either three phosphine ligands in the case of $[\text{PhBP}_3^{\text{R}}]\text{Fe}\equiv\text{N}$ [211, 258, 259] or three N -heterocyclic carbene groups in the case of $[(\text{TIMEN}^{\text{R}})\text{Fe}\equiv\text{N}]^+$ [212] and another variant [260]. In these complexes, because of the pseudotetrahedral symmetry with strong trigonal distortion at the iron site, the valence d -orbitals of the iron are widely split in a “three-over-two” pattern such that the four valence electrons are accommodated in the low-lying nonbonding e -orbitals, that is, d_{xy} and $d_{x^2-y^2}$ [260]. Therefore, these compounds are diamagnetic, $S = 0$ (the state which is called the “low-low-spin” state of the d^4 configuration). As a consequence of the preferential population of nonbonding d -orbitals rather than antibonding orbitals, the Fe–N distances are very short (151–155 pm, [212, 259]), the Fe–N vibration frequencies are high ($\nu(\text{Fe}\equiv\text{N}) \approx 1,000 \text{ cm}^{-1}$), and the species have high reactivity toward nucleophiles [257]. The d^4 configuration causes an unprecedentedly large EFG at the Mössbauer nucleus. Although not determined, one may presume a positive sign for V_{zz} because of the huge (positive) valence contribution to the EFG expected for four electrons in the two “planar” orbitals d_{xy} and $d_{x^2-y^2}$. The observed quadrupole splitting is 6.01 mm s^{-1} for $[\text{PhBP}^{i\text{Pr}}_3]\text{Fe}\equiv\text{N}$ [211] and 6.04 mm s^{-1} for $[(\text{TIMEN}^{\text{mes}})\text{Fe}\equiv\text{N}]^+$ [212], which are the largest ever observed for an iron compound.

The corresponding isomer shifts are -0.31 mm s^{-1} (at 140 K) and -0.27 mm s^{-1} (at 77 K), respectively.

In analogy to the iron(IV)-oxo unit, the iron(IV)-imido unit (Fe(IV)=NR) has been proposed as the reactive intermediate of isolobal amination reactions catalyzed by iron [213, 261]. A model compound for such a species is the tosylimido analog of a nonheme iron(IV)-oxo complex $[\text{Fe(NTs)(N4Py)}]^{2+}$ ($\text{N4Py} = N,N\text{-bis}(2\text{-pyridylmethyl})\text{bis}(2\text{-pyridyl)methylamine}$, $\text{NTs} = \text{mesityl-}N\text{-tosylimide}$). In contrast to related porphyrin-imido compounds, which contain an iron(II) center, $S = 2$ ($\delta = 0.72 \text{ mm s}^{-1}$, $\Delta E_Q = 1.51 \text{ mm s}^{-1}$) [262], the Mössbauer parameters of this nonheme complex are indicative of an iron(IV) species ($\delta = 0.02 \text{ mm s}^{-1}$, $\Delta E_Q = +0.98 \text{ mm s}^{-1}$, $S = 1$, $D = 29 \text{ cm}^{-1}$). The parameters are very close to those of the analogous iron(IV)-oxo complex $[\text{Fe(O)(N4Py)}]^{2+}$ ($\delta = -0.04 \text{ mm s}^{-1}$, $\Delta E_Q = +0.93 \text{ mm s}^{-1}$, $S = 1$, $D = 22 \text{ cm}^{-1}$) [213]. More examples of iron(IV)-imido compounds are reviewed in [257].

Nonoxo-, Nonnitrido-Iron(IV) Compounds

While most examples of genuine iron(IV) species utilize bridging or terminal oxo or nitrido ligands, high-valent complexes without these groups are quite rare. To our knowledge, the only well-characterized mononuclear Fe(IV)-*heme* complex without an oxo ligand is the phenyl-iron derivative, $[\text{Fe(oetpp)}\text{C}_6\text{H}_5]\text{SbCl}_6$, generated from the phenyl-iron(III) complex $\text{Fe(III)(oetpp)}\text{C}_6\text{H}_5$ by oxidation with an organic radical, $[\text{C}_{12}\text{H}_8\text{OS}]\text{SbCl}_6$ (oetpp = 2,3,7,8,12,13,17,18-octaethyl-5,10,15,20-tetraphenylporphyrin) [214]. The compound exhibits an isomer shift of $\delta = 0.13 \text{ mm s}^{-1}$ and a quadrupole splitting of $\Delta E_Q = +3.23 \text{ mm s}^{-1}$. Applied-field measurements revealed large ZFS ($D \approx 30 \text{ cm}^{-1}$) and axially symmetric magnetic hyperfine parameters that are consistent with iron(IV), $S = 1$, but definitively exclude the possible alternative of iron(III) and an oxidized porphyrin. A similar iron site has been recently observed for the reactive oxidized state of the enzyme MauG which utilizes two covalently bound c-type hemes to catalyze the synthesis of the so-called cofactor tryptophan–tryptophylquinone. It was proposed that the enzyme stores two oxidation equivalents in a highly oxidized pair of a heme Fe(IV)=O group ($\delta = 0.06 \text{ mm s}^{-1}$, $\Delta E_Q = 1.70 \text{ mm s}^{-1}$) and a heme Fe(IV) nonoxo species ($\delta = 0.17 \text{ mm s}^{-1}$, $\Delta E_Q = 2.54 \text{ mm s}^{-1}$) [263].

The first well-characterized mononuclear *nonheme* Fe(IV) complex without an oxo or nitrido ligand is $[\text{Fe}^{\text{IV}}\text{Cl}(\eta^4\text{-MAC}^*)]^-$ ($\text{H}_4[\text{MAC}^*] = 1,4,8,11\text{-tetraaza-13,13diethyl-2,2,5,5,7,7,10,10-octamethyl-3,6,9,12,14-pentaoxocyclotetradecane}$) where iron is coordinated by a plane of four amide-nitrogen anions from a macrocyclic ligand and one axial chloride ligand [100, 264]. Its spin is $S = 2$ with small negative ZFS ($D = -2.6 \text{ cm}^{-1}$) as inferred from EPR and applied-field Mössbauer measurements [100]. For a short review of high-valent iron complexes with the $\eta^4\text{-MAC}^*$ ligand, including Fe(IV) species with $S = 1$, see [265].

The iron(IV) state in $[(\text{Me}_3\text{cyclam-acetate})\text{FeX}]^{2+}$, $\text{X} = \text{Cl}^-, \text{N}_3^-, \text{F}^-$, [215, 216] is stabilized by the five-coordinating macrocyclic ligand ($\text{Me}_3\text{-cyclam-acetate})^-$

which is a variant of cyclam-acetate (mentioned earlier) with three additional methyl groups [215, 266, 267]. A full spectroscopic investigation of these compounds (and their related Fe(III) and Fe(II) derivatives) by applied-field Mössbauer studies and DFT calculations showed that the spin state of iron(IV) is $S = 1$ and that the energy of the single-electron valence orbitals increases in the order $d_{xy} < d_{xz} \approx d_{yz} < d_{x^2-y^2} < d_{z^2}$, as expected from ligand field theory [215]; the Mössbauer parameters are collected in Table 8.4. Note the increased isomer shift and reduced quadrupole splitting of the fluoro complex within the series which reflects the fact that the iron(IV)-fluoro group is an “isoelectronic twin” of the iron (IV)-oxo compounds listed above.

The first well characterized “low–low-spin” iron(IV) compound ($S = 0$) is the complex $[\text{N}_3\text{N}'\text{FeCN}]$ ($\delta = -0.22 \text{ mm s}^{-1}$, $\Delta E_Q = 3.28 \text{ mm s}^{-1}$) [217], where $[\text{N}_3\text{N}']^{3-}$ represents the trianionic triamido-amine ligand $[(t\text{-BuMe}_2\text{SiNCH}_2\text{CH}_2\text{N})]^{3-}$. The three bulky amido substituents form a “pocket” and protect the metal site leaving only the apical position open for functional reactions. The “low–low-spin” state arises from trigonal bipyramidal ligand-field symmetry which provides a “three-over-two” orbital splitting with two energetically low-lying e orbitals.

Corroles and Other Noninnocent Ligands

There has been a longstanding debate in the literature on the electronic structure of chloro-iron corroles, especially for those containing the highly electron-withdrawing *meso*-tris(pentafluorophenyl)corrole (TPFC) ligand [268–270]. Two alternative electronic structures were proposed for this and for the related Fe (TDCC)Cl (TDCC = *meso*-tris(2,6-dichlorophenyl)corrole) complex, that is, a high-valent ferryl species ($S = 1$) chelated by a trianionic corrolato ligand (Fe (IV)Cor $^{3-}$) or an intermediate-spin ferric iron ($S = 3/2$) that is antiferromagnetically coupled to a dianionic π -radical corrole (Fe(III)Cor $^{2-}$) yielding an overall spin-triplet ground state ($S_t = 1$). A combined experimental (Mössbauer) and computational (DFT) investigation of two series of corrole-based iron complexes finally reached the following conclusion: “The electronic structures of FeXCor (X = F, Cl, Br, I, Cor = TPFC, TDCC) are best formulated as (Fe(III)Cor $^{2-}$), similar to chloro-iron corroles containing electron-rich corrole ligands” [271]. Antiferromagnetic exchange between Fe(III) ($S = 3/2$) and the corrole radical ($S' = 1/2$) afforded by a singly occupied Fe– d_{z^2} and corrole a_{2u} -like π -orbitals, leads to the observed spin-triplet ground state, $S_t = 1$. The coupling constants exceed those of analogous porphyrin systems by a factor of 2–3. In the corroles, the combination of lower symmetry, extra negative charge and smaller cavity size (relative to the porphyrins) leads to exceptionally strong iron-corrole σ -bonds. Hence, the Fe– $d_{x^2-y^2}$ -based molecular orbital is unavailable in the corrole complexes (contrary to the porphyrin case), and the local spin state is $S_{\text{Fe}} = 3/2$ in the corroles versus $S_{\text{Fe}} = 5/2$ in the porphyrins. Since these results clearly rule out the

presence of iron(IV), corrole complexes cannot be included in the list of high-valent compounds assembled here.

Similarly, the stable densely colored oxidation products of many iron(III) compounds with ligands which are known or may be suspected to be noninnocent, that is, redox-active, such as dithiocarbamate (dtc), phenanthroline (phen), dithiocarbazone and particularly dithiolate (mnt, bdt, etc.) and their various derivatives, have been assigned to iron(IV) species in the past [186]. However, recent work (still in progress) based on high-resolution structure determination, EPR, Mössbauer and XAS spectroscopy, magnetic susceptibility measurements and DFT calculations unambiguously shows that the electronic structure of such systems is actually much better described by iron(III) and a ligand radical, or even iron(II) and two ligand radicals [74, 92, 272–275]. Therefore, we refrain from reviewing such highly oxidized coordination compounds with noninnocent ligands in this section. Instead, some example from the previous list of falsely assigned “iron(IV) complexes” [186] are mentioned in the paragraph on iron(III) intermediate-spin complexes (see for instance, compounds **9**, **10** [92] in Table 8.1).

8.2.3.4 Iron(V) Compounds

Genuine iron(V) is a very rare oxidation state. In the preparation of iron oxides (and of other solid-state materials), the intended iron(V) disproportionates mostly into an iron(III) fraction and two parts of an iron(VI) fraction [276]. The only example of an iron(V) oxide for which the Mössbauer parameters are known [185] is $\text{La}_2\text{Li}\text{FeO}_6$. A low isomer shift of $\delta = -0.41 \text{ mm s}^{-1}$ was observed at room temperature with practically zero quadrupole splitting [277], which was taken as a proof that iron is accommodated in octahedral FeO_6 sites surrounded by six Li ions. Although repeatedly cited, it seems that the spectra have never been published, and the data must therefore be considered with care.

Iron-porphyrin complexes of biological as well as synthetic origin do not attain the iron(V) state, because the porphyrin is not innocent and takes one of the two oxidation equivalents with respect to the iron(III) state. Recently, however, an optically detected intermediate generated by laser flash photolysis of a mutant of cytochrome P-450 was tentatively assigned to an iron(V)-oxo species [278]. In contrast, a nonheme iron(V)-oxo unit has been proposed, since long to be the oxidant in the large family of Rieske dioxygenases [169]. However, only a single genuine iron(V)-oxo compound has been synthesized to date with the redox-innocent tetraniomic macrocyclic tetraamido (TAML) ligand B* (B* is related to $\eta^4\text{-MAC}$ mentioned above [265]). The ligand provides four exceptionally strong amide-N σ -donor groups, which are capable of stabilizing iron(V) when an iron(III) precursor complex is treated with an oxygen-transfer agent such as a peroxy acid forming $[\text{B}^*\text{Fe}^{\text{V}}(\text{O})]^-$ [173]. The presence of a $3d^3$ configuration was verified using Mössbauer spectroscopy ($\delta = -0.42 \text{ mm s}^{-1}$ at 4.2 K (-0.46 mm s^{-1} at 140 K), $\Delta E_Q = 4.25 \text{ mm s}^{-1}$), EPR spectroscopy ($S = 1/2$, $g = [1.99, 1.97, 1.74]$), K-edge XAS and EXAFS spectroscopy. The molecular structure could not be characterized

because of the thermal instability of the compound, but spectroscopy-biased DFT calculations provide a convincingly detailed description of the perferryl state of the iron [173].

Resonance Raman studies yielded the first indication of the formation of an iron (V)-nitrido species obtained by the photolysis of a porphyrin-iron(III) azide precursor by the Raman laser [279–281]; the product, however, could never be obtained in an otherwise detectable amount. Further spectroscopic evidence for the formation of an iron(V) species was possible for the $\text{Fe}(\text{V})\equiv\text{N}$ group stabilized by the redox-innocent ligands of the cyclam type [282]. Comprehensive studies were performed on the complex $[(\text{cyclam-ac})\text{Fe}^{\text{V}}\equiv\text{N}]^+$ using K-edge XAS and EXAFS measurements, magnetic susceptibility, Mössbauer spectroscopy, and nuclear inelastic scattering in conjunction with DFT calculations [200, 255, 283]. These studies characterize the electronic structure of the compound as a low-spin ($d_{xy}^2(d_{xz}, d_{yz})^1$) system with a formal bond order for $\text{Fe}\equiv\text{N}$ of 2.5, leaving significant radical character on the nitrogen atom [255, 257]. The electron configuration yields essentially an E ground state which is subjected to Jahn–Teller effect and the related perturbations of the magnetic properties. The Mössbauer parameters of $[(\text{cyclam-ac})\text{Fe}^{\text{V}}\equiv\text{N}]^+$ ($\delta = -0.02 \text{ mm s}^{-1}$, $\Delta E_Q = 1.60 \text{ mm s}^{-1}$, Table 8.5) are consistent with those found earlier for $[(\text{cyclam})\text{Fe}^{\text{V}}\equiv\text{N}]^+$ in CH_3CN solution which presumably provides a sixth ligand to the iron ($\delta = -0.04 \text{ mm s}^{-1}$, $\Delta E_Q = 1.67 \text{ mm s}^{-1}$) [282].

8.2.3.5 Iron(VI) Compounds

Basic ligand-field considerations predict the following energetic order of valence d -orbitals for six-coordinate iron–nitrido compounds with approximate C_{4v} symmetry: $d_{xy} < d_{xz} \approx d_{yz} < d_{x^2-y^2} < d_{z^2}$, whereby only the d_{xy} orbital is nonbonding

Table 8.5 Mössbauer parameters of iron(V) and iron(VI) compounds^a

Compound	CN ^b	Spin ^c	Temp. (K)	δ (mm s ⁻¹)	ΔE_Q (mm s ⁻¹)	Ref.
Iron(V)						
$\text{La}_2\text{LiFe}^{\text{V}}\text{O}_6$	6	3/2	r.t.	-0.41	0	[277] ^d
$[\text{B}^*\text{Fe}^{\text{V}}(\text{O})]^-$ ^c	5	1/2	4.2	-0.42	4.25	[173]
$[(\text{cyclam-ac})\text{Fe}^{\text{V}}\equiv\text{N}]^+$	6	1/2	4.2	-0.02	1.60	[200, 255]
Iron(VI)						
$[(\text{Me}_3\text{cyclam-acetate})\text{Fe}^{\text{VI}}\equiv\text{N}]^{2+}$	6	0	4.2	-0.29	+1.53	[284]
K_2FeO_4	4	1	78	-0.85	0	[285]
SrFeO_4	4	1	78	-0.83	0	[285]
BaFeO_4	4	1	78	-0.81	0	[285]

^a B^* = a tetraamido macrocycle, cyclam-acetate = 1,4,8,11-tetramethyl-1,4,8,11-tetraaza-cyclo-tetradecene-1-acetate

^bCoordination number

^cSpin of the iron(IV) ion

^dSpectra not published

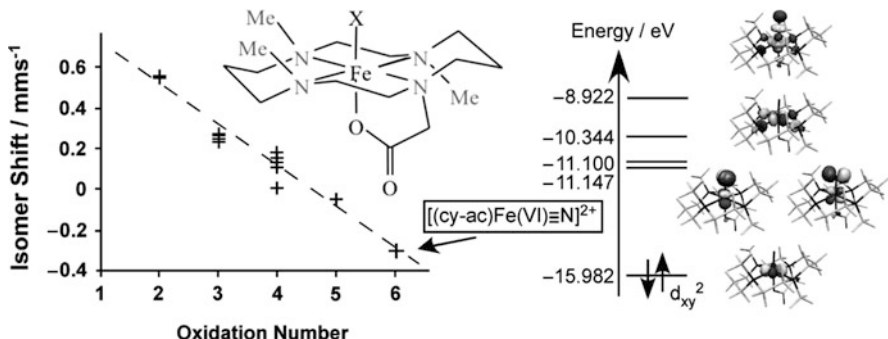


Fig. 8.26 (Left) Isomer-shift correlation diagram for a systematic series of $[(\text{Me}_3\text{cyclam}-\text{acetate})\text{Fe}(\text{X})]^{n+}$ complexes, where X is an azide (N_3^-) or a nitrido ($\equiv\text{N}$) group. (Right) Orbital scheme of $[(\text{Me}_3\text{cyclam}-\text{acetate})\text{Fe}^{\text{VI}}\equiv\text{N}]^{2+}$

with respect to all ligands [257]. This suggests relatively high stability for a d^2 or a d^1 configuration. Accordingly, the first and only known molecular iron(VI) compound is a recently discovered Fe(VI)-nitrido species [284]. The bulky, innocent ligand ($\text{Me}_3\text{cyclam}-\text{acetate}$) $^-$ made it possible to synthesize $[(\text{Me}_3\text{cyclam}-\text{acetate})\text{Fe}^{\text{VI}}\equiv\text{N}]^{2+}$ by low-temperature photolysis of the iron(IV)-azide precursor $[(\text{Me}_3\text{cyclam}-\text{acetate})\text{Fe}^{\text{IV}}\text{N}_3]^{2+}$ in the sample cup of the Mössbauer spectrometer. The product is diamagnetic, $S = 0$, as predicted by the LF diagram, and the $\text{Fe}\equiv\text{N}$ bond (157 pm obtained from EXAFS) is significantly shorter than that for the corresponding iron(V) compound (161 pm, [255]). The isomer shift is -0.29 mm s^{-1} , which is 0.40 mm s^{-1} lower than that of the corresponding iron(III)-azide starting material and 0.19 mm s^{-1} lower than that of the corresponding iron(V)-nitrido compound which was, together with the XAS preedge energies, the key argument for the assignment of the oxidation state (VI), see Fig. 8.26. The general trends in the electronic structure of such iron-nitrido systems as a function of the number of electrons has been elucidated in a recent DFT study of a series of hypothetical and real complexes [286].

The only other and long known iron(VI) species is the tetrahedral ferrate ion, FeO_4^{2-} , occurring in different salts such as K_2FeO_4 , Cs_2FeO_4 , or SrFeO_4 and BaFeO_4 [186]. The salts are rather unstable and represent strong oxidants used in chemistry and technical applications. According to its local tetrahedral symmetry, the iron(VI) is in high spin state, $S = 1$, and the isomer shifts takes unrivaled large negative values ($\delta = -0.80 - 0.85 \text{ mm s}^{-1}$ at 75 K, [287]). A brief review on other basic physical and chemical properties of ferrates are found in [186].

8.2.4 Iron in Low Oxidation States

Low-valent iron in the formal oxidation states (I) and (0) is mostly found in iron-carbonyl and metal–organic compounds which have been intensively studied since

Table 8.6 Isomer shift and quadrupole splitting of iron carbonyls and metal–organic compounds

Compound	Formal valency ^a	Temp. (K)	δ (mm s ⁻¹)	ΔE_Q (mm s ⁻¹)	Ref.
Fe(CO) ₅	0	78	-0.09	2.57	[288]
Fe ₂ (CO) ₉	0	78	0.10	0.54	[288]
Fe ₃ (CO) ₁₂	0	78	0.04 0.10	0.13 (1×), 1.12 (2×)	[288]
Na ₂ ⁺ [Fe(CO) ₄] ²⁻	-II	80	-0.18	0	[17] in Chap. 1
Et ₄ N ⁻ [Fe(CO) ₄ H] ⁺	I	80	-0.17	1.36	[17] in Chap. 1
I ₂ :Fe(CO) ₄	II	4.2	0.14	0.38	[17] in Chap. 1
LFe(CO) ₄ ^b	0	4.2	-0.09 to +0.07	0.4–2	[17] in Chap. 1
Butadiene-Fe(CO) ₃	0	4.2	0.03	1.46	[288], [17] in Chap. 1
(Cp) ₂ Fe ^c	II	80	0.53	2.37	[17] in Chap. 1
(Cp) ₂ FeBr	III		0.43	~0.2	[17] in Chap. 1
Substit. Fe-Cp compounds	II		0.51–0.55	2.0–2.4	[17] in Chap. 1

^aFormal valence state of iron^bL is a two-electron donor ligand^cCp = π -cyclopentadienyl

the early years of Mössbauer spectroscopy [17] in Chap. 1, [288]. We refrain from reviewing this field again, but rather present a cursory table of values to set out the possible impact of Mössbauer spectroscopy for the identification of valence states and structural features (Table 8.6).

Metal–organic bonds are short and covalent; therefore, the assignment of oxidation numbers to the central metal is problematic *per se*. The composition of the relevant molecular orbitals frequently approaches 50% (or more) admixture of ligand character into the metal *d*-orbitals. While a reasonable correlation of the isomer shift with the oxidation state could be found for iron(II) to iron(VI), particularly when the comparison is limited to the same spin state and to similar ligand systems, such trends are mostly elusive for low-valent low-spin iron. The major reason is the strong degree of π -backbonding for low-valent metal ions, which changes upon oxidation of the compound and compensates for the change in the number of valence 3*d* electrons. The classical examples for this behavior are K₄[Fe(CN)₆]·3H₂O and K₃[Fe(CN)₆] which have virtually the same isomer shift [289] and also the same metal–ligand bond lengths. Therefore, simple trends in isomer shifts for low-valent compounds (and particularly, low-spin) should be accepted only with caution.

8.2.4.1 Low-Valent Iron Porphyrins

In some electron-rich systems, the usual trend that the isomer shift increases with the number of valence electrons appears to be inverted. This is the case for the comparison of planar iron porphyrins in the formal oxidation states (I) and (0), which are obtained by one- and two-electron reduction of iron(II) porphyrins in

THF solution [290]. There had been much confusion in the past about the magnetic moment of the iron(I) species and the correct Mössbauer and NMR properties caused by impurities of the samples and possible unknown axial ligation. However, with clean crystallized samples with known molecular structure [291], the first reduction product of iron(II)(tetraphenylporphyrin), $[\text{Fe}(\text{TPP})]^-$, can be clearly characterized as a quasiplanar iron(I) complex with spin $S = 1/2$ (EPR: $g_{\perp} = 2.28$, $g_{\parallel} = 1.92$). The isomer shift is very high for a porphyrin, $\delta = 0.65 \text{ mm s}^{-1}$, and is about 0.13 mm s^{-1} more positive than that for planar Fe(II)(TPP) (Table 8.7), consistent with the high electron density of a low-spin d^7 system.

However, it was pointed out that two other observations are out of line with the iron(I) formulation and more consistent with an iron(II)-porphyrin *radical anion* [290]: (1) the low-intensity red-shifted Soret band in the UV–VIS spectrum with broad maxima in the α, β -region compared to, for instance, Fe(TPP) in THF, is typical of a porphyrin radical, and (2) the bond lengths of the porphyrin core indicate population of the (antibonding) LUMO of the ligand (i.e., the presence of an “extra” electron in the π -system). The presence of porphyrin radical character in the electronic ground state was also inferred from the paramagnetic NMR-shifts of the pyrrole protons at the meso and β -carbon atoms [291].

The second reduction step of Fe(II)(TPP) yields an extremely air-sensitive green product which can be assigned the formula $[\text{Fe}(\text{I})(\text{TPP})]^2-$ because of the red shift of the Soret band in the UV–VIS spectrum. The pure material is diamagnetic ($S = 0$) but this does not allow one to distinguish between the three possible descriptions as an iron(0) d^8 -porphyrin, a spin-coupled $S = 1/2$ iron(I)-porphyrin

Table 8.7 Isomer shift and quadrupole splitting of some low-valent iron complexes

Compound	Val. ^a	Spin	Temp. (K)	δ (mm s ⁻¹)	ΔE_Q (mm s ⁻¹)	Ref.
Fe(II)(TPP)(pip) ₂	II	$S = 0$	77	0.51	1.44	[146]
Fe(II)(TPP)	II	$S = 1$	77	0.52	1.51	[146]
$[\text{Fe}(\text{TPP})]^-$	I	$S = 1/2$	77	0.65	2.23	[290, 291]
$[\text{Fe}(\text{TPP})]^{2-}$	0	$S = 0$	77	0.48	1.29	[290, 291]
LFe(HCCPh)	I	$S = 3/2$	4.2	0.50	2.05 ^b	[292]
LFe ^{II} Cl	II	$S = 2$	4.2	0.74	-1.61	[293]
LFe ^{II} CH ₃	II	$S = 2$	4.2	0.48	+1.74	[293]
L ^{Me} Fe ^{II} NNFe ^{II} L ^{Me}	II	$S_{\text{Fe}} = 2$	4.2	0.62	1.41 ^b	[294]
{[PhBP <i>i</i> Pr ₃]Fe ^I (μ -N ₂) ₂ }	I	$S_{\text{Fe}} = 3/2$	4.2	0.53	0.89	[211]
[PhBP <i>i</i> Pr ₃]Fe ^I PMe ₃	I	$S = 3/2$	4.2	0.57	0.23	[211]
[PhBP <i>i</i> Pr ₃]Fe ^{II} (dbabh) ^c	II	$S = 2$	4.2	0.55	1.75	[211]

^aFormal valence state of the iron

^bThe value is derived from a zero-field spectrum recorded at 150 K. ΔE_Q could not be determined at 4.2 K because the compound is in the limit of slow paramagnetic relaxation and the strong unquenched orbital moment forces the internal field into the direction of an “easy axis of magnetization.” As a consequence, the quadrupole shift observed in the magnetically split spectra results only from the component of the *EFG* along the internal field and the orientation of the *EFG* is not readily known

^cdbabh is a bulky N-coordinating amide

anion radical ($S' = 1/2$), or an iron(II) ($S = 1$) site coupled to a porphyrin dianionic radical. The Fe–N bond distances (196.8 pm), which are consistent with an LS state, support the suggestion of an iron(I)-radical formulation but do not readily rule out an iron(II)-diradical moiety.

The Mössbauer spectrum of the dianion was a surprise because the isomer shift ($\delta = 0.48 \text{ mm s}^{-1}$) was substantially *more negative* than that of the monoanion, and resembles more that of Fe(II)(TPP) than that of $[\text{Fe}(\text{I})\text{TPP}]^-$. Reed and Scheidt therefore suggested a resonance hybrid of iron(I) and iron(II) for the electronic structure of the dianion molecule instead of the formulation $[\text{Fe}(\text{O})(\text{TPP})]^{2-}$ [290, 291].

8.2.4.2 Three- and Four-Coordinate Low-Valent Iron Compounds

A quest for low-valent iron(I)-coordination compounds started in the early 2000s after it was demonstrated that the so-called Chatt-type nitrogen reduction cycle [295] can be mediated by a mononuclear molybdenum compound with low coordination number ([296] and references therein). Although the Chatt-cycle has been originally proposed for the Mo cofactor of the biological nitrogen fixation system, metal ions other than Mo were thought to play a role in binding nitrogen in nitrogenase and iron was certainly an interesting possibility. The nitrogenase enzyme system [297–299] needs to be loaded with electrons before substrate binding, and the Chatt-cycle for an iron analog implicates iron-oxidation states from (I) to (IV). The feasibility of a corresponding synthetic model compound is under intense exploration. Within this field of research, a number of low-coordinated iron(I) compounds have been crystallographically characterized but only a few Mössbauer spectra have been recorded.

The first Mössbauer spectra of an iron(I) compound were reported for LFe(HCCPh), $\text{L} = [\text{HC}(\text{'Bu})\text{N}-[2,6\text{-diisopropylphenyl}]\text{)}_2]^-$ [292]. The iron is coordinated to the two nitrogen atoms of the β -diketiminate ligand L and to the $\text{C}\equiv\text{C}$ bond of the phenylacetylene ligand via one of the π orbitals which renders the compound essentially three-coordinate. Various spectroscopic measurements, including EPR and applied-field Mössbauer spectroscopy, in conjunction with DFT calculations, showed clearly that the electronic structure of LFe(HCCPh) is best described by a $3d^7$ high-spin configuration with spin $S = 3/2$ (Table 8.7). Within the LF picture for the three-coordinate compound, the spin-orbit interaction in the space of the energetically quasi degenerate orbitals d_{z^2} and d_{yz} yields a consistent explanation for the remarkable magnetic properties, that is, the uniaxial hyperfine field of 68.8 T at the Mössbauer nucleus, the huge ZFS, $D \approx -100 \text{ cm}^{-1}$, and the highly anisotropic effective g values of about nine and zero. For one direction, the orbital momentum of iron is almost unquenched. The electronic properties of LFe(HCCPh) can be compared with those of the related iron(II) compounds LFe^{II}Cl and LFe^{II}CH₃ [293]. Note that the isomer shifts of the divalent iron compounds are more positive than those of the monovalent iron.

An interesting reaction product of the β -diketiminate iron complex is the N₂-bridged diiron complex L^{Me}FeNNFeL^{Me} [294] which also contains a three-coordinate iron site with the formal oxidation number (I). The ground state with spin $S_t = 3$ exhibits a large orbital contribution to the magnetic moment and a uniaxial positive hyperfine field of +68.1 T. A comprehensive study [294], however, led to the conclusion that the compound is best described as an iron(II) dimer ($S_{\text{Fe}} = 2$) with a bridging N₂²⁻ group which, in analogy with the isoelectronic O₂ molecule, is in a spin-triplet state ($S_{\text{N}2} = 1$). With this interpretation, the total spin state $S_t = 3$ can be readily explained by antiferromagnetic coupling of the spin $S_{\text{N}2} = 1$ and the spins $S_{\text{Fe},1} = 2$ and $S_{\text{Fe},2} = 2$ of the two terminal iron(II) sites without invoking an exotic ferromagnetic coupling scheme between two high-spin iron(I) sites.

Weak ferromagnetic coupling ($J \approx 4 \text{ cm}^{-1}$) has been found for the related dinitrogen complex $\{[\text{PhBP}^{\text{iPr}}_3]\text{Fe}^{\text{I}}\}_2(\mu\text{-N}_2)$ which appears to be more likely an iron(I) complex [211]. Both iron sites are four-coordinate by three phosphorous atoms from the ligand [PhBP^{iPr}₃] [300] and one nitrogen atom from the bridging N₂. The Mössbauer parameters are summarized in Table 8.7, together with those of the monomeric monovalent “reference” complex [PhBP^{iPr}₃] $\text{Fe}^{\text{I}}\text{PMe}_3$.

8.2.4.3 Low-Spin Iron in the Active Site of Hydrogenases

Low-valent iron is an essential constituent of the active center of hydrogenases, the biological catalysts for the production of molecular hydrogen. Huge amounts of H₂ are produced in the anoxic biological habitats of the planet by microbial fermentation. Anaerobic microorganisms use most of it to reduce CO₂ to methane or sulfate to hydrogen sulfide [301]. These reactions and the sheer numbers of turnover have mesmerized scientists for a long time and have stimulated very active research in biology and bioinorganic chemistry. The literature in this rapidly developing field has been reviewed in many major articles ([301–304] and references therein). Here, we summarize the essential Mössbauer parameters of the different types of active clusters and their model compounds that have been synthesized to explore either the structural and spectroscopic or the functional features of the natural systems. Three types of hydrogenases are known, and these are labeled according to the composition of their active sites, [FeFe]-, [FeNi]-, and [Fe]-hydrogenases.

[FeFe]-Hydrogenases

The [FeFe]-hydrogenases have been known since the 1930s [305], and Warburg recognized sulfur-coordinate iron as an essential element of the enzyme [306]. The [FeFe]-hydrogenase from *Clostridium pasteurianum* accommodates 20 iron atoms organized in one [2Fe–2S] cluster, three [4Fe–4S] clusters and the so-called H-cluster which is a [4Fe–4S] cluster covalently linked to a dinuclear [FeFe]

compound [307]. The iron atoms in the dinuclear center are bridged by CO and two sulfur atoms from a dithiol group. Only one of the two iron atoms is additionally bridged by a single cysteine sulfur to the attached [4Fe–4S] cluster, forming together the H-cluster. The other terminal ligands of the [FeFe] dimer are cyanide and CO [308] originally discovered in the vibration spectra of the protein [309].

Elaborate Mössbauer studies on enzyme samples obtained from two different microorganisms (which was impeded not only by the large number of iron sites but also by a large number of possible redox states and sample treatments) provided the electronic structure of the cyanide- and CO-ligated [FeFe] center and its interaction with the attached iron–sulfur cluster [310, 311]. The Mössbauer spectrum of the dinuclear center was recognized for the first time in a sample with reduced H clusters (H_{red}) showing a quadrupole doublet indicating low-spin iron (II) ($\delta = 0.08 \text{ mm s}^{-1}$, $\Delta E_Q = 0.87 \text{ mm s}^{-1}$) [310]. Later, different states of the [FeFe] center could be identified from the spectra of hydrogenase from a different organism, in three oxidized, one reduced, and a CO-treated state [311]. The iron sites are persistently low-spin and respond to redox titration only with minor shifts of δ and ΔE_Q , but they take part in the paramagnetic behavior of the H-cluster and show appreciable hyperfine coupling at redox potentials of -110 to -350 mV (SHE) and in the CO-reacted sample [311]. Isomer shifts and quadrupole splittings of the [FeFe] center are listed in Table 8.8, together with those of some model compounds.

[NiFe]-Hydrogenases

[NiFe]-hydrogenases are intensely studied enzymes [303, 304]. The first evidence of CO and CN^- groups as integral parts of the active center of a biological system was obtained from infrared spectroscopy for this class of hydrogenases [312]. Later, the first X-ray structure [313] revealed that these diatomic groups are coordinated to the iron atom of the [NiFe] center. Early Mössbauer investigations had revealed a spectral component with an unusually low isomer shift, $\delta = 0.05\text{--}0.15 \text{ mm s}^{-1}$ [314] which only later, in conjunction with the first model compound having a P– S_3 –CO–CN coordination environment [315], has been safely assigned to the corresponding low-spin iron(II) center; the data are given in Table 8.8. Further conclusive Mössbauer work on the [NiFe] center is elusive, mostly because of the difficulties to identify and subtract the dominating and overlapping subspectra from FeS clusters and the tantalizing “plethora of so-called ‘states’ of the enzyme” [304] (at least 11!), some of which might be just artifacts of protein isolation and processing.

[Fe]-Hydrogenase

The third type of hydrogenases from some methanogenic archaea, also referred to as iron–sulfur-cluster-free hydrogenase, or *Hmd*, has attracted interest in bioinorganic

Table 8.8 Isomer shift and quadrupole splitting of low-spin iron in the active site of hydrogenases and biomimetic model compounds

Compound	Temp. (K)	δ (mm s ⁻¹)	ΔE_Q (mm s ⁻¹)	Ref.
[FeFe]-hydrogenase and models				
H _{Red} , <i>Clostridium pasteurianum</i>	4.2	0.08	0.87	[310]
H _{Red} , <i>Desulfovibrio vulgaris</i>	4.2	0.13	0.85	[311]
H _{OX+1} ^a	4.2	0.16	1.09	[311]
H _{OX-2.06} ^a	4.2	0.17	1.08	[311]
H _{OX-2.10} ^a	4.2	0.13, 0.14	0.85, 0.67	[311]
H _{OX} -CO ^a	4.2	0.17, 0.13	0.70, 0.65	[311]
[Fe ^{II} (PS ₃)(CO)(CN)]	4.2	0.15	0.91	[315]
{[Fe ₂ S ₃ L](CN)(CO) ₄ } ^b	80	0.05, 0.11	0.92, 0.44	[316]
{[Fe ₂ S ₃ L](CO) ₅ } ^c	80	0.03, 0.12	0.94, 0.25	[316]
[NiFe]-hydrogenase and models				
State D, <i>Chromatium vinosum</i>	4.2	0.05–0.15	–	[314]
[Ni(dsdm)(Fe ⁰ (CO) ₃) ₂ } ^e	80	0.07, 0.03	0.66, 0.57	[317]
[Fe ⁰ (CO) ₃ SMe] ₂	80	0.03	1.00/0.88 ^d	[317]
[Fe]-hydrogenase and models				
[Fe], native	80	0.06	+0.65	[318]
[Fe], cofactor	80	0.03	0.43	[318]
[Fe] + H ₂	80	0.06	0.65	[318]
[Fe] + CO	80	−0.03	−1.38	[318]
[Fe] + KCN	80	−0.001	−1.73	[318]
[Fe(<i>cis</i> -CO) ₂ (N-R) ₂]	80	0.10	0.79	[319]
[Fe(<i>cis</i> -CO) ₂ (S-R) ₂]	80	0.07	0.51	[320]
Fe(CO) ₂ (PPh ₃)IL	50	0.10	0.48	[321]

^aH clusters are termed according to one-electron oxidation and the highest EPR g value, or CO treatment, see [311]

^bCompound 5a

^cCompound 4a of [316]

^dSyn and anti-configuration, respectively

^eMore examples of compounds of the type [X(Fe(CO)₃)₂] are found in [317]

chemistry because it does not contain additional obscuring nickel or iron–sulfur clusters in its active site [301]. The abbreviation Hmd is related to the catalyzed reaction, namely, the reversible reduction of methenyltetrahydromethanopterin with H₂ to methylenetetrahydromethanopterin and a proton [322]. The mononuclear [Fe]-center has a square-pyramidal coordination polyhedron provided by the N-atom of an unusual guanyllyl-pyridone cofactor in the apical position and a cysteine-sulfur atom, two CO molecules and an unknown ligand in the basal plane [323, 324]. The presence and geometric arrangement of the CO groups was discovered first by infrared spectroscopy which also revealed the reaction of the center with CO and the reversible formation of a presumably six-coordinate derivative with three CO ligands and alternatively, the bonding of three CN[−] ligands [325]. These free forms, as well as a H₂-bound form and the quasiisolated iron center in a protein-free environment with only the cofactor and sulfur substituents, could be distinguished by Mössbauer spectroscopy (Table 8.8). The [Fe]

center is clearly low-spin as can be inferred from the low isomer shifts, $\delta < 0.1 \text{ mm s}^{-1}$, and it is diamagnetic as seen from the lack of EPR signals and from applied-field Mössbauer spectra [318]. As the total charge of the iron center is not known, the oxidation state could not be derived from the Mössbauer spectra since two oxidation states, Fe(II) and Fe(0), both show $S = 0$, and the isomer shifts are not conclusive; only Fe(I) is ruled out because it is paramagnetic. However, an inspection of the IR frequencies for a large number of complexes with a {Fe(*cis*-CO)₂} motif strongly supports an Fe(II) LS state [319].

8.3 Mobile Mössbauer Spectroscopy with MIMOS in Space and on Earth

Göstar Klingelhöfer^{*} and Iris Fleischer^{*}

8.3.1 Introduction

The NASA Mars Exploration Rovers (MER) (Fig. 8.27), Spirit and Opportunity, landed on the Red Planet in January 2004. The goal of the mission was to search for signatures of water possibly being present in the past. Both NASA Mars Exploration Rovers [326] carry the miniaturized Mössbauer spectrometer (MIMOS II) [327] as part of their scientific payload. The scientific basis for landing a Mössbauer spectrometer on Mars is extensively discussed by Knudsen et al. [328, 329]. The scientific objectives of the MIMOS II Mössbauer spectrometer investigation on Mars are (1) to identify its mineralogical composition and (2) to measure the relative abundance of iron-bearing phases (e.g., silicates, oxides, carbonates, phyllosilicates, hydroxyoxides, phosphates, sulfides, and sulfates), (3) to distinguish between magnetically ordered and paramagnetic phases and provide, from measurements at different temperatures, information on the size distribution of magnetic particles, and (4) to measure the distribution of Fe among its oxidation states (e.g., Fe²⁺, Fe³⁺, and Fe⁶⁺). These data characterize the present state of Martian surface materials and provide constraints on climate history and weathering processes by which the surface evolved to its present state.

The MER mission was originally planned to last for three months on the Martian surface. At the time of writing (July 2010), both rovers and their instruments have spent more than 6 years exploring their landing sites and are still operational.

^{*}Institut für Anorganische Chemie und Analytische Chemie, Johannes Gutenberg-Universität Mainz, Staudingerweg 9, 55099 Mainz, Germany; e-mail: klingel@uni-mainz.de.



Fig. 8.27 NASA Mars-Exploration-Rover artist view (courtesy NASA, JPL, Cornell). On the front side of the Rover, the robotic arm (IDD) carrying the Mössbauer spectrometer and other instruments can be seen

The mission success criteria for the rovers had been to drive more than 600 m, and the goal for the Mössbauer spectrometers had been to collect spectra from at least three different soil and rock samples at each landing site. To date, the rovers have covered distances of more than 7 km (Spirit) and more than 20 km (Opportunity), respectively. The total amount of scientific targets investigated by the Mössbauer spectrometers exceeds 300, the total number of integrations exceeds 600. A total of 14 unique Fe-bearing phases were identified up to now: Fe^{2+} in olivine, pyroxene, and ilmenite; Fe^{2+} and Fe^{3+} in magnetite and chromite; Fe^{3+} in nanophase ferric oxide (npOx), hematite, goethite, jarosite, an unassigned Fe^{3+} sulfate, and an unassigned Fe^{3+} phase associated with jarosite. Fe^0 was identified in kamacite, an Fe–Ni alloy, and schreibersite $(\text{Fe},\text{Ni})_3\text{P}$ present in Fe-meteorites. Both Mössbauer spectrometers remain operational and continue to return valuable scientific data [330–335].

Besides the extraterrestrial application of MIMOS, there are a number of terrestrial applications, such as the investigation of rock paintings, ancient artifacts, and environmental science, where the instrument has been applied successfully.

8.3.2 *The Instrument MIMOS II*

The instrument MIMOS II is extremely miniaturized compared to standard laboratory Mössbauer spectrometers and is optimized for low power consumption and high detection efficiency (see Sect. 3.3) and [326, 327, 336–339]. All components were selected to withstand high acceleration forces and shocks, temperature variations over the Martian diurnal cycle, and cosmic ray irradiation. Mössbauer measurements can be done during day and night covering the whole diurnal temperature

variation between about -100°C (min) and about $+10^{\circ}\text{C}$ (max) of a Martian day [340–343].

To minimize experiment time a very strong $^{57}\text{Co}/\text{Rh}$ source was used, with an initial source strength of about 350 mCi at launch. Instrument internal calibration is accomplished by a second, less intense radioactive source mounted on the end of the velocity transducer opposite to the main source and in transmission measurement geometry with a reference sample. For further details, see the technical description in Sect. 3.3.

The MIMOS II Mössbauer spectrometer sensor head (see Sect. 3.3) is located at the end of the *Instrument Deployment Device IDD* (see Fig. 8.27) On Mars-Express Beagle-2, an European Space Agency (ESA) mission in 2003, the sensor head was also mounted on a robotic arm integrated to the *Position Adjustable Workbench (PAW)* instrument assembly [344, 345]. The sensor head shown in Figs. 8.28 and 8.29 carries the electromechanical transducer with the main and reference $^{57}\text{Co}/\text{Rh}$ sources and detectors, a contact plate, and sensor. The contact plate and sensor are used in conjunction with the IDD to apply a small preload when it places the sensor head, holding it firmly against the target.

Because of the complexity of sample preparation, backscatter measurement geometry is the choice for an in situ planetary Mössbauer instrument [327]. No sample preparation is required, because the instrument is simply presented to the sample for analysis. Both 14.41 keV γ -rays and 6.4 keV Fe X-rays are detected simultaneously.

MIMOS II has three temperature sensors, one on the electronics board and two on the sensor head. One temperature sensor in the sensor head is mounted near the internal reference absorber, and the measured temperature is associated with the reference absorber and the internal volume of the sensor head. The other sensor is mounted outside the sensor head at the contact ring assembly. It gives the analysis temperature for the sample on the Martian surface. This temperature is used to route

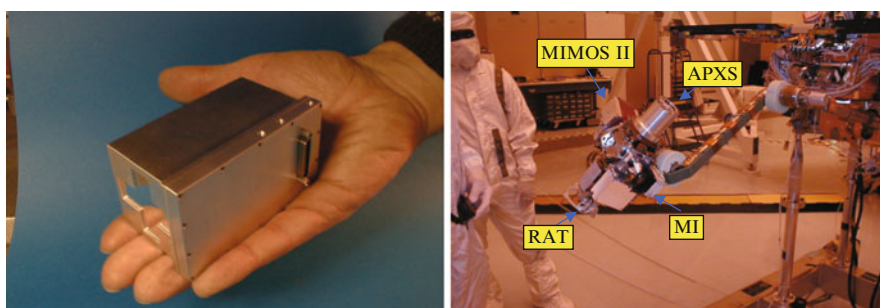


Fig. 8.28 External view of the MIMOS II sensor head without contact plate assembly (*left*); MIMOS II sensor head mounted on the robotic arm (IDD) of the Mars Exploration Rover. The IDD also carries the α -Particle-X-ray Spectrometer APXS, also from Mainz, Germany, for elemental analysis, the Microscope Imager MI for high resolution microscopic pictures ($\sim 30 \mu\text{m}$ per pixel), and the RAT for sample preparation (brushing; grinding; drilling ($< 1 \text{ cm}$ depth)). Picture taken at Kennedy-Space-Center KSC, Florida, USA

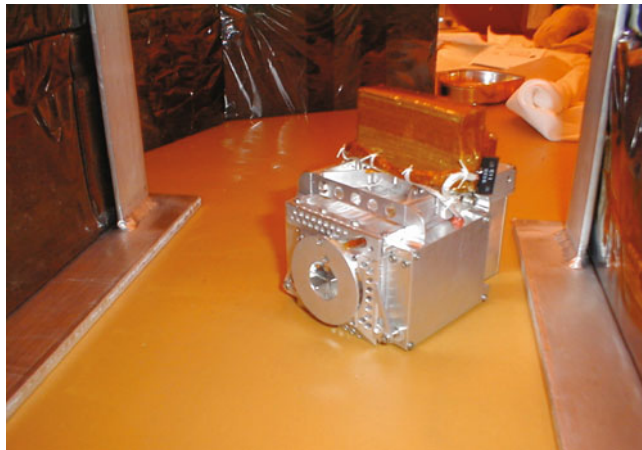


Fig. 8.29 The flight unit of the MIMOS II Mössbauer spectrometer sensor head (for the rover *Opportunity*), with the circular contact plate assembly (*front* side). The circular opening in the contact plate has a diameter of 15 mm, defining the field of view of the instrument

the Mössbauer data to the different temperature intervals (maximum of 13, with the temperature width software selectable) assigned in memory areas (for more details, see Sect. 8.3.3).

Sampling depth. In addition to no requirement for sample preparation, backscatter measurement geometry has another important advantage. Emission of internal conversion electrons, Auger electrons, and X-rays, which occur along with the recoilless emission and absorption of the 14.4 keV γ -ray of ^{57}Fe , can also be used for Mössbauer measurements. For ^{57}Fe , X-rays resulting from internal conversion have an energy of 6.4 keV. Because the penetration depth of radiation is inversely proportional to energy, the average depth from which 14.4 keV γ -rays emerge in emission measurements is greater than that for 6.4 keV X-rays. The importance of this difference in emission depths for an in situ Mössbauer spectrometer is that mineralogical variations that occur over the scale depths of the 14.4 and 6.4 keV radiations can be detected and characterized. Such a situation on Mars might arise for thin alteration rinds and dust coatings on the surfaces of otherwise unaltered rocks [346, 347].

Cosine smearing. Because instrument volume and experiment time must both be minimized for a planetary Mössbauer spectrometer, it is desirable in backscatter geometry to illuminate as much of the sample as possible with source radiation. However, this requirement at some point compromises the quality of the Mössbauer spectrum because of an effect known as “cosine smearing” [327, 348, 349] (see also Sects. 3.1.8 and 3.3). The effect on the Mössbauer spectrum is to increase the linewidth of Mössbauer peaks (which lowers the resolution) and shift their centers outward (affects the values of Mössbauer parameters). Therefore, the diameter of the source “ γ -ray beam” incident on the sample, which is determined by a

collimator, is a compromise between acceptable experiment time and acceptable velocity resolution. The distortion in peak shape resulting from cosine smearing can be accounted for mathematically in spectral fitting routines [327, 339, 348–350].

8.3.3 Examples

8.3.3.1 Mars-Exploration-Rover Mission

A MIMOS II instrument was mounted on the robotic arm of each of two identical rovers, called *Spirit* and *Opportunity*, which were launched separately in June 2003 (from Kennedy Space Center, Florida) and landed successfully on Mars in January 2004, *Spirit* in Gusev Crater and *Opportunity* in Meridiani Planum (opposite side of Mars). The primary objective of the Mars-Exploration-Rover (MER) science investigation is to explore with the *Athena* instrument payload two sites on the Martian surface where water may once have been present, and to assess past environmental conditions at those sites and their suitability for life [326, 327, 351, 352]. The rovers are ~ 1.5 m long, ~ 1.5 m high, and weigh ca. 185 kg each. The solar panels and a lithium-ion battery system provide a power of up to 900 W-h per Martian day. The rovers have been designed to cover a total distance during the mission of up to about 1 km taking photographs, performing remote sensing with their optical instruments, and recording Mössbauer and X-ray fluorescence (XRF) spectra of rock and soil on their way. Typical measuring times for Mössbauer spectra have been 2–4 h at mission beginning, with a source intensity of ~ 150 mCi at landing. Temperatures change between day and night from as high as about $+10^\circ\text{C}$ to as low as about -100°C , depending on the landing site and the Martian season. The robotic arm (see Fig. 8.30) carries the Mössbauer spectrometer MIMOS II, an α -Particle-X-ray-Spectrometer (APXS) for elemental analysis, developed at the Max Planck-Institute for Chemistry in Mainz and the University Mainz [353, 354], a Microscopic Imager MI, and a Rock Abrasion Tool RAT for polishing rocks and drilling holes of up to ~ 10 mm into rocks, with a diameter of 4.5 cm (see e.g., Fig. 8.31).

Gusev Crater. The Gusev Crater landing site, a flat-floored crater with a diameter of 160 km and of Noachian age, is located at about 14.5°S of the equator. Gusev was hypothesized to be the site of a former lake, filled by Ma'adim Vallis, one of the largest valley networks on Mars. The first Mössbauer spectrum ever recorded on the Martian surface was obtained on soil at Spirit's landing site on the plains in Gusev crater (see Fig. 8.32). It shows a basaltic signature dominated by the minerals olivine and pyroxene. This type of soil and dust were found to be globally distributed on Mars. Spectra obtained on soil at Opportunity's landing site in Meridiani Planum are almost identical to those recorded in Gusev crater.

The collection of spectra obtained at Spirit's landing site reveals various mineralogical signs of weathering. Spectra obtained on the basaltic rocks and soil on the plains show mainly olivine and pyroxene and small amounts of nonstoichiometric magnetite, and only comparably small amounts of weathering. An example

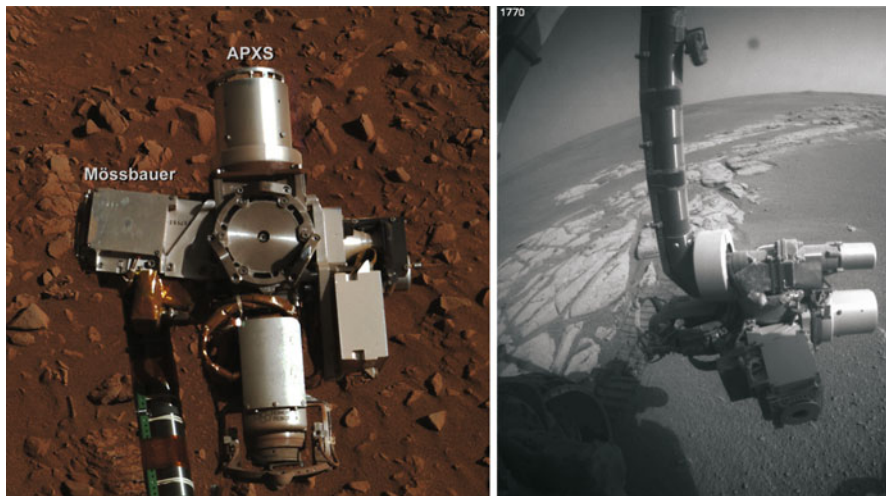


Fig. 8.30 The Instrument Deployment Device (IDD) above the surface of Mars, showing all the four in situ instruments: (left) the MIMOS II with its contact ring can be seen in the front; picture taken at Meridiani Planum, Mars; (right) MIMOS II is located on the left side; picture taken at Gusev Crater, Mars

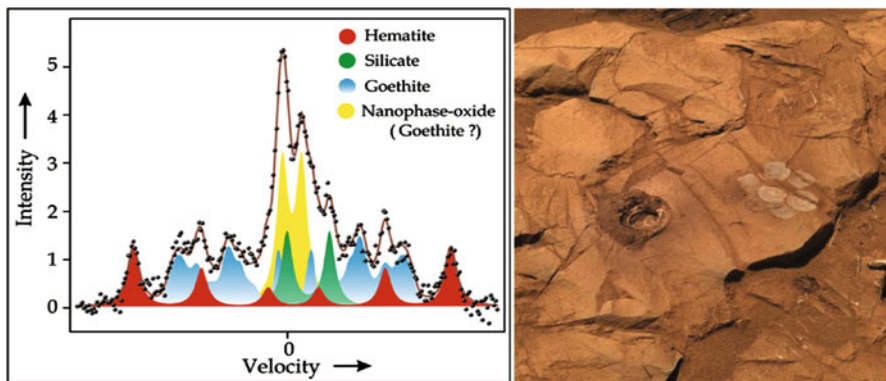


Fig. 8.31 (Left) In the Mössbauer spectrum taken in the Columbia Hills at a rock called *Clovis* the mineral goethite (GT) (α -FeOOH) could be identified. GT is a clear mineralogical evidence for aqueous processes on Mars. (Right) The rock *Clovis* is made out of rather soft material as indicated by the electric drill-current when drilling the ~ 1 cm deep hole seen in the picture. Drill fines are of brownish color. The pattern to the right of the drill hole was made by brushing the dust off the surface by using the RAT

of such a rock named *Adirondack*, found close to Spirit's landing site, is shown in Fig. 8.33, together with its Mössbauer spectrum. The Fe mineralogy of this ~ 50 cm wide rock is composed of the dominating mineral olivine, pyroxene, nanophase

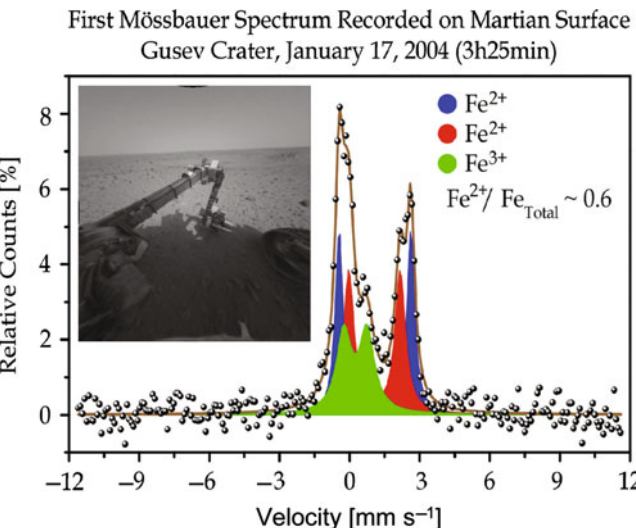


Fig. 8.32 The first Mössbauer Spectrum ever taken outside Earth, at Gusev Crater, Mars. It shows the basaltic composition of the plains at the landing site of the Rover *Spirit*

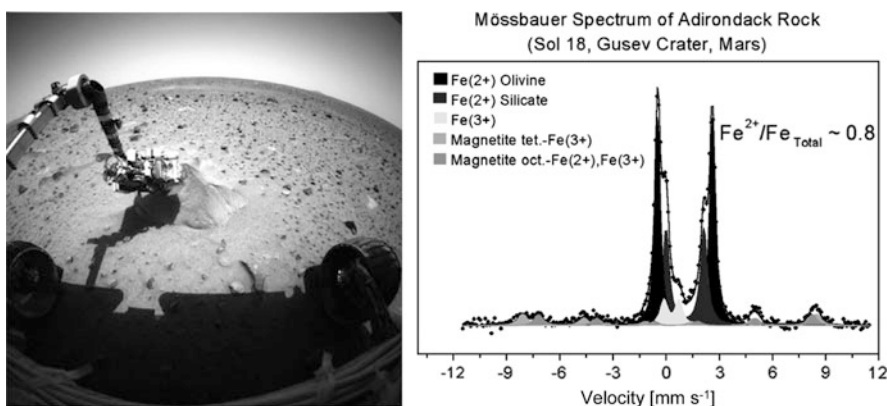


Fig. 8.33 Left: robotic arm with MIMOS II positioned on the rock *Adirondack*, as seen by the navigation camera of the rover; Right: Mössbauer Spectrum (14.4 keV; temperature range 220–280 K) of the rock *Adirondack* at Spirit landing side Gusev Crater, plains. The data were taken at the as-is dusty surface (not yet brushed). The spectrum shows an olivine-basalt composition, typical for soil and rocks in Gusev plains, consisting of the minerals olivine, pyroxene, an Fe³⁺ doublet, and nonstoichiometric magnetite

ferric oxide (npOx), and a small contribution of nonstoichiometric magnetite. The composition does not change within a depth of ~8 mm (drill hole obtained with the Rock Abrasion Tool (RAT)). On a similar rock, also in the plains, named *Mazatzal*, a dark surface layer was detected with the Microscopic Imager after the first of two

RAT grinding operations. This surface layer was removed except for a remnant in a second grind. Spectra – both 14.4 keV and 6.4 keV – were obtained on the undisturbed surface, on the brushed surface and after grinding. The sequence of spectra shows that nanophas Oxide (npOx) is enriched in the surface layer, while olivine is depleted. This is also apparent from a comparison of 14.4 keV spectra and 6.4 keV spectra [332, 346, 347]. The thickness of this surface layer was determined by Monte-Carlo (MC)-Simulation to about 10 μm . Our Monte Carlo simulation program [346, 347] takes into account all kinds of absorption processes in the sample as well as secondary effects of radiation scattering. For the MC-simulation, a simple model of the mineralogical sample composition was used, based on normative calculations by McSween [355].

The spectra of the rocks in the plains are very similar to the spectra obtained on the soil (see above). The ubiquitous presence of olivine in soil suggests that physical rather than chemical weathering processes currently dominate at Gusev crater.

On the contrary, thoroughly weathered rocks were encountered in the Columbia Hills, about 2.5 km away from the Spirit landing site. The Mössbauer signature is characteristic of highly altered rocks. Spectra obtained on these samples show larger amounts of nanophas ferric oxides and hematite. In spectra obtained on ~ 20 rock samples, the mineral goethite ($\alpha\text{-FeOOH}$) was identified (see Fig. 8.31), a clear indicator for aqueous weathering processes in the Columbia hills in the past [332, 356–358]. In particular, one of the rocks, named Clovis (Fig. 8.31), which was found in the West Spur region, contains the highest amount of the Fe oxyhydroxide goethite (GT) of about 40% in area (see Fig. 8.31) found so far in the Columbia Hills. A detailed analysis of these data indicates a particle size of ~ 10 nm. The rock Clovis also contains a significant amount of hematite. The behavior of hematite is complex because the temperature of the Morin transition (~ 260 K) lies within diurnal temperature variations on Mars.

Meridiani Planum. Opportunity touched down on 24 January 2004 in the eastern portion of the Meridiani Planum landing ellipse in an impact crater 20 m in diameter named Eagle Crater. The Meridiani Planum landing site is the top stratum of a layered sequence about 600 m thick that overlies the Noachian cratered terrain. Orbital data indicated the presence of significant amounts of the mineral hematite, an indicator for water activities. The surface of Meridiani Planum explored by the Opportunity rover can be described as a flat plain of sulfur-rich outcrop that is mostly covered by thin superficial deposits of aeolian basaltic sand and dust, and lag deposits of hard Fe-rich spherules (and fragments thereof) that weathered from the outcrop and small unidentified rock fragments and cobbles, and meteorites. Surface expressions of the outcrop occur at impact craters (e.g., Eagle (Figs. 8.34 and 8.35), Fram, Endurance, Erebus, Victoria (see Fig. 8.36) craters) and occasionally in troughs between ripple crests [330, 334, 335, 358].

Mössbauer spectra measured by the Opportunity rover at the Meridiani Planum landing site (see Fig. 8.35) revealed four mineralogical components in Meridiani Planum at Eagle crater: jarosite- and hematite-rich outcrop (see Fig. 8.34), hematite-rich soil, olivine-bearing basaltic soil, and a variety of rock fragments such as

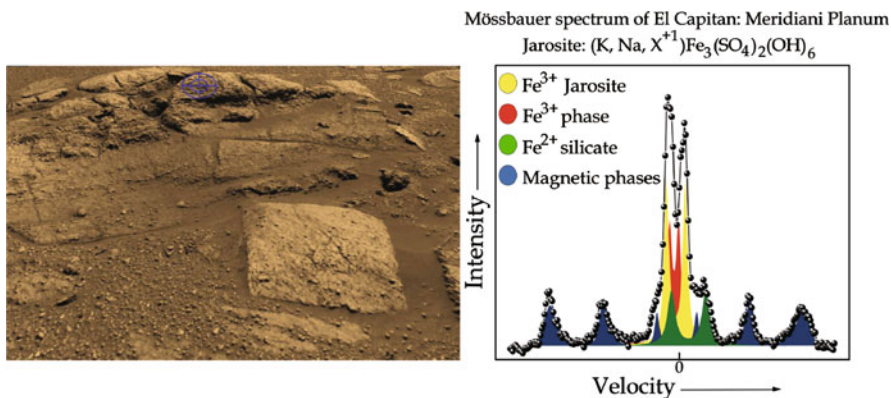


Fig. 8.34 (Left): outcrop rocks found at the crater wall of Eagle Crater, where the rover Opportunity landed on 24 January 2004. Clearly, the sedimentary structure is seen. (Right): in the spectrum, taken on sol 33 (sol = Martian day) of the mission, the mineral Jarosite, an Fe^{3+} -sulfate, could be identified at the Meridiani Planum landing site. It forms only under aqueous conditions at low pH ($<\sim 3\text{--}4$) and is therefore clear mineralogical evidence for aqueous processes on Mars

meteorites and impact breccias. Spherules (Fig. 8.37), interpreted to be concretions, are hematite-rich and dispersed throughout the outcrop.

The same Fe-sulfate jarosite containing material was found everywhere along the several (more than 20) kilometer-long driveway of Opportunity to the south, in particular, at craters Eagle, Fram, Endurance, and Victoria, suggesting that the whole area is covered with this sedimentary jarositic, hematite and Fe-silicate (olivine; pyroxene) containing material. The mineral jarosite ($(\text{K}, \text{Na})\text{Fe}_3(\text{SO}_4)_2(\text{OH})_6$) contains hydroxyl and is thus direct mineralogical evidence for aqueous, acid-sulfate alteration processes on early Mars. Because jarosite is a hydroxide sulfate mineral, its presence at Meridiani Planum is mineralogical evidence for aqueous processes on Mars, probably under acid-sulfate conditions as it forms only at pH-values below $\sim 3\text{--}4$.

Hematite in the soil is concentrated in spherules and their fragments, which are abundant on nearly all soil surfaces. Several trenches excavated using the rover wheels showed that the subsurface is dominated by basaltic sand, with a much lower abundance of spherules than at the surface. Olivine-bearing basaltic soil is present throughout the region. At several locations along the rover's traverse, sulfate-rich bedrock outcrops are covered by no more than a meter or so of soil.

Meteorites on Mars. Meridiani Planum is the first Iron meteorite discovered on the surface of another planet, at the landing site of the Mars Exploration rover Opportunity [359]. Its maximum dimension is ~ 30 cm (Fig. 8.38). Meteorites on the surface of solar system bodies can provide natural experiments for monitoring weathering processes. On Mars, aqueous alteration processes and physical alteration by Aeolian abrasion, for example, may have shaped the surface of the meteorite, which therefore has been investigated intensively by the MER instruments. Observations at mid-infrared wavelengths with the Mini-TES

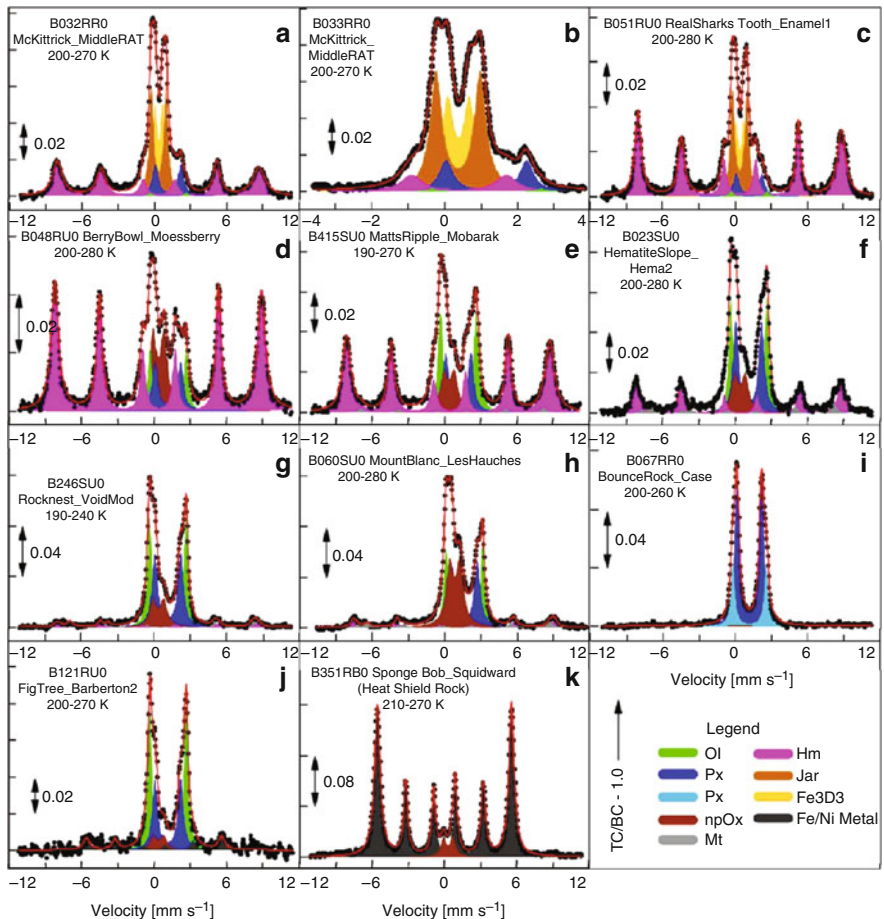


Fig. 8.35 Overview on Meridiani Planum Mössbauer mineralogy. The large variability in mineral composition at this landing site can be seen. Shown are representative Mössbauer spectra. Spectra are the sum over all temperature windows within the indicated temperature ranges. The computed fit and component subspectra (Lorentzian lineshapes) from least-squares analyses are shown by the solid line and the solid shapes, respectively. Full (**a**) and reduced (**b**) velocity Mössbauer spectra for interior Burns outcrop exposed by RAT grinding show that hematite, jarosite, and Fe3D3 (acronym for unidentified Fe^{3+} phase; see [331–334, 341, 346, 352]) are the major Fe-bearing phases. Mössbauer spectrum for a rind or crust (**c**) of outcrop material that has an increased contribution of hematite relative to jarosite plus Fe3D3. Mössbauer spectra of two soils (**d** and **e**) have high concentrations of hematite. The spectrum (**e**) is typical for hematite lag deposits at ripple crests. The soil spectra (**f**–**h**) [334, 341] are basaltic in nature and have olivine, pyroxene, and nanophase ferric oxide as major Fe-bearing phases. The soil target named *MountBlanc_LesHauches* (**h**) is considered to be enriched in martian dust. Mössbauer spectra in (**i**–**k**) are for three single-occurrence rocks: BounceRock (**i**) is monomineralic pyroxene. Barberton (**j**) contains kamacite (iron–nickel metal), and Heat Shield Rock is nearly monomineralic kamacite identified as an Fe–Ni meteorite (see below). TC = total counts and BC = baseline counts (From Morris et al. [334])

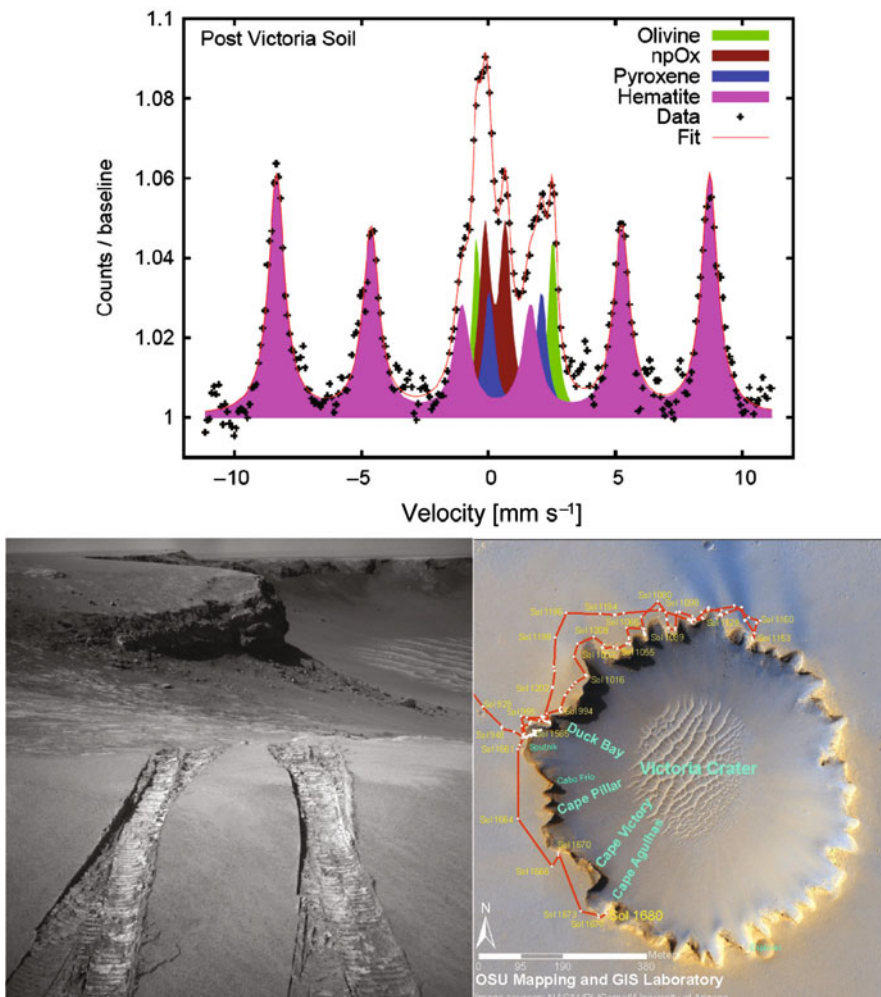


Fig. 8.36 *Left:* Spectrum of the soil close to the crater rim where *Opportunity* entered and exited the crater. The basaltic soil is unusually high in hematite (but no indication of significant contribution from hematitic spherules). *Middle:* rover tracks. *Right:* ~750 m diameter (~75 m deep) eroded impact crater *Victoria Crater*, formed in sulfate-rich sedimentary rocks. Image acquired by the Mars Reconnaissance Orbiter High-Resolution Science Experiment camera (Hirise). The red line is the drive path of *Opportunity* exploring the crater. (Courtesy NASA, JPL, ASU, Cornell University)

(Thermal Emission Spectrometer) instrument indicated the metallic nature of the rock [340]. Observations made with the panoramic camera and the microscopic image revealed that the surface of the rock is covered with pits interpreted as regmaglypts and indicate the presence of a coating on the surface. The α -Particle-X-ray spectrometer (APXS) and the Mössbauer spectrometer were used to investigate the undisturbed and the brushed surface of the rock. Based on the Ni and Ge

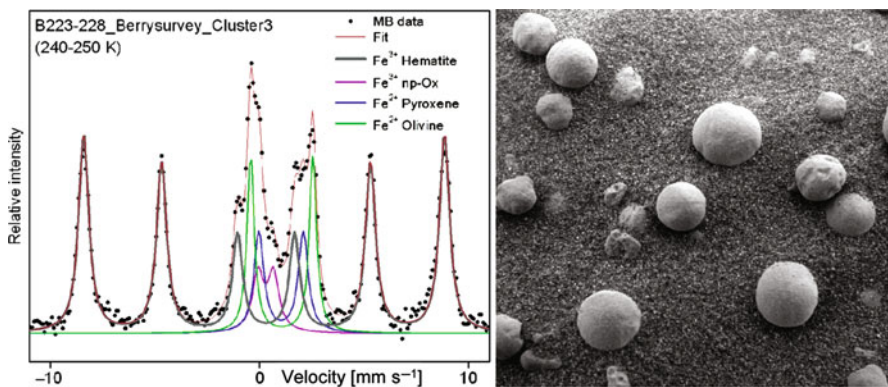


Fig. 8.37 *Left:* spectrum of an accumulation of hematite rich spherules (*Blueberries*) on top of basaltic soil (Sol 223–228 of the mission; 1 Sol = 1 Martian day). The spectrum is dominated by the hematite signal. Estimations based on area ratios (blueberries/soil) and APXS data indicate that the blueberries are composed mainly of hematite. *Right:* MI picture ($3 \times 3 \text{ cm}^2$) of hematitic spherules (*blueberries*) on basaltic soil at Meridiani Planum

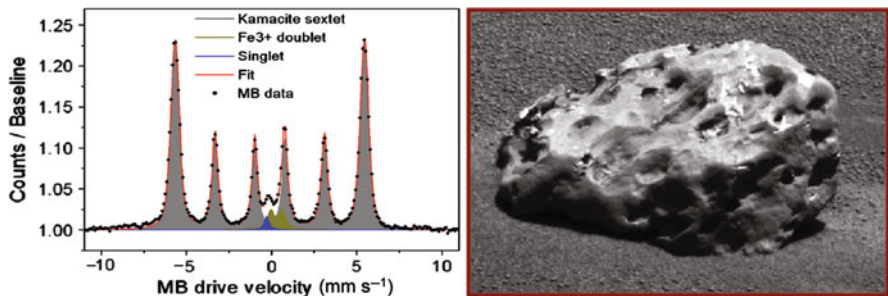


Fig. 8.38 (*Left*): The Mössbauer spectrum of the rock called “Heat Shield rock,” clearly shows with high intensity the mineral Kamacite, an Fe–Ni alloy with about 6–7% Ni; (*Right*): The iron–nickel meteorite “Meridiani Planum” (originally called “Heat Shield Rock”) at Opportunity landing site, close to the crater Endurance. The meteorite is about 30 cm across (Courtesy NASA, JPL, Cornell University)

contents derived by APXS, Meridiani Planum was classified as an iron meteorite of the IAB complex. The brushed meteorite surface was found to be enriched in P, S and Cl in comparison to Martian soil.

Mössbauer Spectral Analysis and Analog Measurements. Mössbauer spectra were obtained in the temperature range between 200 and 270 K and in two different energy windows (14.4 and 6.4 keV), which provide depth selective information about a sample [346]. To compensate for low counting statistics due to limited integration time, all available spectra were summed for the integrations on the undisturbed and brushed surface, respectively. In addition to kamacite (α -(Fe,Ni)) (~85%) and small amounts of ferric oxide (see Fig. 8.38), all spectra exhibit features indicative for an additional mineral phase. Based on analog measurements

performed with a specimen of the Mundrabilla Iron meteorite, the additional spectral features can be attributed to schreibersite ($(\text{Fe},\text{Ni})_3\text{P}$) [360]. Mineral inclusions of schreibersite in Meridiani Planum are also consistent with an enrichment of P observed with the APXS [360].

Besides this iron meteorite, there have been four other rocks identified to be probably of meteoritic origin. These centimeter-sized pebbles, named *Barberton*, *Santa Catarina*, *Santorini* and *Kasos*, show troilite and/or kamacite signatures in the corresponding Mössbauer spectra [359]. The range of Fe oxidation states suggests the presence of a fusion crust. The four cobbles have a very similar chemical composition determined by the APXS, and therefore they may be fragments of the same impactor that created *Victoria Crater* [361].

Victoria Crater. After a journey of more than 950 Sols (1 Sol = 1 Martian day ~ 24 h and 37 min) or more than 2.5 Earth years (~ 1.3 Martian years), Opportunity arrived at the 750 m diameter crater Victoria (Fig. 8.36) [335], after traveling across the plains of Meridiani Planum more than 10 km to the south from its landing site in Eagle Crater. The rover has explored this eroded impact crater for more than 750 Sols (more than 2 Earth years or 1 Martian year), descending into the crater on Sol 1293 to begin in situ physical and chemical/mineralogical observations. After exiting the crater on Sol 1634, Opportunity performed more imaging and in situ investigations to the southwest of *Duck Bay*, name of a part of the crater rim, before leaving Victoria heading south toward a 20 km diameter crater named Endeavor.

The outline of Victoria Crater is serrated, with sharp and steep promontories separated by rounded alcoves (Fig. 8.36). The crater formed in sulfate-rich sedimentary rocks, and is surrounded by a smooth terrain that extends about one crater diameter from the rim. On the crater floor is a dune field. There are no perched ejecta blocks preserved on the smooth terrain around the crater rim, probably planed off by Aeolian abrasion. The Mössbauer mineralogy of the sedimentary rocks at the crater rim and inside the crater itself is nearly the same as at Eagle crater landing site and Endurance crater, both about 6–8 km away [335].

The soil close to the crater rim, at the exit point of Opportunity, shows a high hematite content in the Mössbauer spectrum (Fig. 8.36), which can be attributed to the presence of hematite spherules (*blueberries*).

8.3.3.2 Terrestrial Applications

In Situ Monitoring of Airborne Particles. The identification of air pollution sources is one of the main goals of any monitoring and controlling of the air quality in an industrialized urban region. In the metropolitan region of Vitoria (MRV), Espírito Santo, Brazil, monitoring and analysis of iron-bearing materials in airborne particles in atmospheric aerosols was performed using MIMOS II [362]. The MRV covers an area of 1,461 km². This region has nearly 1.3 million inhabitants, houses a large industrial complex, is undergoing a rapid expansion and has to bear an intense traffic. During the second half of the 1980s, particulate matter (TSP)

concentration above $80 \mu\text{g m}^{-3}$ was recorded. These concentrations did not comply with the Brazilian air quality standards. High pollution concentration was also associated with a period of low pluviometric precipitation, strong winds, vegetation burnings, and intense industrial activities. A MIMOS II instrument was installed inside an airborne particle sampler. MIMOS II operated very stable in field, and the performance was not affected by the vibrations of the air pump system. The obtained results are in good agreement with the results recorded in the laboratory. Hematite was identified as a predominant phase in the suspended particles from MRV. As subordinate phases geothite (GT), pyrite, iron-containing silicates and, sometimes, an ultrafine Fe^{3+} phase were detected. The hematite comes mostly from the industrial plants producing iron ore pellets and from soil, GT from soil and pyrite from handling and storing coal in the industrial area. Ultrafine particles are a result of strongly weathered tropical soils and industrial emissions. Eventually, magnetite was also found. Magnetite is related to steelwork plants and silicates stem from soil and civil constructions.

In Situ Monitoring of Soils Below the Surface. Iron in soil is one of the five most important chemical elements in abundance. It plays a major role in biogeochemical cycles as electron donor and acceptor in oxido-reduction reactions, the main source of energy for life. Iron minerals found in soils are iron oxides (most abundant), clay minerals, and less commonly, iron sulfides and carbonates. Soil genesis and soil properties are influenced by iron in minerals and in soil solution [363]. In order to monitor in situ transformations of iron minerals in soils, a special experimental setup for subsurface in-field applications was developed at the University of Mainz [363, 364]. A modified version of the instrument MIMOS II is mounted on a movable platform inside a 2 m long and 20 cm diameter Plexiglas tube, which has been installed in hydromorphic soil in the field. Positioning of the sensor head to different depths is done by a stepping motor arrangement with an accuracy of about 1 mm. Also, dedicated software for running measurement sequences (e.g., different depth positions at different times etc.) was developed. The setup can work autonomously up to several months in the field.

Experimental results confirm that the fougérite mineral found in hydromorphic soils is $\text{Fe(II)}/\text{Fe(III)}$ hydroxycarbonate green rust. With a total iron concentration of about 4% in the bulk soil, spectra were obtained after 1–2 days of count accumulation. Calibrations were done in the laboratory. The example spectra demonstrate that the instrument can acquire Mössbauer spectra with reasonable statistics even with low-intensity sources. The spectra display three quadrupole doublets (D1, D2, and D3) associated with the fougérite mineral encountered in gley soils and responsible for their bluish-green color where D1 and D2 with a large quadrupole splitting are attributed to Fe(II) state and D3 to Fe(III) . Intensities of the peaks that are found to be 50, 10, and 40% from computer fitting are consistent with the $\text{Fe(II)}/\text{Fe(III)}$ hydroxycarbonate green rust where stoichiometry intensity ratios are 1/2:1/6:1/3 [363].

Archaeological Artifacts. A Lekythos Greek vase (500 years b.c.) was analyzed by backscattering Mössbauer spectroscopy [365, 366]. This Lekythos vase has three black human figures with small red-painted details painted on a yellow-fired clay

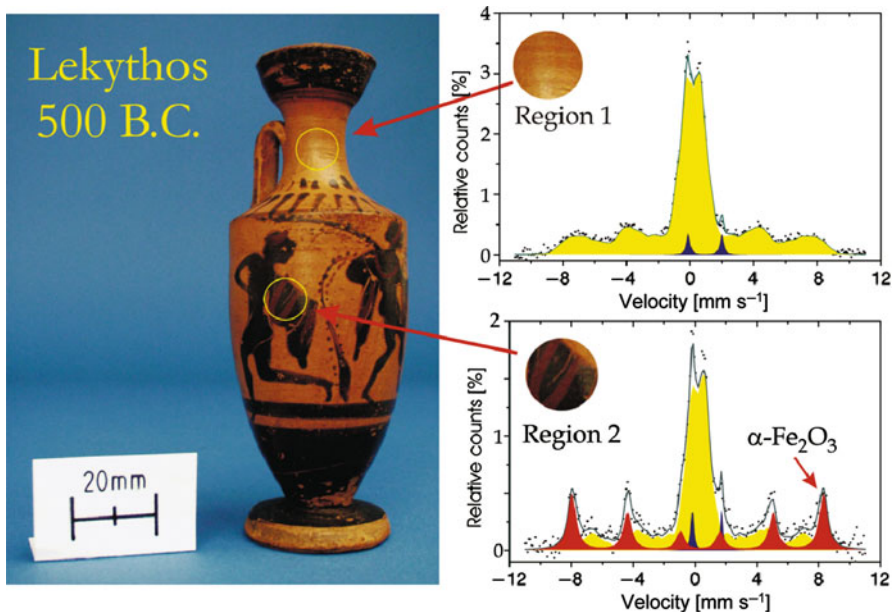


Fig. 8.39 Picture of the Lekythos vase (500 years B.C.), and two examples of spectra obtained with the portable spectrometer MIMOS II at the areas indicated in the figure above. The circular field of view of the instrument was set to about 1 cm diameter

(Fig. 8.39). The Lekythos vase was built as an oil or perfume jar having an ellipsoidal body, narrow neck, flanged mouth, curved handle, and a narrow base terminating in a foot. It was used chiefly for ointments and religious (funerary) ceremonies. This is substantiated by the fact that Lekythos have been found in and around tombs and excavated from ancient homes. Mössbauer backscattering spectra were recorded at room temperature with MIMOS II in three different regions of the Lekythos vase (Fig. 8.39). One was on nonpainted surfaces and the other was on the painted surfaces (only black-painted, and black with red details). Free painted surface shows a broad spectrum that can be associated with poor-crystallized iron oxides produced during the firing clay process. The painted surfaces show, in addition to the characteristic nonpainted area, a well-defined sextet. The Mössbauer parameters of this sextet correspond to well-crystallized hematite. The Mössbauer spectrum taken over the red painted details shows no significant difference from the nonpainted surface. Therefore, the red details are presumably iron-free.

The usefulness of this nondestructive technique may go further than pigment characterization, and it is proposed as an additional method for checking the authenticity of ancient archaeological artifacts.

Rock Paintings in the Field. The manufacturing and composition of paints from prehistoric periods are of great archaeological interest because it is possible to deduce aspects of the ancient cultures based on their abilities to produce works of arts. Many pigments used in ancient paintings are iron-based compounds. In most

cases, for obvious reasons, it is impossible to remove samples, and therefore in situ methods have to be applied.

The impressive paintings in Santana do Riacho, associated with the recent development of the spectrometer MIMOS II, prompted the authors to perform, for the first time, nondestructive in situ Mössbauer measurements on ancient rock paintings in Brazil (near Belo Horizonte, Minas Gerais) [366–369]. We have used a prototype of the instrument to investigate the iron oxide composition of rock paintings in the field. The instrument was mounted on a tripod, and the power was supplied by battery (see Fig. 8.40a). Spectra were collected during 24–48 h (~ 30 mCi $^{57}\text{Co}/\text{Rh}$ source), with an average daily temperature of 27–32°C and 18–22°C during night.

The archaeological site of Santana do Riacho is located at about 90 km north-eastern of Belo Horizonte, in the “Serra do Cipó” region. The natural shelter of the archaeological site where the rock paintings were made is approximately 80 m long and 5 m high. Excavations of all sorts of materials (bones, stones, pigmented materials, etc.) have been performed over the years and a vast body of information was collected. Hundreds of prehistorical paintings are clearly visible all over the wall, but so far, no conclusive proof exists about the nature of the materials (e.g., paints) that were used in these drawings. The vast majority of the paintings are red

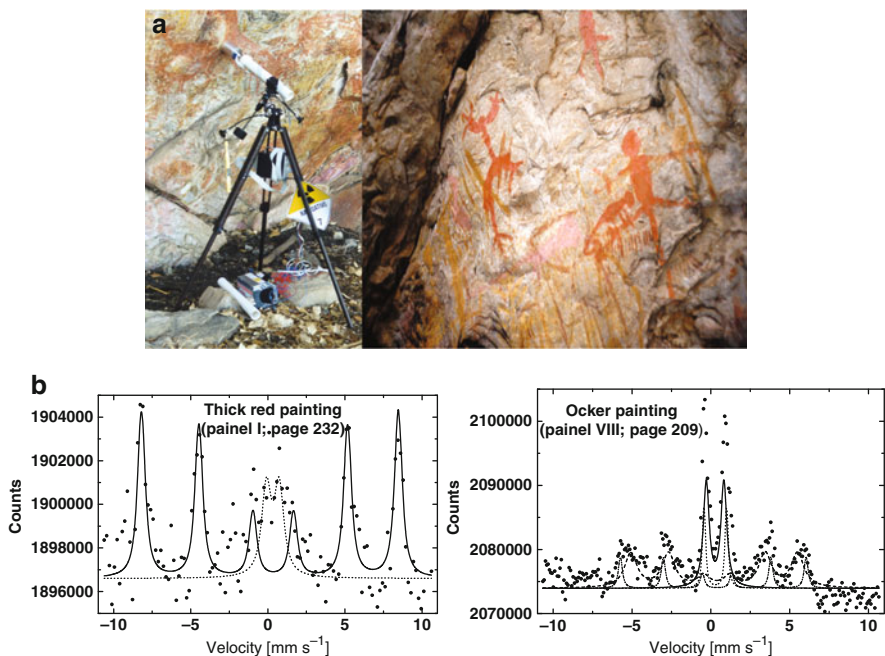


Fig. 8.40 (a). The MIMOS II instrument is mounted on a tripod and positioned to the picture of interest (left); part of the wall showing several distinct paintings with different colors (right). (b). Mössbauer spectra of (1) the thick red painting located in panel I, page 232, and (2) the ochre painting located in panel VIII, page 209 of the book about the archaeological site of Santana do Riacho, Brazil [368, 369]

(70%) and yellow (20%), but there are others in orange, black, brown, and ochre. Iron oxides are most probably the pigments that were used. The paintings were selected based on their colors and apparent thickness, and six spots were measured. The analysis of the data suggests that hematite and GT seem to be the pigments responsible for the red and yellow colors (see Fig. 8.40b), but no conclusion was yet found for an ochre painting. Possibly, it is related to the mineral jarosite.

8.3.3.3 The Advanced Instrument MIMOS IIa

The Mars-Exploration-Rover mission has demonstrated that Mössbauer spectroscopy is an important tool for the in situ exploration of extraterrestrial bodies and the study of Fe-bearing samples. MIMOS II is part of the scientific payload of future space missions, in particular, Phobos Grunt (Russian Space Agency; 2011) and ExoMars (European Space Agency (ESA) and NASA; 2018). In comparison to MIMOS II, the instrument under development for ExoMars will use Si-Drift detectors (SDD) which also allows high-resolution XRF analysis in parallel to Mössbauer spectroscopy [366, 370, 371]. The new design of the improved version of the MIMOS II instrument is lighter than the MER instrument. A new ring detector system of four SDDs [370] will replace the four Si-PIN detectors of the current version greatly improving the energy resolution and the area fill factor around the collimator. The SDDs with a sensitive area of $2 \times 45 \text{ mm}^2$ each exhibit an energy resolution $<280 \text{ eV}$ at room temperature approaching the theoretical limit of $\sim 130 \text{ eV}$ at moderate cooling (about -20°C). This results in an increase of the signal to noise ratio (SNR) (or sensitivity) of more than a factor of 10 (Fig. 8.41). In addition to the Mössbauer data, SDD allows the simultaneous acquisition of the XRF spectrum, thus providing data on the sample's elemental composition (Fig. 8.41). For more details, see Sect. 3.3.

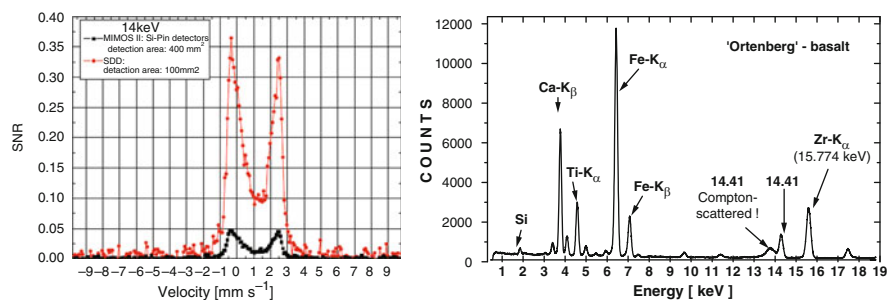


Fig. 8.41 *Left:* Comparison of SNR of 14.4 keV Mössbauer spectra, taken with a Si-PIN detector system (MER instrument; four diodes) and with a SDD detector system (advanced MIMOS instrument; only one diode chip); *Right:* X-ray spectrum of a basalt (Ortenberg basalt; see [366, 371]), taken with a high resolution Si-drift detector system at ambient pressure (1 atm), demonstrating the XRF capability of the “advanced MIMOS” instrument. Excitation source: $^{57}\text{Co}/\text{Rh}$ Mössbauer source. Energy resolution: about 170 eV at $+10^\circ\text{C}$ (SDD temperature)

8.3.4 Conclusions and Outlook

The miniaturized Mössbauer instruments have proven as part of the NASA Mars Exploration Rover 2003 mission that Mössbauer spectroscopy is a powerful tool for planetary exploration, including our planet Earth. For the advanced model of MIMOS II, the new detector technologies and electronic components increase sensitivity and performance significantly. In combination with the high-energy resolution of the SDD, it will be possible to perform XRF analysis in parallel to Mössbauer spectroscopy. In addition to the Fe-mineralogy, information on the sample's elemental composition will be obtained.

The instrument MIMOS II will be part of the upcoming ESA–NASA space missions ExoMars in 2018, and the Russian Space Agency sample return mission Phobos Grunt scheduled for launch in 2011 to visit the Mars moon Phobos.

The miniaturized Mössbauer spectrometer MIMOS II has been used already in several terrestrial applications which would not have been possible before. A number of other possible terrestrial applications, for example, in the field, in industry, and fundamental research, are under consideration. With the new generation of the Mössbauer spectrometer MIMOS II, the method itself can be applied to numerous new fields in research, environmental science, planetary science, and many other fields. Because of this reason, Mössbauer spectroscopy may become a more widely used method than it is today.

References

References to Sect. 8.1

1. König, E.: *Coord. Chem. Rev.* **3**, 471 (1968)
2. Goodwin, H.A.: *Coord. Chem. Rev.* **18**, 293 (1976)
3. Gütlich, P.: *Struct. Bond. (Berlin)* **44**, 83 (1981)
4. Gütlich, P., Hauser, A., Spiering, H.: *Angew. Chem. Int. Ed.* **33**, 20 (1994)
5. Gütlich, P., Goodwin, H.A., (eds.): *Top. Curr. Chem.* 233–235 (2004)
6. Gütlich, P., Garcia, Y., Spiering, H.: In: Miller, J.S., Drillon, M. (eds.) *Magnetism: Molecules to Materials IV*, p. 271. Wiley-VCH, Weinheim (2003)
7. Dézsi, I., Molnar, B., Tarnozci, T., Tompa, K.: *J. Inorg. Nucl. Chem.* **29**, 2486 (1967)
8. Jesson, J.P., Weiher, J.F.: *J. Chem. Phys.* **46**, 1995 (1967)
9. Jesson, J.P., Weiher, J.F., Trofimenko, S.: *J. Chem. Phys.* **48**, 2058 (1968)
10. Long, G.J., Grandjean, F., Reger, D.L.: *Top. Curr. Chem.* **233**, 91 (2004)
11. Sorai, M., Ensling, J., Gütlich, P.: *Chem. Phys.* **18**, 199 (1976)
12. Gütlich, P., Link, R., Steinhäuser, H.G.: *Inorg. Chem.* **17**, 2509 (1978)
13. Spiering, H., Meissner, E., Köppen, H., Müller, E.W., Gütlich, P.: *Chem. Phys.* **68**, 65 (1982)
14. Sorai, M., Ensling, J., Hasselbach, K.M., Gütlich, P.: *Chem. Phys.* **20**, 197 (1977)
15. Gütlich, P., Köppen, H., Steinhäuser, H.G.: *Chem. Phys. Lett.* **74**, 475 (1980)
16. Köppen, H., Müller, E.W., Köhler, C.P., Spiering, H., Meissner, E., Gütlich, P.: *Chem. Phys. Lett.* **91**, 348 (1982)

17. Drickamer, H.G.: *Angew. Chem.* **86**, 61 (1974)
18. Meissner, E., Köppen, H., Spiering, H., Gütlich, P.: *Chem. Phys. Lett.* **95**, 163 (1983)
19. Köhler, C.P., Jakobi, R., Meissner, E., Wiehl, L., Spiering, H., Gütlich, P.: *J. Phys. Chem. Solids* **51**, 239 (1990)
20. Decurtins, S., Gütlich, P., Köhler, C.P., Spiering, H., Hauser, A.: *Chem. Phys. Lett.* **105**, 1 (1984)
21. Decurtins, S., Gütlich, P., Hasselbach, K.M., Hauser, A., Spiering, H.: *Inorg. Chem.* **24**, 2174 (1985)
22. Hauser, A.: *Chem. Phys. Lett.* **124**, 543 (1986)
23. Poganiuch, P., Decurtins, S., Gütlich, P.: *J. Am. Chem. Soc.* **112**, 3270 (1990)
24. Real, J.A., Gaspar, A.B., Muñoz, M.C., Gütlich, P., Ksenofontov, V., Spiering, H.: *Top. Curr. Chem.* **233**, 167 (2004)
25. Real, J.A., Zarembowitch, J., Kahn, O., Solans, X.: *Inorg. Chem.* **26**, 2939 (1987)
26. Real, J.A., Bolvin, H., Bousseksou, A., Dworkin, A., Kahn, O., Varret, F., Zarembowitch, J.: *J. Am. Chem. Soc.* **114**, 4650 (1992)
27. Ksenofontov, V., Spiering, H., Reiman, S., Garcia, Y., Gaspar, A.B., Moliner, N., Real, J.A., Gütlich, P.: *Chem. Phys. Lett.* **348**, 381 (2001)
28. Zimmermann, R., Ritter, G., Spiering, H.: *Chem. Phys.* **4**, 133 (1974)
29. Zimmermann, R., Ritter, G., Spiering, H., Nagy, D.L.: *J. Phys.* **35**, C6 (1974)
30. Yoneda, K., Nakano, K., Fujioka, J., Yamada, K., Suzuki, T., Fuyuhiro, A., Kawata, S., Kaizaki, S.: *Polyhedron* **24**, 2437 (2005)
31. Yoneda, K., Adachi, K., Hayami, S., Maeda, Y., Katada, M., Fuyuhiro, A., Kawata, S., Kaizaki, S.: *Chem. Commun.*, 45 (2006)
32. Grunert, C.M., Reiman, S., Spiering, H., Kitchen, J.A., Brooker, S., Gütlich, P.: *Angew. Chem. Int. Ed.* **47**, 2997 (2008)
33. Klingele, M.H., Moubaraki, B., Cashion, J.D., Murray, K.S., Brooker, S.: *Chem. Commun.*, 987 (2005)
34. Klingele, M.H., Moubaraki, B., Murray, K.S., Brooker, S.: *Chem. Eur. J.* **11**, 6962 (2005)
35. Kolnaar, J.J.A., van Dijk, G., Kooijman, H., Spek, A.L., Ksenofontov, V., Gütlich, P., Haasnoot, J.G., Reedijk, J.: *Inorg. Chem.* **36**, 2433 (1997)
36. Galyametdinov, Y., Ksenofontov, V., Prosvirin, A., Ovchinnikov, I., Ivanova, G., Gütlich, P., Haase, W.: *Angew. Chem. Int. Ed.* **40**, 4269 (2001)
37. Fujigaya, T., Jiang, D.L., Aida, T.: *J. Am. Chem. Soc.* **125**, 14690 (2003)
38. Hayami, S., Danjohbara, K., Inoue, K., Ogawa, Y., Matsumoto, N., Maeda, Y.: *Adv. Mater.* **16**, 869 (2004)
39. Hayami, S., Moriyama, R., Shuto, A., Maeda, Y., Ohta, K., Inoue, K.: *Inorg. Chem.* **46**, 7692 (2007)
40. Hayami, S., Motokawa, N., Shuto, A., Masuhara, N., Someya, T., Ogawa, Y., Inoue, K., Maeda, Y.: *Inorg. Chem.* **46**, 1789 (2007)
41. Seredyuk, M., Gaspar, A.B., Ksenofontov, V., Galyametdinov, Y., Kusz, J., Gütlich, P.: *Adv. Funct. Mater.* **18**, 2089 (2008)
42. Seredyuk, M., Gaspar, A.B., Ksenofontov, V., Galyametdinov, Y., Verdaguera, M., Villain, F., Gütlich, P.: *Inorg. Chem.* **47**, 10232 (2008)
43. Seredyuk, M., Gaspar, A.B., Ksenofontov, V., Galyametdinov, Y., Kusz, J., Gütlich, P.: *J. Am. Chem. Soc.* **130**, 1431 (2008)
44. Seredyuk, M., Gaspar, A.B., Ksenofontov, V., Reiman, S., Galyametdinov, Y., Haase, W., Rentschler, E., Gütlich, P.: *Chem. Mater.* **18**, 2513 (2006)
45. Seredyuk, M., Gaspar, A.B., Ksenofontov, V., Reiman, S., Galyametdinov, Y., Haase, W., Rentschler, E., Gütlich, P.: *Hyperfine Interact.* **166**, 385 (2006)
46. Matsuura, T. (ed.): *Hot Atom Chemistry*. Kodansha, Tokyo (1984)
47. Sano, H., Gütlich, P.: *Hot Atom Chemistry*. Kodansha, Tokyo (1984) (and references therein)

48. Ensling, J., Fitzsimmons, B.W., Gütlich, P., Hasselbach, K.M.: *Angew. Chem. Int. Ed.* **9**, 637 (1970)
49. Ensling, J., Gütlich, P., Hasselbach, K.M., Fitzsimmons, B.W.: *Chem. Phys. Lett.* **42**, 232 (1976)
50. Gütlich, P.: *Top. Curr. Chem.* **234**, 231 (2004)
51. Deisenroth, S., Hauser, A., Spiering, H., Gütlich, P.: *Hyperfine Interact.* **93**, 1573 (1994)
52. Hauser, A.: *Chem. Phys. Lett.* **173**, 507 (1990)
53. Oshio, A., Spiering, H., Ksenofontov, V., Renz, F., Gütlich, P.: *Inorg. Chem.* **40**, 1143 (2001)

References to Sect. 8.2

54. Griffith, J.S.: *J. Inorg. Nucl. Chem.* **2**, 1–10 (1956)
55. Griffith, J.S.: *Discuss. Faraday Soc.* **26**, 8–86 (1959)
56. Hoskins, B.F., Martin, R.L., White, A.H.: *Nature* **211**, 627–628 (1966)
57. Maltempo, M.M.: *J. Chem. Phys.* **61**, 2540–2547 (1974)
58. Maltempo, M.M., Moss, T.H., Cusanovich, M.A.: *Biochim. Biophys. Acta* **342**, 290–305 (1974)
59. Maltempo, M.M., Moss, T.H.: *Q. Rev. Biophys.* **9**, 181–215 (1976)
60. Maltempo, M.M., Ohlsson, P.I., Paul, K.G., Petersson, L., Ehrenberg, A.: *Biochemistry* **18**, 2935–2941 (1979)
61. LaMar, G.N., Jackson, J.T., Dugad, L.B., Cusanovich, M.A.: *J. Biol. Chem.* **265**, 16173–16180 (1990)
62. Fujii, S., Yoshimura, T., Kamada, H., Yamaguchi, K., Suzuki, S., Takakwa, S.: *Biochim. Biophys. Acta – Protein Struct. Mol. Enzym.* **1251**, 161 (1995)
63. Schulz, C.E., Rutter, R., Sage, J.T., Debrunner, P.G., Hager, L.P.: *Biochemistry* **23**, 4743–4754 (1984)
64. Schauer, C.K., Akabori, K., Elliott, C.M., Anderson, O.P.: *J. Am. Chem. Soc.* **106**, 1127–1128 (1984)
65. Karlin, K.D.: *Dithiolene Chemistry: Synthesis, Properties, and Applications*, vol. 52. Wiley, New York (2004)
66. De Vries, J.L.K.F., Keijzers, C.P., De Boer, E.: *Inorg. Chem.* **11**, 1343–1348 (1972)
67. Niarchos, D., Kostikas, A., Simopoulos, A., Coucouvanis, D., Piltingsrud, D., Coffman, R.E.: *J. Chem. Phys.* **69**, 4411–4418 (1978)
68. Keutel, H., Käplinger, I., Jäger, E.-G., Grodzicki, M., Schünemann, V., Trautwein, A.X.: *Inorg. Chem* **38**, 2320–2327 (1999)
69. Dolphin, D.H., Sams, J.R., Tsin, T.B.: *Inorg. Chem.* **16**, 711–713 (1977)
70. Wickman, H.H., Trozzolo, A.M., Williams, H.J., Hull, G.W., Merritt, F.R.: *Phys. Rev.* **155**, 563 (1967)
71. Harris, G.: *Theor. Chim. Acta* **10**, 119–154 (1968)
72. Harris, G.: *Theor. Chim. Acta* **10**, 155–180 (1968)
73. Patra, A.K., Bill, E., Bothe, E., Chlopek, K., Neese, F., Weyhermüller, T., Stobie, K., Ward, M.D., McCleverty, J.A., Wieghardt, K.: *Inorg. Chem.* **45**, 7877–7890 (2006)
74. Chlopek, K., Muresan, N., Neese, F., Wieghardt, K.: *Chem. Eur. J.* **13**, 8391–8403 (2007)
75. Ray, K., George, S.D., Solomon, E.I., Wieghardt, K., Neese, F.: *Chem. Eur. J.* **13**, 2783–2797 (2007)
76. Ganguli, P., Marathe, V.R., Mitra, S.: *Inorg. Chem.* **14**, 970–973 (1975)
77. Wickman, H.H., Wagner, C.F.: *J. Chem. Phys.* **51**, 435–444 (1969)
78. Chapps, G.E., McCann, S.W., Wickman, H.H., Sherwood, R.C.: *J. Chem. Phys.* **60**, 990–997 (1974)
79. Wickman, H.H., Merritt, F.R.: *Chem. Phys. Lett.* **1**, 117–118 (1967)

80. Wickman, H.H., Trozzolo, A.M., Williams, H.J., Hull, G.W., Merritt, F.R. Bell Telephone Research Reports, Murray Hill, NJ. (1967)
81. Wickman, H.H., Trozzolo, A.M.: Inorg. Chem. **7**, 63–68 (1968)
82. Petridis, D., Simopoulos, A., Kostikas, A., Pasternak, M.: J. Chem. Phys. **65**, 3139–3145 (1976)
83. Wickman, H.H.: J. Chem. Phys. **56**, 976–982 (1972)
84. Grow, J.M., Hopkins, T.E., Robbins, G.L., Silverthorn, W.E., Wickman, H.H.: J. Chem. Phys. **67**, 5275–5281 (1977)
85. Grow, J.M., Robbins, G.L., Wickman, H.H.: J. Chem. Phys. **67**, 5282–5290 (1977)
86. De Vries, J.L.K.F., Trooster, J.M., De Boer, E.: Inorg. Chem. **10**, 81–85 (1971)
87. Birchall, T., Greenwood, N.N.: J. Chem. Soc. A, 286–291 (1969)
88. Fettouhi, M., Morsy, M., Waheed, A., Golhen, S., Ouahab, L., Sutter, J.-P., Kahn, O., Menendez, N., Varret, F.: Inorg. Chem. **38**, 4910–4912 (1999)
89. Sellmann, D., Geck, M., Knoch, F., Ritter, G., Dengler, J.: J. Am. Chem. Soc. **113**, 3819 (1991)
90. Sellmann, D., Emig, S., Heinemann, F.W.: Angew. Chem. Int. Ed. Engl. **36**, 1734–1736 (1997)
91. Sellmann, D., Emig, S., Heinemann, F.W., Knoch, F.: Angew. Chem. Int. Ed. Engl. **36**, 1201–1203 (1997)
92. Ray, K., Bill, E., Weyhermüller, T., Wieghardt, K.: J. Am. Chem. Soc. **127**, 5641–5654 (2005)
93. Fallon, G.D., Gatehouse, B.M., Marini, P.J., Murray, K.S., West, B.O.: J. Chem. Soc. Dalton Trans., 2733–2739 (1984)
94. Ghosh, P., Bill, E., Weyhermüller, T., Wieghardt, K.: J. Am. Chem. Soc. **125**, 3967–3979 (2003)
95. Chun, H., Weyhermüller, T., Bill, E., Wieghardt, K.: Angew. Chem. Int. Ed. **40**, 2489 (2001)
96. Chun, H.P., Bill, E., Weyhermüller, T., Wieghardt, K.: Inorg. Chem. **42**, 5612–5620 (2003)
97. Blanchard, S., Bill, E., Weyhermüller, T., Wieghardt, K.: Inorg. Chem. **43**, 2324–2329 (2004)
98. Chlopek, K., Bill, E., Weyhermüller, T., Wieghardt, K.: Inorg. Chem. **44**, 7087–7098 (2005)
99. Koch, S., Holm, R.H., Frankel, R.B.: J. Am. Chem. Soc. **97**, 6714–6723 (2002)
100. Kostka, K.L., Fox, B.G., Hendrich, M.P., Collins, T.J., Rickard, C.E.F., Wright, L.J., Münck, E.: J. Am. Chem. Soc. **115**, 6746–6757 (1993)
101. Simonato, J.-P., Pecaut, J., Le Pape, L., Oddou, J.-L., Jeandey, C., Shang, M., Scheidt, W.R., Wojaczynski, J., Wolowiec, S., Latos-Grazynski, L., Marchon, J.-C.: Inorg. Chem. **39**, 3978–3987 (2000)
102. Ikeue, T., Ohgo, Y., Yamaguchi, T., Takahashi, M., Takeda, M., Nakamura, M.: Angew. Chem. Int. Ed. **40**, 2617–2620 (2001)
103. Koch, W.O., Schünemann, V., Gerdan, M., Trautwein, A.X., Krüger, H.-J.: Chem. Eur. J. **4**, 686–691 (1998)
104. Weiss, R., Gold, A., Terner, J.: Chem. Rev. **106**, 2550–2579 (2006)
105. Ogoshi, H., Watanabe, E., Yoshida, Z.: Chem. Lett., 989–992 (1973)
106. Kastner, M.E., Scheidt, W.R., Mashiko, T., Reed, C.A.: J. Am. Chem. Soc. **100**, 666–667 (1978)
107. Reed, C.A., Mashiko, T., Bentley, S.P., Kastner, M.E., Scheidt, W.R., Spartalian, K., Lang, G.: J. Am. Chem. Soc. **101**, 2948–2958 (1979)
108. Masuda, H., Taga, T., Osaki, K., Sugimoto, H., Yoshida, Z., Ogoshi, H.: Inorg. Chem. **19**, 950–955 (1980)
109. Boersma, A.D., Goff, H.M.: Inorg. Chem. **21**, 581–586 (1982)
110. Toney, G.E., Gold, A., Savrin, J., Terhaar, L.W., Sangaiah, R., Hatfield, W.E.: Inorg. Chem. **23**, 4350–4352 (1984)
111. Gupta, G.P., Lang, G., Lee, Y.J., Scheidt, W.R., Shelly, K., Reed, C.A.: Inorg. Chem. **26**, 3022–3030 (1987)

112. Dugad, L.B., Mitra, S.: Proc. Indian Acad. Sci. Chem. Sci. **93**, 295–311 (1984)
113. Scheidt, W.R., Osvath, S.R., Lee, Y.J., Reed, C.A., Shaevitz, B., Gupta, G.P.: Inorg. Chem. **28**, 1591–1595 (1989)
114. Gismelseed, A., Bominaar, E.L., Bill, E., Trautwein, A.X., Winkler, H., Nasri, H., Doppelt, P., Mandon, D., Fischer, J., Weiss, R.: Inorg. Chem. **29**, 2741–2749 (1990)
115. Goff, H., Shimomura, E.: J. Am. Chem. Soc. **102**, 31–37 (1980)
116. Nessel, M.J.M., Cai, S., Shokhireva, T.K., Shokhirev, N.V., Jacobson, S.E., Jayaraj, K., Gold, A., Walker, F.A.: Inorg. Chem. **39**, 532–540 (2000)
117. Debrunner, P.G.: Mössbauer spectroscopy of iron porphyrins. In: Lever, A.B.P., Gray, H.B. (eds.) Iron Porphyrins Part III, pp. 137–234. VCH, Weinheim (1989)
118. Kintner, E.T., Dawson, J.H.: Inorg. Chem. **30**, 4892–4897 (1991)
119. Gupta, G.P., Lang, G., Scheidt, W.R., Geiger, D.K., Reed, C.A.: J. Chem. Phys. **85**, 5212–5220 (1986)
120. Kennedy, B.J., Murray, K.S., Zwack, P.R., Homborg, H., Kalz, W.: Inorg. Chem. **25**, 2539–2545 (1986)
121. Fang, M., Wilson, S.R., Suslick, K.S.: J. Am. Chem. Soc. **130**, 1134–1135 (2008)
122. Alonso, P.J., Arauzo, A.B., Forniés, J., García-Monforte, M.A., Martínez, A.M.J.I., Menjón, B., Rillo, C., Sáiz-Garitaonandia, J.J.: Angew. Chem. Int. Ed. **45**, 6707–6711 (2006)
123. Gupta, G.P., Lang, G., Reed, C.A., Shelly, K., Scheidt, W.R.: J. Chem. Phys. **86**, 5288–5293 (1987)
124. Schünemann, V., Gerdan, M., Trautwein, A.X., Haoudi, N., Mandon, D., Fischer, J., Weiss, R., Tabard, A., Guillard, R.: Angew. Chem. Int. Ed. **38**, 3181–3183 (1999)
125. Ogoshi, H., Sugimoto, H., Watanabe, E., Yoshida, Z., Maeda, Y., Sakai, H.: Bull. Chem. Soc. Jpn. **54**, 3414–3419 (1981)
126. Reed, C.A., Guiiset, F.: J. Am. Chem. Soc. **118**, 3281–3282 (1996)
127. Klemm, L., Klemm, W.: J. Prakt. Chem. **143**, 82–89 (1935)
128. Lever, A.B.P.: J. Chem. Soc., 1821–1829 (1965)
129. Dale, B.W., Williams, R.J.P., Johnson, C.E., Thorp, T.L.: J. Chem. Phys. **49**, 3441–3444 (1968)
130. Barracough, C.G., Martin, R.L., Mitra, S., Sherwood, R.C.: J. Chem. Phys. **53**, 1643–1648 (1970)
131. Labarta, A., Molins, E., Vinas, X., Tejada, J., Caubet, A., Alvarez, S.: J. Chem. Phys. **80**, 444–448 (1984)
132. Filoti, G., Kuz'min, M.D., Bartolome, J.: Phys. Rev. B Condens. Matter Mater. Phys. **74**, 134420 (2006)
133. Ercolani, C., Neri, C., Porta, P.: Inorg. Chim. Acta **1**, 415 (1967)
134. Linstead, R.P., Robertson, J.M.: J. Chem. Soc. **1936**, 1736 (1936)
135. Hudson, A., Whitefield, H.J.: Inorg. Chem. **6**, 1120–1123 (1966)
136. Dale, B.W., Williams, R.J.P., Edwards, P.R., Johnson, C.E.: J. Chem. Phys. **49**, 3445–3449 (1968)
137. Deszi, I., Balazs, A., Molnar, B., Grobchenko, V.D., Kukoshevich, L.I.: J. Inorg. Nucl. Chem. **31**, 1661 (1969)
138. Dale, B.W.: Mol. Phys. **28**, 503–511 (1974)
139. Bell, N.A., Brooks, J.S., Robinson, J.K., Thorpe, S.C.: J. Chem. Soc. Faraday Trans. **94**, 3155 (1998)
140. Grenoble, D.C., Drickamer, H.G.: J. Chem. Phys. **35**, 1624 (1971)
141. Silver, J., Luker, P., Houlton, A., Howe, S., Hey, P., Ahmet, M.T.: J. Mater. Chem. **2**, 849 (1992)
142. Tanaka, K., Elkaim, E., Li, L., Jue, Z.N., Coppens, P., Landrum, J.: J. Chem. Phys. **84**, 6969–6978 (1986)
143. Boyd, P.D.W., Buckingham, D.A., McMeeking, R.F., Mitra, S.: Inorg. Chem. **18**, 3585–3591 (1979)
144. Mispelter, J., Momenteau, M., Lhoste, J.M.: J. Chem. Phys. **72**, 1003–1012 (1980)

145. McGarvey, B.R.: Inorg. Chem. **27**, 4691–4698 (1988)
146. Collman, J.P., Hoard, J.L., Kim, N., Lang, G., Reed, C.A.: J. Am. Chem. Soc. **97**, 2676–2681 (1975)
147. Dolphin, D., Sams, J.R., Tsin, T.B., Wong, K.L.: J. Am. Chem. Soc. **98**, 6970–6975 (1976)
148. Lang, G., Spartalian, K., Reed, C.A., Collman, J.P.: J. Chem. Phys. **69**, 5424–5427 (1978)
149. Strauss, S.H., Silver, M.E., Long, K.M., Thompson, R.G., Hudgens, R.A., Spartalian, K., Ibers, J.A.: J. Am. Chem. Soc. **107**, 4207–4215 (2002)
150. Walker, F.A.: Proton NMR and EPR spectroscopy of paramagnetic metalloporphyrins. In: Kadish, K.M., Smith, K.M., Guilard, R. (eds.) Porphyrin Handbook, pp. 81–183. Academic, San Diego (2000)
151. Reiff, W.M., Frommen, C.M., Yee, G.T., Sellers, S.P.: Inorg. Chem. **39**, 2076–2079 (2000)
152. Bachmann, J., Nocera, D.G.: J. Am. Chem. Soc. **127**, 4730–4743 (2005)
153. Sontum, S.F., Case, D.A., Karplus, M.: J. Chem. Phys. **79**, 2881–2892 (1983)
154. Choe, Y.-K., Nakajima, T., Hirao, K., Lindh, R.: J. Chem. Phys. **111**, 3837–3845 (1999)
155. Liao, M.-S., Scheiner, S.: J. Chem. Phys. **116**, 3635–3645 (2002)
156. Reiff, W.M., Wong, H., Baldwin, J.E., Huff, J.: Inorg. Chim. Acta **25**, 91–96 (1977)
157. Sellmann, D., Geck, M., Moll, M.: J. Am. Chem. Soc. **113**, 5259–5264 (2002)
158. Ray, K., Begum, A., Weyhermüller, T., Piligkos, S., Slagereren, J.V., Neese, F., Wieghardt, K.: J. Am. Chem. Soc. **127**, 4403–4415 (2005)
159. Bill, E., Bender, U., Gonser, U., Trautwein, A.X., Jones, W.M., Sabin, J.D.: In: Proc. Ind. Natl. Sci. Acad. Phys. Sci., Spec. Vol. for the International Conference on the Applications of the Mössbauer Effect, pp. 669–671, New Delhi (1982)
160. König, E., Madeja, K.: Inorg. Chem. **7**, 1848–1855 (1968)
161. König, E., Kanellakopulos, B.: Chem. Phys. Lett. **12**, 485–488 (1972)
162. König, E., Ritter, G., Kanellakopulos, B.: J. Chem. Phys. **58**, 3001–3009 (1973)
163. König, E., Schnakig, R.: Theor. Chim. Acta **30**, 205–208 (1973)
164. König, E., Ritter, G., Goodwin, H.A.: Inorg. Chem. **20**, 3677–3682 (1981)
165. König, E., Ritter, G., Kanellakopulos, B.: Inorg. Chim. Acta **59**, 285–291 (1982)
166. Feig, A.L., Lippard, S.J.: Chem. Rev. **94**, 759–805 (1994)
167. Que, L., Watanabe, Y.: Science **292**, 651–653 (2001)
168. Neese, F., Slep, L.D.: Angew. Chem. Int. Ed. **42**, 2942–2945 (2003)
169. Costas, M., Mehn, M.P., Jensen, M.P., Que, L.: Chem. Rev. **104**, 939–986 (2004)
170. Visser, S.P.: Angew. Chem. Int. Ed. **45**, 1790–1793 (2006)
171. Kovaleva, E.G., Lipscomb, J.D.: Nat. Chem. Biol. **4**, 186–193 (2008)
172. Xue, G., Fiedler, A.T., Martinho, M., Müncck, E., Que, L.: Proc. Natl. Acad. Sci. U. S. A. **105**, 20615–20620 (2008)
173. de Oliveira, F.T., Chanda, A., Banerjee, D., Shan, X., Mondal, S., Que Jr., L., Bominaar, E.L., Müncck, E., Collins, T.J.: Science **315**, 835–838 (2007)
174. Yoon, J., Wilson, S.A., Jang, Y.K., Seo, M.S., Nehru, K., Hedman, B., Hodgson, K.O., Bill, E., Solomon, E.I., Nam, W.: Angew. Chem. Int. Ed. **48**, 1257–1260 (2009)
175. Que, L.: J. Biol. Inorg. Chem. **9**, 684–690 (2004)
176. Meunier, B.: In: McClaverty, J., Meyer, T.J. (eds.) Comprehensive Coordination Chemistry II, pp. 261–280. Elsevier, New York (2003)
177. Meunier, B., de Visser, S.P., Shaik, S.: Chem. Rev. **104**, 3947–3980 (2004)
178. Shaik, S., Kumar, D., de Visser, S.P., Altun, A., Thiel, W.: Chem. Rev. **105**, 2279–2328 (2005)
179. Theorell, H.: Enzymologia **10**, 250 (1941)
180. Chance, B.: Arch. Biochem. Biophys. **41**, 404–415 (1952)
181. George, P.: Biochem. J. **54**, 267–276 (1953)
182. Moss, T., Ehrenberg, A., Bearden, A.J.: Biochemistry **8**, 4159–4162 (1969)

183. Hersleth, H.-P., Uchida, T., Rohr, A.K., Teschner, T., Schünemann, V., Kitagawa, T., Trautwein, A.X., Görbitz, C.H., Andersson, K.K.: *J. Biol. Chem.* **282**, 23372–23386 (2007)
184. Weller, M.T., Hector, A.L.: *Angew. Chem. Int. Ed.* **39**, 4162–4163 (2000)
185. Menil, F.: *J. Phys. Chem. Solids* **46**, 763–789 (1985)
186. Russo, U., Long, G.J.: Mössbauer spectroscopic studies of the high oxidation states of iron. In: Long, G.J., Grandjean, F. (eds.) *Mössbauer Spectroscopy Applied to Inorganic Chemistry*, pp. 289–329. Plenum, New York (1989)
187. Delattre, J.L., Stacy, A.M., Young, V.G., Long, G.J., Hermann, R., Grandjean, F.: *Inorg. Chem.* **41**, 2834–2838 (2002)
188. Takeda, Y., Naka, S., Takano, M., Shinjo, T., Takada, T., Shimada, M.: *Mater. Res. Bull.* **13**, 61–66 (1978)
189. Takano, M., Okita, T., Nakayama, N., Bando, Y., Takeda, Y., Yamamoto, O., Goodenough, J.B.: *J. Solid State Chem.* **73**, 140–150 (1988)
190. Takeda, Y., Shimada, M., Kanamaru, F., Koizumi, M., Yamamoto, N.: *Mater. Res. Bull.* **9**, 537–543 (1974)
191. Kawasaki, S., Takano, M., Takeda, Y.: *J. Solid State Chem.* **121**, 174–180 (1996)
192. Demazeau, G., Pouchard, M., Chevreau, N., Thomas, M., Ménil, F., Hagenmuller, P.: *Mater. Res. Bull.* **16**, 689–696 (1981)
193. Schulz, C.E., Devaney, P.W., Winkler, H., Debrunner, P.G., Doan, N., Chiang, R., Rutter, R., Hager, L.P.: *FEBS Lett.* **103**, 102–105 (1979)
194. Rutter, R., Hager, L.P., Dhonau, H., Hendrich, M., Valentine, M., Debrunner, P.: *Biochemistry* **23**, 6809–6816 (1984)
195. Boso, B., Lang, G., McMurry, T.J., Groves, J.T.: *J. Chem. Phys.* **79**, 1122–1126 (1983)
196. Bill, E., Ding, X.Q., Bominaar, E.L., Trautwein, A.X., Winkler, H., Mandon, D., Weiss, R., Gold, A., Jayraj, K., Hatfield, W.E., Kirk, M.L.: *Eur. J. Biochem.* **188**, 665–672 (1990)
197. Groves, J.T., Quinn, R., McMurry, T.J., Nakamura, M., Lang, G., Boso, B.: *J. Am. Chem. Soc.* **107**, 354–360 (1985)
198. Horner, O., Oddou, J.L., Mouesca, J.M., Jouve, H.M.: *J. Inorg. Biochem.* **100**, 477–479 (2006)
199. English, D.R., Hendrickson, D.N., Suslick, K.S.: *Inorg. Chem.* **22**, 368–370 (1983)
200. Grapperhaus, C.A., Mienert, B., Bill, E., Weyhermüller, T., Wieghardt, K.: *Inorg. Chem.* **39**, 5306–5317 (2000)
201. Rohde, J.-U., In, J.-H., Lim, M.H., Brennessel, W.W., Bukowski, M.R., Stubna, A., Münck, E., Nam, W., Que, L.: *Science* **299**, 1037–1039 (2003)
202. Lim, M.H., Rohde, J.U., Stubna, A., Bukowski, M.R., Costas, M., Ho, R.Y.N., Münck, E., Nam, W., Que, L.: *Proc. Natl. Acad. Sci. U. S. A.* **100**, 3665–3670 (2003)
203. Price, J.C., Barr, E.W., Tirupati, B., Bollinger, J.M., Krebs, C.: *Biochemistry* **42**, 7497–7508 (2003)
204. Pestovsky, O., Stoian, S., Bominaar, E.L., Shan, X.P., Münck, E., Que, L., Bakac, A.: *Angew. Chem. Int. Ed.* **44**, 6871–6874 (2005)
205. England, J., Martinho, M., Farquhar, E.R., Frisch, J.R., Bominaar, E.L., Münck, E., Que, L.: *Angew. Chem. Int. Ed.* **48**, 3622–3626 (2009)
206. Sturgeon, B.E., Burdi, D., Chen, S.X., Huynh, B.H., Edmondson, D.E., Stubbe, J., Hoffman, B.M.: *J. Am. Chem. Soc.* **118**, 7551–7557 (1996)
207. Lee, S.K., Fox, B.G., Froland, W.A., Lipscomb, J.D., Münck, E.: *J. Am. Chem. Soc.* **115**, 6450–6451 (2002)
208. Slep, L.D., Mijovilovich, A., Meyer-Klaucke, W., Weyhermüller, T., Bill, E., Bothe, E., Neese, F., Wieghardt, K.: *J. Am. Chem. Soc.* **125**, 15554–15570 (2003)
209. Jüstel, T., Weyhermüller, T., Wieghardt, K., Bill, E., Lengen, M., Trautwein, A.X., Hildebrandt, P.: *Angew. Chem. Int. Ed. Engl.* **34**, 669–672 (1995)
210. Jüstel, T., Müller, M., Weyhermüller, T., Kressl, C., Bill, E., Hildebrandt, P., Lengen, M., Grodzicki, M., Trautwein, A.X., Nuber, B., Wieghardt, K.: *Chem. Eur. J.* **5**, 793–810 (1999)

211. Hendrich, M.P., Gunderson, W., Behan, R.K., Green, M.T., Mehn, M.P., Betley, T.A., Lu, C.C., Peters, J.C.: Proc. Natl. Acad. Sci. U. S. A. **103**, 17107–17112 (2006)
212. Vogel, C., Heinemann, F.W., Sutter, J., Anthon, C., Meyer, K.: Angew. Chem. Int. Ed. **47**, 2681–2684 (2008)
213. Klinker, E.J., Jackson, T.A., Jensen, M.P., Stubna, A., Juhász, G., Bominaar, E.L., Münck, E., Que Jr., L.: Angew. Chem. Int. Ed. **45**, 7394–7397 (2006)
214. Bill, E., Schünemann, V., Trautwein, A.X., Weiss, R., Fischer, J., Tabard, A., Guillard, R.: Inorg. Chim. Acta **339**, 420–426 (2002)
215. Berry, J.F., Bill, E., Bothe, E., Neese, F., Wieghardt, K.: J. Am. Chem. Soc. **128**, 13515–13528 (2006)
216. Berry, J.F., Bill, E., Bothe, E., Weyhermüller, T., Wieghardt, K.: J. Am. Chem. Soc. **127**, 11550–11551 (2005)
217. Cummins, C.C., Schrock, R.R.: Inorg. Chem. **33**, 395–396 (1994)
218. Paulsen, H., Müther, M., Grodzicki, M., Trautwein, A.X., Bill, E.: Bull. Soc. Chim. Fr. **133**, 703–710 (1996)
219. Neese, F., Solomon, E.I.: Inorg. Chem. **37**, 6568–6582 (1998)
220. Gans, P., Buisson, G., Duee, E., Marchon, J.C., Erler, B.S., Scholz, W.F., Reed, C.A.: J. Am. Chem. Soc. **108**, 1223–1234 (1986)
221. Lang, G., Bosco, B., Erler, B.S., Reed, C.A.: J. Chem. Phys. **84**, 2998–3004 (1986)
222. Erler, B.S., Scholz, W.F., Lee, Y.J., Scheidt, W.R., Reed, C.A.: J. Am. Chem. Soc. **109**, 2644–2652 (1987)
223. Goff, H.M., Phillipi, M.A.: J. Am. Chem. Soc. **105**, 7567–7571 (1983)
224. Schünemann, V., Winkler, H.: Rep. Prog. Phys. **63**, 263–353 (2000)
225. Solomon, E.I., Brunold, T.C., Davis, M.I., Kemsley, J.N., Lee, S.K., Lehnert, N., Neese, F., Skulan, A.J., Yang, Y.S., Zhou, J.: Chem. Rev. **100**, 235–349 (2000)
226. Hausinger, R.P.: Crit. Rev. Biochem. Mol. Biol. **39**, 21–68 (2004)
227. Koehntop, K.D., Emerson, J.P., Que, L.: J. Biol. Inorg. Chem. **10**, 87–93 (2005)
228. Krebs, C., Price, J.C., Baldwin, J., Saleh, L., Green, M.T., Bollinger, J.M.: Inorg. Chem. **44**, 742–757 (2005)
229. Sinnecker, S., Svensen, N., Barr, E.W., Ye, S., Bollinger, J.M., Neese, F., Krebs, C.: J. Am. Chem. Soc. **129**, 6168–6179 (2007)
230. Hoffart, L.M., Barr, E.W., Guyer, R.B., Bollinger, J.M., Krebs, C.: Proc. Natl. Acad. Sci. U. S. A. **103**, 14738–14743 (2006)
231. Eser, B.E., Barr, E.W., Frantorn, P.A., Saleh, L., Bollinger, J.M., Krebs, C., Fitzpatrick, P.F.: J. Am. Chem. Soc. **129**, 11334 (2007)
232. Galonic, D.P., Barr, E.W., Walsh, C.T., Bollinger, J.M., Krebs, C.: Nat. Chem. Biol. **3**, 113–116 (2007)
233. Oh, N.Y., Suh, Y., Park, M.J., Seo, M.S., Kim, J., Nam, W.: Angew. Chem. Int. Ed. **44**, 4235–4239 (2005)
234. Nam, W.: Acc. Chem. Res. **40**, 522–531 (2007)
235. Sastri, C.V., Lee, J., Oh, K., Lee, Y.J., Jackson, T.A., Ray, K., Hirao, H., Shin, W., Halfen, J.A., Kim, J., Que, L., Shaik, S., Nam, W.: Proc. Natl. Acad. Sci. U. S. A. **104**, 19181–19186 (2007)
236. Kaizer, J., Klinker, E.J., Oh, N.Y., Rohde, J.U., Song, W.J., Stubna, A., Kim, J., Münck, E., Nam, W., Que, L.: J. Am. Chem. Soc. **126**, 472–473 (2004)
237. Martinho, M., Banse, F., Bartoli, J.F., Mattioli, T.A., Battioni, P., Horner, O., Bourcier, S., Girerd, J.J.: Inorg. Chem. **44**, 9592–9596 (2005)
238. Krebs, C., Fujimori, D.G., Walsh, C.T., Bollinger, J.M.: Acc. Chem. Res. **40**, 484–492 (2007)
239. Balland, V., Charlot, M.F., Banse, F., Girerd, J.J., Mattioli, T.A., Bill, E., Bartoli, J.F., Battioni, P., Mansuy, D.: Eur. J. Inorg. Chem., 301–308 (2004)
240. Que, L.: Acc. Chem. Res. **40**, 493–500 (2007)
241. Decker, A., Rohde, J.U., Klinker, E.J., Wong, S.D., Que, L., Solomon, E.I.: J. Am. Chem. Soc. **129**, 15983–15996 (2007)

242. Riggs-Gelasco, P.J., Shu, L.J., Chen, S.X., Burdi, D., Huynh, B.H., Que, L., Stubbe, J.: *J. Am. Chem. Soc.* **120**, 849–860 (1998)
243. Shu, L.J., Nesheim, J.C., Kauffmann, K., Münck, E., Lipscomb, J.D., Que, L.: *Science* **275**, 515–518 (1997)
244. Martinho, M., Xue, G.Q., Fiedler, A.T., Que, L., Bominaar, E.L., Münck, E.: *J. Am. Chem. Soc.* **131**, 5823–5830 (2009)
245. Wallar, B.J., Lipscomb, J.D.: *Chem. Rev.* **96**, 2625–2657 (1996)
246. Lammers, M., Follmann, H.: *Struct. Bond.* **54**, 27–91 (1983)
247. Summerville, D.A., Cohen, I.A.: *J. Am. Chem. Soc.* **98**, 1747 (1976)
248. Buchler, J.W., Dreher, C.: *Z. Naturforsch. B* **39**, 222–230 (1984)
249. Scheidt, W.R., Summerville, D.A., Cohen, A.: *J. Am. Chem. Soc.* **98**, 6623 (1976)
250. Ercolani, C., Hewage, S., Heucher, R., Rossi, G.: *Inorg. Chem.* **32**, 2975 (1993)
251. Ding, X.Q., Bill, E., Trautwein, A.X., Winkler, H., Kostikas, A., Papaefthymiou, V., Simopoulos, A., Beardwood, P., Gibson, J.F.: *J. Chem. Phys.* **99**, 6421–6428 (1993)
252. Gamelin, D.R., Bominaar, E.L., Kirk, M.L., Wieghardt, K., Solomon, E.I.: *J. Am. Chem. Soc.* **118**, 8085–8097 (1996)
253. Glaser, T., Beissel, T., Bill, E., Weyhermüller, T., Schünemann, V., Meyer-Klaucke, W., Trautwein, A.X., Wieghardt, K.: *J. Am. Chem. Soc.* **121**, 2193–2208 (1999)
254. Einsle, O., Tezcan, F.A., Andrade, S.L.A., Schmid, B., Yoshida, M., Howard, J.B., Rees, D.C.: *Science* **297**, 1696–1700 (2002)
255. Aliaga-Alcalde, M., George, S.D., Mienert, B., Bill, E., Wieghardt, K., Neese, F.: *Angew. Chem. Int. Ed.* **44**, 2908–2912 (2005)
256. Mehn, M.P., Peters, J.C.: *J. Inorg. Biochem.* **100**, 634–643 (2006)
257. Berry, J.F.: *Comm. Inorg. Chem.* **30**, 28–66 (2009)
258. Betley, T.A., Peters, J.C.: *J. Am. Chem. Soc.* **126**, 6252–6254 (2004)
259. Rohde, J.U., Betley, T.A., Jackson, T.A., Saouma, C.T., Peters, J.C., Que, L.: *Inorg. Chem.* **46**, 5720–5726 (2007)
260. Scepaniak, J.J., Fulton, M.D., Bontchev, R.P., Duesler, E.N., Kirk, M.L., Smith, J.M.: *J. Am. Chem. Soc.* **130**, 10515 (2008)
261. Jensen, M.P., Mehn, M.P., Que Jr., L.: *Angew. Chem. Int. Ed.* **42**, 4357 (2003)
262. Mahy, J.P., Battioni, P., Mansuy, D., Fisher, J., Weiss, R., Mispelter, J., Morgenstern-Badarau, I., Gans, P.: *J. Am. Chem. Soc.* **106**, 1699–1706 (1984)
263. Li, X.H., Fu, R., Lee, S.Y., Krebs, C., Davidson, V.L., Liu, A.M.: *Proc. Natl. Acad. Sci. U. S. A.* **105**, 8597–8600 (2008)
264. Collins, T.J., Kosta, K.L., Münck, E., Uffelmann, E.S.: *J. Am. Chem. Soc.* **112**, 5637 (1990)
265. Chanda, A., Popescu, D.-L., de Oliveira, F.T., Bominaar, E.L., Ryabov, A.D., Münck, E., Collins, T.J.: *J. Inorg. Biochem.* **100**, 606–619 (2006)
266. Berry, J.F., Bill, E., Garcia-Serres, R., Neese, F., Weyhermüller, T., Wieghardt, K.: *Inorg. Chem.* **45**, 2027–2037 (2006)
267. Song, Y.F., Berry, J.F., Bill, E., Bothe, E., Weyhermüller, T., Wieghardt, K.: *Inorg. Chem.* **46**, 2208–2219 (2007)
268. Cai, S., Licoccia, S., D’Ottavi, C., Paolesse, R., Nardis, S., Bulach, V., Zimmer, B., Shokhireva, T.K., Walker, F.A.: *Inorg. Chim. Acta* **339**, 171 (2002)
269. Ghosh, A., Steene, E.: *J. Inorg. Biochem.* **91**, 423 (2002)
270. Simkhovich, L., Goldberg, I., Gross, Z.: *Inorg. Chem.* **41**, 5433 (2002)
271. Ye, S., Tuttle, T., Bill, E., Simkhovich, L., Gross, Z., Thiel, W., Neese, F.: *Chem. Eur. J.* **14**, 10839–10851 (2008)
272. Muresan, N., Lu, C.C., Ghosh, M., Peters, J.C., Abe, M., Henling, L.M., Weyhermüller, T., Bill, E., Wieghardt, K.: *Inorg. Chem.* **47**, 4579–4590 (2008)
273. Roy, N., Sproules, S., Bill, E., Weyhermüller, T., Wieghardt, K.: *Inorg. Chem.* **47**, 10911–10920 (2008)
274. Khusniyarov, M.M., Weyhermüller, T., Bill, E., Wieghardt, K.: *J. Am. Chem. Soc.* **131**, 1208–1221 (2009)

275. Milsmann, C., Patra, G.K., Bill, E., Weyhermüller, T., George, S.D., Wieghardt, K.: Inorg. Chem. **48**, 7430–7445 (2009)
276. Levason, W., McAuliffe, C.A.: Coord. Chem. Rev. **12**, 151–184 (1974)
277. Demazeau, G., Buffat, B., Pouchard, M., Hagenmuller, P.: Z. Anorg. Allg. Chem. **491**, 60–66 (1982)
278. Newcomb, M., Zhang, R., Chandrasena, R.E.P., Halgrimson, J.A., Horner, J.H., Makris, T. M., Sligar, S.G.: J. Am. Chem. Soc. **128**, 4580–4581 (2006)
279. Wagner, W.-D., Nakamoto, K.: J. Am. Chem. Soc. **110**, 4044–4045 (1988)
280. Wagner, W.-D., Nakamoto, K.: J. Am. Chem. Soc. **111**, 1590–1589 (1989)
281. Dey, A., Ghosh, A.: J. Am. Chem. Soc. **124**, 3206–3207 (2002)
282. Meyer, K., Bill, E., Mienert, B., Weyhermüller, T., Wieghardt, K.: J. Am. Chem. Soc. **121**, 4859–4876 (1999)
283. Petrenko, T., George, S.D., Aliaga-Alcalde, N., Bill, E., Mienert, B., Xiao, Y., Guo, Y., Sturhahn, W., Cramer, S.P., Wieghardt, K., Neese, F.: J. Am. Chem. Soc. **129**, 11053–11060 (2007)
284. Berry, J.F., Bill, E., Bothe, E., George, S.D., Mienert, B., Neese, F., Wieghardt, K.: Science **312**, 1937–1941 (2006)
285. Herber, R.H., Johnson, D.: Inorg. Chem. **18**, 2786–2790 (1979)
286. Berry, J.F., George, S.D., Neese, F.: Phys. Chem. Chem. Phys. **10**, 4361–4374 (2008)
287. Shinjo, T., Ichida, T., Takada, T.: J. Phys. Soc. Jpn. **29**, 111–116 (1970)
288. Fluck, E.: 57-Fe: metal organic compounds. In: Goldanskii, V.I., Herber, R.H. (eds.) Chemical Applicaitons of Mössbauer Spectroscopy. Academic, New York (1968)
289. Kerler, W., Neuwirth, W.: Z. Physik. **167**, 176–193 (1962)
290. Reed, C.A.: Iron(I) and iron(IV) porphyrins. In: Kadish, K.M. (ed.) Electrochemical and Spectrochemical Studies of Biological Redox Components, pp. 333–356. American Chemical Society (1982)
291. Mashiko, T., Reed, C.A., Haller, K.J., Scheidt, W.R.: Inorg. Chem. **23**, 3192–3196 (1984)
292. Stoian, S.A., Yu, Y., Smith, J.M., Holland, P.L., Bominaar, E.L., Münck, E.: Inorg. Chem. **44**, 4915–4922 (2005)
293. Andres, H., Bominaar, E.L., Smith, J.M., Eckert, N.A., Holland, P.L., Münck, E.: J. Am. Chem. Soc. **124**, 3012–3025 (2002)
294. Stoian, S.A., Vela, J., Smith, J.M., Sadique, A.R., Holland, P.L., Münck, E., Bominaar, E.L.: J. Am. Chem. Soc. **128**, 10181–10192 (2006)
295. Chatt, J., Dilworth, J.R., Richards, R.L.: Chem. Rev. **78**, 589–625 (1978)
296. Yandulov, D.V., Schrock, R.R.: Science **301**, 76–78 (2003)
297. Burgess, B.K., Lowe, D.J.: Chem. Rev. **96**, 2983–3011 (1996)
298. Howard, J.B., Rees, D.C.: Chem. Rev. **96**, 2965–2982 (1996)
299. Seefeldt, L.C., Dean, D.R.: Acc. Chem. Res. **30**, 589–625 (1997)
300. Brown, S.D., Betley, T.A., Peters, J.C.: J. Am. Chem. Soc. **125**, 322–323 (2003)
301. Shima, S., Thauer, R.K.: Chem. Rec. **7**, 37–46 (2007)
302. Capon, J.F., Gloaguen, F., Petillon, F.Y., Schollhammer, P., Talarmin, J.: Coord. Chem. Rev. **253**, 1476–1494 (2009)
303. Ogata, H., Lubitz, W., Higuchi, Y.: Dalton Trans., 7577–7587 (2009)
304. Tard, C., Pickett, C.J.: Chem. Rev. **109**, 2245–2274 (2009)
305. Kemper, W., Kubowitz, F.: Biochem. Z. **265**, 245 (1933)
306. Warburg, O.: Schwermetalle als Wirkungsgruppen von Fermenten. Verlag Dr. Werner Sänger, Berlin (1946)
307. Peters, J.W., Lanzilotta, W.N., Lemon, B.J., Seefeldt, L.C.: Science **282**, 1853–1858 (1998)
308. Nicolet, Y., de Lacey, A.L., Vernede, X., Fernandez, V.M., Hatchikian, E.C., Fontecilla-Camps, J.C.: J. Am. Chem. Soc. **123**, 1596–1601 (2001)
309. Pierik, A.J., Hulstein, M., Hagen, W.R., Albracht, S.P.J.: Eur. J. Biochem. **258**, 572–578 (1998)
310. Popescu, C.V., Münck, E.: J. Am. Chem. Soc. **121**, 7877–7884 (1999)

311. Pereira, A.S., Tavares, P., Moura, I., Moura, J.J.G., Huynh, B.H.: *J. Am. Chem. Soc.* **123**, 2771–2782 (2001)
312. Bagley, K.A., Duin, E.C., Roseboom, W., Albracht, S.P.J., Woodruff, W.H.: *Biochemistry* **34**, 5527–5535 (1995)
313. Volbeda, A., Charon, M.-H., Piras, C., Hatchikian, E.C., Frey, M., Fontecilla-Camps, J.C.: *Nature* **373**, 580–587 (1995)
314. Surerus, K.K., Chen, M., Vanderzwaan, J.W., Rusnak, F.M., Kolk, M., Duin, E.C., Albracht, S.P.J., Münck, E.: *Biochemistry* **33**, 4980–4993 (1994)
315. Hsu, H.F., Koch, S.A., Popescu, C.V., Münck, E.: *J. Am. Chem. Soc.* **119**, 8371–8372 (1997)
316. Razavet, M., Davies, S.C., Hughes, D.L., Barclay, J.E., Evans, D.J., Fairhurst, S.A., Liu, X.M., Pickett, C.J.: *Dalton Trans.*, 586–595 (2003)
317. Chalbot, M.U., Mills, A.M., Spek, A.L., Long, G.J., Bouwman, E.: *Eur. J. Inorg. Chem.*, 453–457 (2003)
318. Shima, S., Lyon, E.J., Thauer, R.K., Mienert, B., Bill, E.: *J. Am. Chem. Soc.* **127**, 10430–10435 (2005)
319. Wang, X.F., Li, Z.M., Zeng, X.R., Luo, Q.Y., Evans, D.J., Pickett, C.J., Liu, X.M.: *Chem. Commun.*, 3555–3557 (2008)
320. Mauro, A.E., Casagrande, O.L., Nogueira, V.M., Santos, R.H.A., Gambardella, M.T.P., Lechat, J.R., Filho, M.F.J.: *Polyhedron* **12**, 2370 (1993)
321. Obrist, B.V., Chen, D., Ahrens, A., Schünemann, V., Scopelliti, R., Hu, X.: *Inorg. Chem.* **48**, 3514–3516 (2009)
322. Zirngibl, C., Hedderich, R., Thauer, R.K.: *FEBS Lett.* **261**, 112 (1990)
323. Shima, S., Pilak, O., Vogt, S., Schick, M., Stagni, M.S., Meyer-Klaucke, W., Warkentin, E., Thauer, R.K., Ermler, U.: *Science* **321**, 572–575 (2008)
324. Hiromoto, T., Warkentin, E., Moll, J., Ermler, U., Shima, S.: *Angew. Chem. Int. Ed.* **48**, 6457–6460 (2009)
325. Lyon, E.J., Shima, S., Boecker, R., Thauer, R.K., Grevels, F.W., Bill, E., Roseboom, W., Albracht, S.P.J.: *J. Am. Chem. Soc.* **126**, 14239–14248 (2004)

References to Sect. 8.3

326. Squyres, S.W., Arvidson, R.E., Baumgartner, E.T., Bell III, J.F., Christensen, P.R., Gorevan, S., Herkenhoff, K.E., Klingelhöfer, G., Madsen, M.B., Morris, R.V., Rieder, R., Romero, R.A.: *J. Geophys. Res.* **108**(E12), 8062 (2003)
327. Klingelhöfer, G., Morris, R.V., Bernhardt, B., Rodionov, D., de Souza Jr., P.A., Squyres, S.W., Foh, J., Kankeleit, E., Bonnes, U., Gellert, R., Schröder, C., Linkin, S., Evlanov, E., Zubkov, B., Prilutski, O.: *J. Geophys. Res.* **108**(E12), 8067 (2003)
328. Knudsen, J.M., Madsen, M.B., Olsen, M., Vistisen, L., Koch, C.B., Moerup, S., Kankeleit, E., Klingelhöfer, G., Evlanov, E.N., Khromov, V.N., Mukhin, L.M., Prilutskii, O.F., Zubkov, B., Smirnov, G.V., Juchniewicz, J.: *Hyperfine Interact.* **68**, 83 (1992)
329. Knudsen, J.M.: *Hyperfine Interact.* **47**, 3 (1989)
330. Schröder, C., Klingelhöfer, G., Morris, R.V., Rodionov, D.S., Fleischer, I., Blumers, M.: *Hyperfine Interact.* **182**, 149 (2008)
331. Morris, R.V., Klingelhöfer, G., Schröder, C., Fleischer, I., Ming, D.W., Yen, A.S., Gellert, R., Arvidson, R.E., Rodionov, D.S., Crumpler, L.S., Clark, B.C., Cohen, B.A., McCoy, T.J., Mittlefehldt, D.W., Shmidt, M.E., de Souza, P.A., Squyres, S.W.: *J. Geophys. Res.* **113**, E12S42 (2008)
332. Morris, R.V., Klingelhöfer, G., Schröder, C., Rodionov, D.S., Yen, A., de Souza Jr., P.A., Ming, D.W., Wdowiak, T., Gellert, R., Bernhardt, B., Evlanov, E.N., Zubkov, B., Foh, J.,

- Bonnes, U., Kankeleit, E., Gütlich, P., Renz, F., Squyres, S.W., Arvidson, R.E.: *J. Geophys. Res.* **111**, E02S13 (2006)
333. Klingelhöfer, G., Morris, R.V., Bernhardt, B., Schröder, C., Rodionov, D.S., de Souza Jr., P.A., Yen, A., Gellert, R., Evlanov, E.N., Zubkov, B., Foh, J., Bonnes, U., Kankeleit, E., Gütlich, P., Ming, D.W., Renz, F., Wdowiak, T., Squyres, S.W., Arvidson, R.E.: *Science* **306**, 1740 (2004)
334. Morris, R.V., Klingelhöfer, G., Schröder, C., Rodionov, D.S., Yen, A., Ming, D.W., De Souza Jr., P.A., Wdowiak, T., Fleischer, I., Gellert, R., Bernhardt, B., Bonnes, U., Cohen, B.A., Evlanov, E.N., Foh, J., Gütlich, P., Kankeleit, E., McCoy, T., Mittlefehldt, D.W., Renz, F., Schmidt, M.E., Zubkov, B., Squyres, S.W., Arvidson, R.E.: *J. Geophys. Res.* **111**, E12S15 (2006)
335. Squyres, S.W., Knoll, A.H., Arvidson, R.E., Ashley, J.W., Bell III, J.F., Calvin, W.M., Christensen, P.R., Clark, B.C., Cohen, B.A., De Souza Jr., P.A., Edgar, L., Farrand, W.H., Fleischer, I., Gellert, R., Golombek, M.P., Grant, J., Grotzinger, J., Hayes, A., Herkenhoff, K.E., Johnson, J.R., Jolliff, B., Klingelhöfer, G., Knudson, A., Li, R., McCoy, T.J., McLennan, S.M., Ming, D.W., Mittlefehldt, D.W., Morris, R.V., Rice Jr., J.W., Schröder, C., Sullivan, R.J., Yen, A., Yingst, R.A.: *Science* **324**, 1058 (2009)
336. Klingelhöfer, G.: *Hyperfine Interact.* **113**, 369 (1998)
337. Klingelhöfer, G.: In: Garcia, M., Marco, J.F., Plazaola, F. (eds.) *Industrial Applications of the Mössbauer Effect*, p. 369. American Institute of Physics, New York (2005)
338. Klingelhöfer, G., Fegley Jr., B., Morris, R.V., Kankeleit, E., Held, P., Evlanov, E., Priloutskii, O.: *Planet. Space Sci.* **44**, 1277–1288 (1996)
339. Klingelhöfer, G., Held, P., Teucher, R., Schlichting, F., Foh, J., Kankeleit, E.: *Hyperfine Interact.* **95**, 305 (1995)
340. Bell, J. (ed.): *The Martian Surface*. Cambridge University Press, Cambridge (2008)
341. Morris, R.V., Klingelhöfer, G.: In: Bell, J. (ed.) *The Martian Surface*, p. 339. Cambridge University Press, Cambridge (2008)
342. Kieffer, H.H., Jakosky, B.M., Snyder, C.W., Mathews, M.S. (eds.): *Mars*. University of Arizona Press, Tucson (2008)
343. Barlow, N. (ed.): *Mars: An Introduction to its Interior, Surface and Atmosphere*. Cambridge University Press, Cambridge (2008)
344. Gibson, E.K., Pillinger, C.T., Wright, I.P., Morgan, G.H., Yau, D., Stewart, J.L.C., Leese, M.R., Praine, I.J., Sheridan, S., Morse, A.D., Barber, S.J., Ebert, S., Goesmann, F., Roll, R., Rosenbauer, H., Sims, M.R.: *LPSC* **35**, 1845 (2004)
345. Pillinger, C.: *Space is a Funny Place*. Barnstorm Productions, Venice (2007)
346. Fleischer, I., Klingelhöfer, G., Schröder, C., Morris, R.V., Hahn, M., Rodionov, D., Gellert, R., de Souza, P.A.: *J. Geophys. Res.* **113**, E06S21 (2008)
347. Fleischer, I., Klingelhöfer, G., Schröder, S., Rodionov, D.: *Hyperfine Interact.* **186**, 193 (2008)
348. Klingelhöfer, G., Imkeller, U., Kankeleit, E., Stahl, B.: *Hyperfine Interact.* **71**, 1445 (1992)
349. Riesenmann, R., Steger, J., Kostiner, E.: *Nucl. Instrum. Method* **72**, 109 (1969)
350. Held, P.: *MIMOS II – Ein miniaturisiertes Mößbauerspektrometer in Rückstreu geometrie zur mineralogischen Analyse der Marsoberfläche*. Ph.D. thesis, Institute of Nuclear Physics, TU Darmstadt (1997)
351. Squyres, S.W., Arvidson, R.E., Bell III, J.F., Brückner, J., Cabrol, N.A., Calvin, W., Carr, M. H., Christensen, P.R., Clark, B.C., Crumpler, L., Des Marais, D.J., d'Uston, C., Economou, T., Farmer, J., Farrand, W., Folkner, W., Golombek, M., Gorevan, S., Grant, J.A., Greely, R., Grotzinger, J., Haskin, L., Herkenhoff, K.E., Hviid, S., Johnson, J., Klingelhöfer, G., Knoll, A.H., Landis, G., Lemmon, M., Li, R., Madsen, M.B., Malin, M.C., McLennan, S. M., McSween, H.Y., Ming, D.W., Moersch, J., Morris, R.V., Parker, T., Rice Jr., J.W., Richter, L., Rieder, R., Sims, M., Smith, P., Soderblom, L.A., Sullivan, R., Wänke, H., Wdowiak, T., Wolff, M., Yen, A.: *Science* **306**, 1698 (2004)
352. Squyres, S.W., Arvidson, R.E., Bell III, J.F., Brückner, J., Cabrol, N.A., Calvin, W., Carr, M. H., Christensen, P.R., Clark, B.C., Crumpler, L., Des Marais, D.J., d'Uston, C., Economou, T., Farmer, J., Farrand, W., Folkner, W., Golombek, M., Gorevan, S., Grant, J.A., Greely, R.,

- Grotzinger, J., Haskin, L., Herkenhoff, K.E., Hviid, S., Johnson, J., Klingelhöfer, G., Knoll, A.H., Landis, G., Lemmon, M., Li, R., Madsen, M.B., Malin, M.C., McLennan, S.M., McSween, H.Y., Ming, D.W., Moersch, J., Morris, R.V., Parker, T., Rice Jr., J.W., Richter, L., Rieder, R., Sims, M., Smith, M., Smith, P., Soderblom, L.A., Sullivan, R., Wänke, H., Wdowiak, T., Wolff, M., Yen, A.: *Science* **305**, 794 (2004)
353. Rieder, R., Gellert, R., Brückner, J., Clark, B.C., Dreibus, G., d'Uston, C., Economou, T., Klingelhöfer, G., Lugmeier, G.W., Wänke, H., Yen, A., Zipfel, J., Squyres, S.W., Athena Science Team: *Lunar Planet. Sci.* **35**, 2172 (2004)
354. Rieder, R., Gellert, R., Brückner, J., Klingelhöfer, G., Dreibus, G., Yen, A., Squyres, S.W.: *J. Geophys. Res.* **108**(E12), 8066 (2003)
355. McSween, H., Wyatt, M.B., Gellert, R., Bell III, J.F., Morris, R.V., Herkenhoff, K.E., Crumpler, L.S., Milam, K.A., Stockstill, K.R., Tornabene, L., Arvidson, R.E., Bartlett, P., Blaney, D., Cabrol, N.A., Christensen, P.R., Clark, B.C., Crisp, J.A., Des Marais, D.J., Economou, T., Farmer, J.D., Farrand, W., Ghosh, A., Golombek, M., Gorevan, S., Greeley, R., Hamilton, V.E., Johnson, J.R., Joliff, B.L., Klingelhöfer, G., Knudson, A.T., McLennan, S., Ming, D., Moersch, J.E., Rieder, R., Ruff, S.W., Schroeder, C., de Souza Jr., P.A., Squyres, S.W., Wänke, H., Wang, A., Yen, A., Zipfel, J.: *J. Geophys. Res.* **111**, E02S10 (2006)
356. Klingelhöfer, G., DeGrave, E., Morris, R.V., Van Alboom, A., De Resende, V.G., De Souza Jr., P.A., Rodionov, D., Schröder, C., Ming, D.W., Yen, A.: *Hyperfine Interact.* **166**, 549 (2005)
357. Van Cromphaut, C., de Resende, V.G., De Grave, E., Van Alboom, A., Vandenberghe, R.E., Klingelhöfer, G.: *Geochim. Cosmochim. Acta* **71**, 4814 (2007)
358. Klingelhöfer, G., Morris, R.V., de Souza Jr., P.A., Rodionov, D., Schröder, C.: *Hyperfine Interact.* **170**, 169 (2006)
359. Schröder, C., Rodionov, D.S., McCoy, T.J., Joliff, B.L., Gellert, R., Nittler, L.R., Farrand, W.H., Johnson, J.R., Ruff, S.W., Ashley, J.W., Mittlefehldt, D.W., Herkenhoff, K.E., Fleischer, I., Haldemann, A.F.S., Klingelhöfer, G., Ming, D.W., Morris, R.V., de Souza Jr., P.A., Squyres, S. W., Weitz, C., Yen, A.S., Zipfel, J., Economou, T.: *J. Geophys. Res.* **113**, E06S22 (2008)
360. Fleischer, I., Schröder, C., Klingelhöfer, G., Gellert, R.: *Meteorit. Planet. Sci. Suppl.*, 5238 (2009)
361. Schröder, C., Ashley, J.W., Chapman, M.G., Cohen, B.A., Farrand, W.H., Fleischer, I., Gellert, R., Herkenhoff, K.E., Johnson, J.R., Joliff, B.L., Joseph, J., Klingelhöfer, G., Morris, R.V., Squyres, S.W., Wright, S.P., Athena Science Team: *LPSC* **40**, 1665 (2009)
362. de Souza Jr., P.A., Klingelhöfer, G., Morimoto, T.: *Hyperfine Interact.* **C 5**, 487 (2002)
363. Feder, F., Trolard, F., Klingelhöfer, G., Bourrie, G.: *Geochim. Cosmochim. Acta* **69**, 4463 (2005)
364. Rodionov, D., Klingelhöfer, G., Bernhardt, B., Schröder, C., Blumers, M., Kane, S., Trolard, F., Bourrie, G., Genin, J.-M.: *Hyperfine Interact.* **167**, 869 (2006)
365. de Souza Jr., P.A., Bernhardt, B., Klingelhöfer, G., Gütlich, P.: *Hyperfine Interact.* **151/152**, 125–130 (2003)
366. Klingelhöfer, G.: In: Miglierini, M., Petridis, D. (eds.) *Mössbauer Spectroscopy in Materials Science*, p. 413. Kluwer Academic, Amsterdam (1999)
367. Klingelhöfer, G., da Costa, G.M., Prous, A., Bernhardt, B.: *Hyperfine Interact.* **C 5**, 423–426 (2002)
368. Prous, A., Malta, I.M.: *Santana do Riacho, Tomo I. Arquivos do Museu de História Natural* **12**, 384 (1991)
369. Prous, A.: *Santana do Riacho, Tomo I. Arquivos do Museu de História Natural* **13/14**, 417 (1992)
370. Strüder, L., Lechner, P., Leutenegger, P.: *Naturwissenschaften* **11**, 539–543 (1998)
371. Blumers, M., Bernhardt, B., Lechner, P., Klingelhöfer, G., d'Uston, C., Soltau, H., Strüder, L., Eckhardt, R., Brückner, J., Henkel, H., Girones Lopez, J., Maul, J.: *Nucl. Instr. Meth. A*, (2010), doi:10.1016/j.nima.2010.04.07